Research on Bulk-metallic Glasses and High-entropy Alloys in Peter K. Liaw's Group and with His Colleagues

CHANHO LEE, JAMIESON BRECHTL, and PETER K. LIAW

Bulk-metallic glasses (BMGs) and high-entropy alloys (HEAs) have attracted extensive attention in the field of metallic materials research for several decades due to their extraordinary properties. Many scientists and researchers have significantly contributed to developing new classes of metallic alloys, such as BMGs and HEAs, for various applications. Liaw's group and his colleagues have focused on the fundamental understanding of unique features, structures, and properties in BMGs and HEAs as well as the development of new types of metallic materials. In this article, we summarized the research work of Liaw's group and his colleagues by reviewing relevant papers. The goal is to provide an understanding of the current research progression in BMGs and HEAs while further encouraging young and junior researchers to be involved in the field of structural materials research pertaining to these classes of exotic alloy systems.

https://doi.org/10.1007/s11661-021-06197-6

I. INTRODUCTION

THE first metallic glass, which was composed of gold and silicon, was produced in 1960 by rapid quenching from its melt.[1] In 1974, the first bulk-metallic glass (BMG) with a required cooling rate (R_c) of 10^3 K/s was developed, and consisted of palladium, copper, and silicon.[2,3] More recently, BMGs with diameters greater than the micrometer-thickness range have been successfully fabricated.[4] For instance, Johnson *et al*. produced a $Zr_{41.2}Ti_{13.8}Cu_{12.5}Ni_{10}Be_{22.5}$ with a diameter of 14 mm and $R_c \leq 10$ K/s.[5] Inoue proposed three empirical rules for the high glass-forming ability (GFA) in metallic glasses.[6] The first rule states that a multicomponent system must have more than three elements. The second rule states that the three main constituent atoms must have a size difference of at least 12 pct. These first two rules comprise what is known as the ''confusion principle'',[7] where the number of atoms coupled with the size disparity results in poor atomic bonding. This poor bonding scheme hinders the formation of a crystal structure, thereby reducing the R_c required to produce an amorphous structure.[8] It should also be mentioned that according to Johnson *et al*., very small changes in alloy composition can have a large and systematic impact on the glass-forming ability of BMGs.[9] The confusion principle is therefore tied to the structural stability of a BMG and has also been linked to its crystallization resistance during irradiation.[10] Finally, the third rule required for high GFA in BMGs is the negative heats of mixing among the three main constituent elements.

BMGs exhibit desirable properties, such as exceptional corrosion resistance,[11–13] high strength and hardness,[14–18] irradiation resistance,[19] good fatigue resistance,[20–23] and excellent magnetic properties.[24,25] Figure 1 features a plot of the Young's moduli and the tensile strengths for different BMGs and conventional alloys.[26] It is apparent that the BMGs exhibit significantly lower Young's moduli and higher tensile strengths as compared to the super high-strength and stainless steels. This combination of high tensile strengths and relatively-lower Young's modulus, therefore, make them a very appealing material with many potential applications in industry.

CHANHO LEE is with the Department of Materials Science and Engineering, The University of Tennessee, Knoxville, TN 37996 and also with the Materials Science and Technology Division, Los Alamos National Laboratory, Los Alamos, NM 87545. JAMIESON BRECHTL is with the Energy and Transportation Sciences Division, Oak Ridge National Laboratory, Oak Ridge, TN 37831. PETER K. LIAW is with the Department of Materials Science and Engineering, The University of Tennessee. Contact e-mail: pliaw@utk.edu

Manuscript submitted August 31, 2020, accepted February 11, 2021.

Chanho Lee and Jamieson Brechtl have contributed equally.

Article published online March 22, 2021

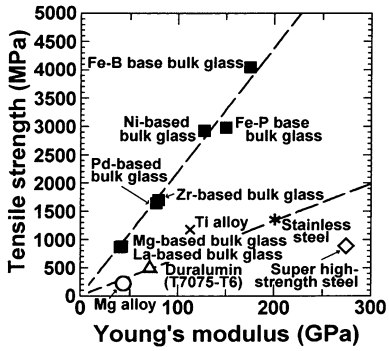

Fig. 1—Tensile strengths *vs* Young's moduli for different BMGs and conventional alloys (reproduced from Ref. [26] with permission).

In addition to the tensile strength and modulus, the fracture toughness of BMGs has also been investigated. For instance, investigations that examined the fracture toughness (K_c) of $Zr_{41.2}Ti_{13.8}Cu_{12.5}Ni_{10}Be_{22.5}$ (atomic percent, at. pct) (Vitreloy 1) reported that K_c ranged from ~ 17.9 to 68 MPa $m^{1/2}$, while another study recorded a measured value of ~ 17.9 MPa $m^{1/2}$.[27–29] In another study, a BMG alloy with the composition of $Zr_{52.5}Cu_{17.9}Ni_{14.6}Al_{10}Ti_5$ (Vitreloy 105) displayed toughness values of 28 to 69 MPa $m^{1/2}$.[30]

Liaw's group and his colleagues have been participating in the investigative work on BMGs and HEAs for almost 20 years. His first publication on the BMGs and HEAs occurred in 2002 and 2008, respectively, which discussed the corrosion effects in a Zr-based BMG,[13] and the alloy design strategy of solid-solution HEAs.[31] Besides his first publications on BMGs and HEAs with his colleagues, his work has also spanned a wide range of topics on BMG, including fatigue,[32–34] fracture,[35,36] irradiation effects,[37] thermal response,[38] and the serrated plastic flow.[39–41] In the meantime, his group also has focused on HEAs, including design of new HEAs,[31,42,43] lightweight HEAs,[44,45] phase stability,[45–47] microstructural investigations,[45,48,49] mechanical behaviors/mechanisms,[46,49–51] fatigue,[52,53] and corrosion resistance[54–56] of various HEAs, using experimental efforts coupled with theoretical calculations. According to the Web of Science database, Liaw's group and his colleagues have published 354 papers related to BMGs and 200 papers related to HEAs as of December 2020. Furthermore, he and his colleagues have also edited one BMG and one HEA books on the subjects, respectively.[4,57]

The research on a new class of multicomponent metallic materials, namely high-entropy alloys (HEAs), was pioneered by Profs. Cantor[58] and Yeh[59] in 1981 and 1995, respectively. They established the brand-new concept of multicomponent metallic alloys, suggesting that the high mixing entropies of their solid phases improve the phase stability according to the Gibbs-phase rule.[58] HEAs typically contain at least five principal elements, each with at. pct between 5 and 35 pct.[60] Furthermore, HEAs possess large configurational entropies [> 1.5R (R is the ideal gas constant)] in a random state, no matter whether they are of a single phase or multi-phase at room temperature (RT).[43] Although the vast majority of the reported HEAs contain more than one phase, the carefully-designed HEAs can possess a single-phase structure rather than ordered phases from regular solidification routes, such as body-centered-cubic (BCC), face-centered-cubic (FCC), and hexagonal-close-packed (HCP) structures.[42,58,61–65]

Historically speaking, HEAs have their roots in the work of Cantor and Yeh.[58,59] More specifically, Cantor *et al.*[58] was the first to produce the single-phase FeCoCrMnNi HEA and Yeh *et al.*[59] defined the HEA concept by his own experimental results and related theories. Importantly, their groundbreaking achievements have significantly inspired Liaw's group and his colleagues to study these advanced materials. Moreover, this inspiration has led to the active collaboration between Liaw and Prof. Yong Zhang on the fundamental HEA research that has resulted in published papers on the subject, including the first article in 2008, which gives the empirical information on the formation of BMGs and HEAs, as described below.[31]

According to several review papers and books, Diao and Liaw *et al.*[66] have classified the HEAs into four groups that are based on alloy compositions and mechanical properties, as shown Figure 2. The first group of HEAs consists of the 3*d*-transition-metal-containing HEAs (CoCrFeMnNi, CoCrFeNi, CoCrMnNi, CoFeMnNi, *etc.*),[58,67–70] which typically show soft mechanical characteristics. The second group contains alloys with combinations of transition metals with larger-atomic radius elements.[46,52,53,71–75] Moreover, most of the HEA compositions in this group include Al elements to decrease the density while maintaining high strength, as compared to alloys in Group 1. The third group pertains to refractory-type HEAs, which have been designed to have high strengths at elevated temperatures.[42,49,61,62,76–78] The fourth group, which include rare-earth elements, have also been studied to explore the various HEA compositions. Liaw's group and his colleagues have studied the different alloy compositions with a variety of crystalline structures, covering most of groups in Figure 2.

Among the designed HEAs that have been discussed above, Liaw's group and his colleagues have significantly focused on three different compositional HEAs, such as Al-containing HEAs (Al_xCoCrFeNi and $Al_{1.3}$CoCuCrFeNi),[46–48,50,52,53] lightweight HEAs (Al_xCrFeMnTi$_x$),[44,45] and refractory HEAs (NbTaTiV),[49] aiming to extend the range of applications. The detailed research processes for these three-types of HEAs in Liaw's group and his colleagues are schematically described in Figure 3. New HEA compositions have been designed by thermodynamic calculations, such as CALculation of PHAse Diagram (CALPHAD) modeling, through collaborations with Drs. Michael C. Gao and Chuan Zhang. CALPHAD describes the thermodynamic properties using phenomenological models.[44–46,49]

The specimens of newly-designed HEAs were fabricated by arc-melting the mixture of elemental metals with purity greater than 99.9 weight percent (wt pct) in a Ti-gettered high-purity argon environment. The mixture

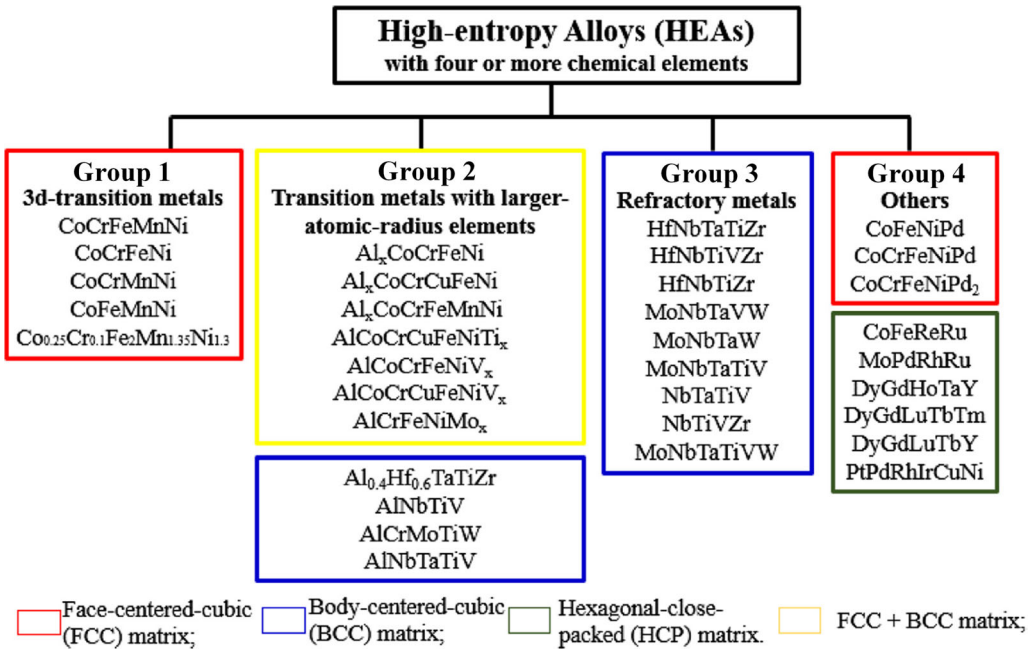

Fig. 2—The classifications of HEAs with four or more elements (reproduced from Ref. [66] with permission).

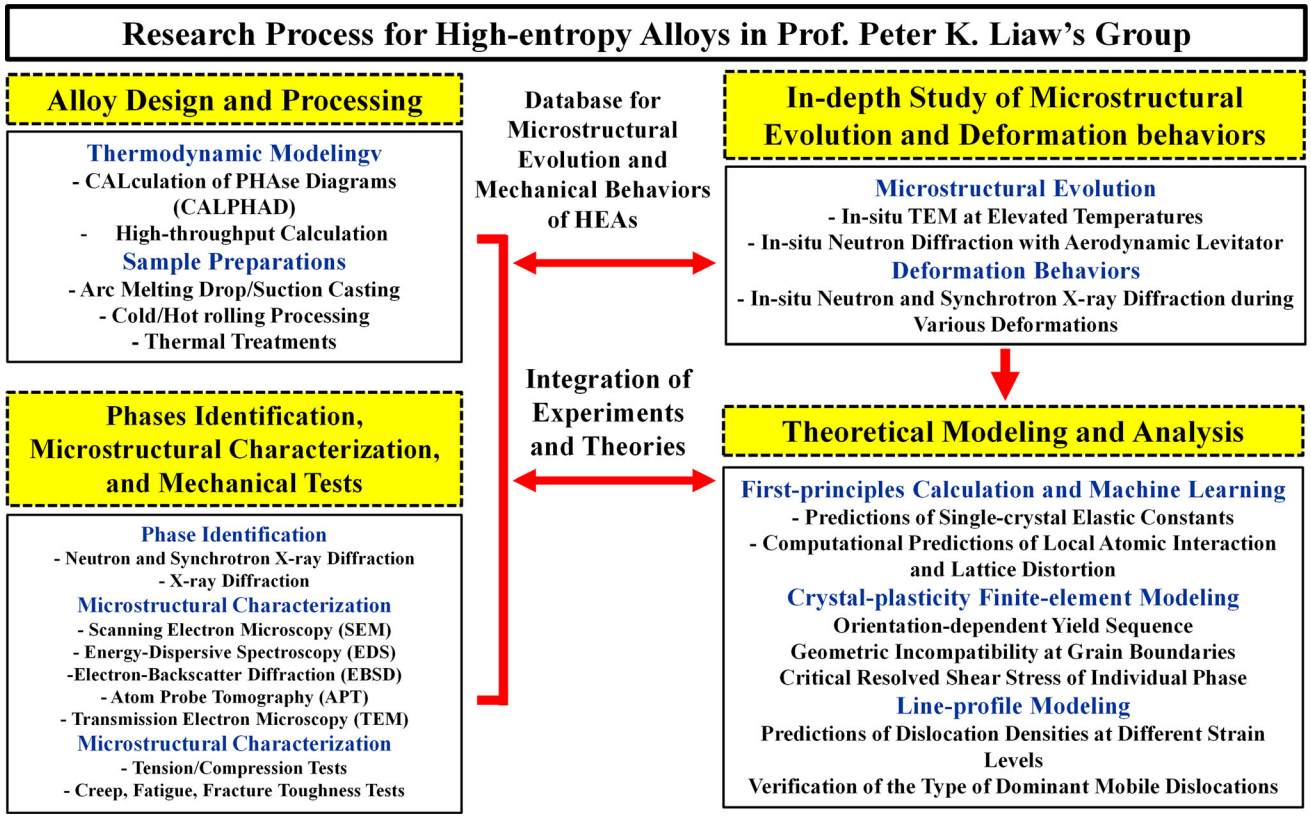

Fig. 3—The research process for HEAs in Liaw's group and his colleagues.

of melted elements was subsequently casted by a drop- and suction-casting technique to fabricate various sizes and shapes of samples for experiments. To control grain sizes and optimize mechanical properties, various treatment processes were applied to the prepared specimens. The suitable temperatures for the heat treatment were determined from the outcomes of the differential thermal analysis and CALPHAD modeling. Several other treatments, including the homogenization, water-quenching, cold-rolling, and hot-isostatic-pressing, were combined

and adjusted according to the experimental results to achieve the desired mechanical properties. The phase identification and microstructural characterization of the designed alloys were carried out, using various techniques, as illustrated in Figure 3. The mechanical behavior, such as tension, compression, creep, and fatigue were assessed *via* room and/or elevated temperature experiments to determine alloys, which exhibit the desired mechanical properties. With the results from the preliminary studies on the newly-designed HEAs, in-depth investigations on the microstructural evolution and deformation mechanisms for several selected HEAs were carried out, using state-of-the-art techniques, such as *in situ* transmission electron microscopy (TEM) and *in situ* neutron/synchrotron diffractions. The deformation mechanisms were further verified via theoretical calculations, such as first-principles calculations, machine learning (ML), ab initio molecular dynamics (AIMD) simulation, and crystal-plasticity finite-element simulation (CPFEM).

The first HEA paper in Liaw's group and his colleagues[31] outlined a potential design strategy for HEAs, *i.e.*, empirical solid-solution formation rules, considering the mixing enthalpy (ΔH_{mix}) and atomic-size difference $\left(\text{Delta} = \sqrt{\sum_{i=1}^{N} c_i(1 - r_i/\bar{r})^2}\right)$,[79] where N is the number of the components in the alloy system, c_i is the atomic percentage of the ith component, r_i is the atomic radius, and $\bar{r}$ is the average atomic radius, as presented in Figure 4(a). The suggested solid-solution formation rules were verified by experimental efforts, such as the phase identification and microstructural investigation for six of the alloy compositions, as shown in Figures 4(b) and (c). The $CrFeCoNiAlCu_{0.25}$, VCuFeCoNi, and $Al_{0.5}CrFeCoNi$ HEAs, which have a relatively small atomic-size difference and small absolute values of ΔH_{mix}, tend to possess a single FCC or BCC solid-solution phase, as shown in the X-ray diffraction (XRD) and scanning electron microscopy (SEM) images in Figure 4(b). On the other hand, the $Ti_2CrCuFeCoNi$, AlTiVYZr, and ZrTiVCuNiBe HEAs formed compounds (Figure 4(c)) with large values of Delta and ΔH_{mix}. The proposed HEA design strategy, therefore, significantly paved the way for designing the single solid-solution HEAs with desirable properties.

The present article summarizes the past and present research works of Liaw's group and his colleagues, which have extensively contributed to the fields of BMGs and HEAs research. In terms of BMGs, this paper will mainly focus on the experimental work pertaining to the shear band and shear-transformation-zone-mediated serrated plastic flow as well as fatigue behavior. Additionally, this current work will discuss how they modeled and analyzed the serrated flow using analytical techniques, such as the mean-field theory model and complexity methods. In terms of HEAs, factors, such as new design strategies, microstructural and mechanial properties of designed HEAs, and in-depth studies of the microstrutural evolution and deformation behaviors, using state-of-art facilities coupled with theoretical calculations, will be discussed. It is expected that the results produced from Liaw's group and his colleagues, as discussed in this work, will provide a clear discussion as to the research progress in BMGs and HEAs. It is also anticipated that this text will help encourage/guide junior researchers in their research plans regarding the future of BMGs and HEAs as structural materials.

Fig. 4—(*a*) Relationship between the mixing enthalpy (ΔH_{mix}) and atomic-size difference (Delta) for HEAs and typical multi-component bulk-metallic glasses. X-ray diffraction patterns and SEM images for (*b*) $CrFeCoNiAlCu_{0.25}$, VCuFeCoNi, $Al_{0.5}CrFeCoNi$ HEAs and (*c*) $Ti_2CrCuFeCoNi$, AlTiVYZr, and ZrTiVCuNiBe HEAs (reproduced from Ref. [31] with permission).

II. RESEARCH ON BULK-METALLIC GLASSES

A. *Microstructure of Bulk-Metallic Glasses*

1. *Free volume*

In terms of their structure, BMGs consists of an amorphous structure that contains regions of lower density that are composed of free volume.[4] The free volume in a metallic glass, as defined by Spaepen, is the part of an atoms nearest neighbor cage in which the atom can move around without a change in its energy.[80] Importantly, the free volume of a BMG is actually a part of the volume[81] that can be annihilated during the thermally induced structural relaxation.[82–84] On the other hand, free volume can be introduced during the glass transition.[83,85] To produce free volume, an atom with a volume, v, must have sufficient energy such that it can be squeezed into a smaller hole of size v^*. The required energy may be provided via an externally applied force, such as compression, which causes a localized shearing event. Spaepen defined the driving energy for the creation of free volume as[80]:

$$\Delta G = \tau\Omega - S\frac{(v^* - v)^2}{v} = \tau\Omega - \frac{2}{3}\mu\frac{1+\upsilon}{1-\upsilon}\frac{(v-v)^2}{v} \quad [1]$$

here τ is the atomic-level shear stress, Ω is the atomic volume, S is the elastic-distortion energy required to squeeze the atom into the smaller hole, μ is the shear modulus, and υ is Poisson's ratio. Figure 5 illustrates the hopping event and creation of free volume due to an applied shear stress on a group of atoms.[80,86]

The free volume, once it is created, can be annihilated due to the structural rearrangement caused by diffusing atoms.[80] Spaepen suggested that the number of diffusive jumps required for annihilation can range from 1 to 10. The atomic jumping process can be enhanced *via* an applied shear stress, which enables the annihilation of free volume.[87] The annihilation of free volume is important since it is generally accompanied by the structural relaxation of the BMG.[84]

2. *Shear transformation zones*

Shear transformation zones (STZs) are defined as the localized atomic deformation patches induced by shear and are thought to be the plasticity carriers in

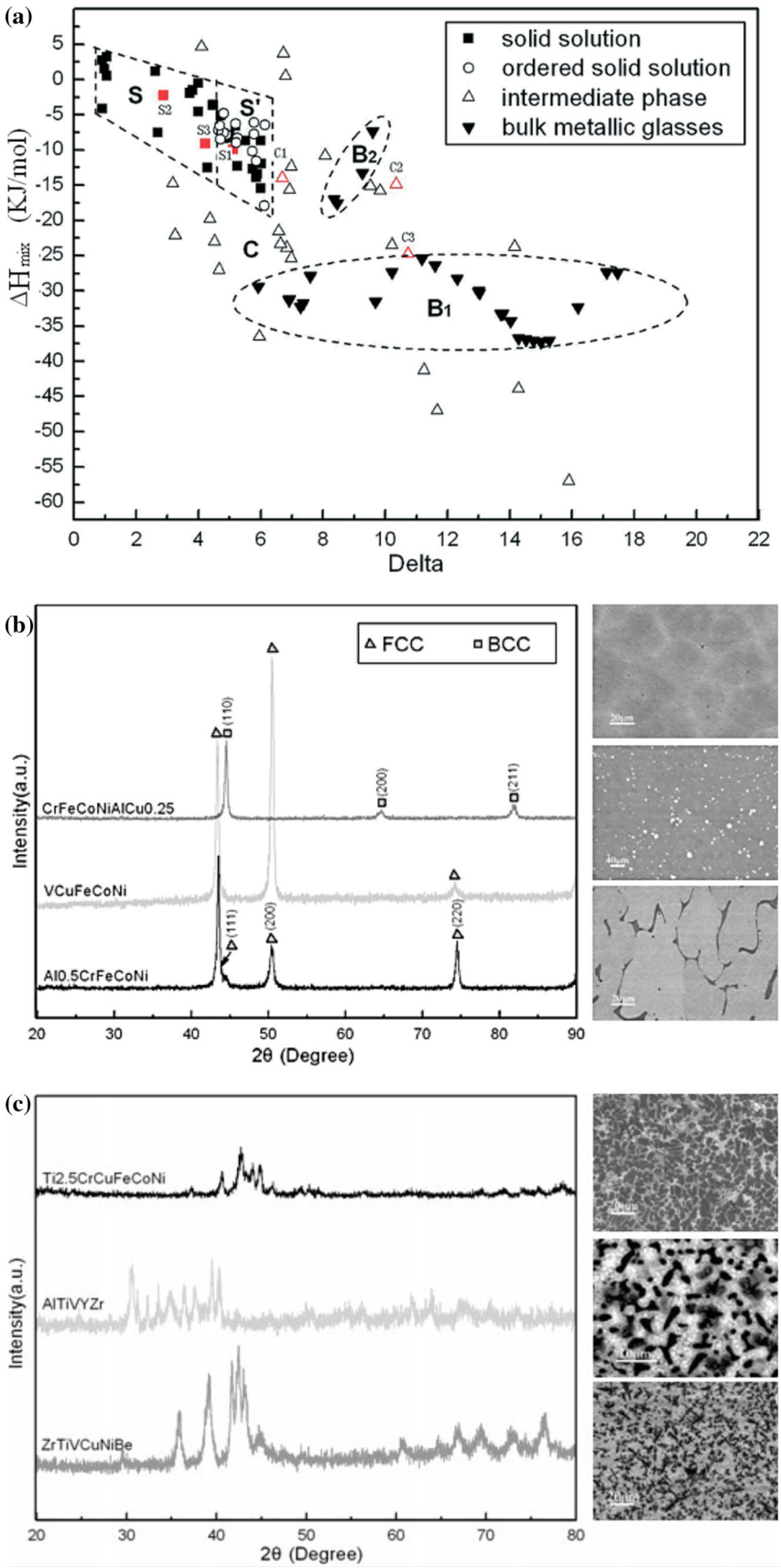
(a)
solid solution
ordered solid solution
intermediate phase
bulk metallic glasses
S
S'
S1
S2
S3
C1
C2
C3
B2
B1
C
ΔHmix (KJ/mol)
Delta
(b)
FCC
BCC
(110)
(200)
(211)
CrFeCoNiAlCu0.25
VCuFeCoNi
(111)
(200)
(220)
Al0.5CrFeCoNi
Intensity(a.u.)
2θ (Degree)
(c)
Ti2.5CrCuFeCoNi
AlTiVYZr
ZrTiVCuNiBe
Intensity(a.u.)
2θ (Degree)

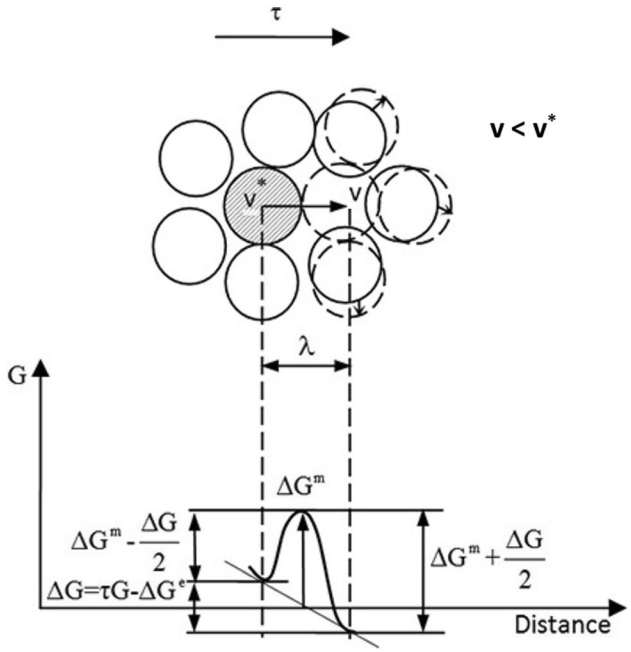

Fig. 5—Illustration of free volume creation by squeezing an atom of volume, v^*, into a neighboring hole of smaller volume, v (reproduced from Refs. [80], [86] with permission).

amorphous solids, such as BMGs.[88] Argon proposed a model to quantify this phenomenon, which describes the nonlinear nature of the STZ to the deformation in the solid.[89] Here, the shear-stress evolution during an STZ event is ascribed to the movement of two short rows of 4–6 atoms around a free volume site and is modeled according to a skewed sinusoid.[89,90] The STZ theory was extended to include a model that featured two-state dynamics of the STZs as well as an effective disorder temperature that could accurately account for the large-scale deformation in metallic glasses.[91] For the first state, system jamming occurs when all available STZs have been transformed during an applied stress which prevents plastic deformation in the direction of the stress. In contrast, the second state occurs at higher stresses, where the system becomes unjammed due to the rapid creation and annihilation of STZs.

More recently, Kosiba *et al.*[92] examined how manipulating the orientation of STZ activation could affect the overall plastic deformation of BMGs. Here, they generated a smoothly varying residual elastic stress field in a $Cu_{44}Zr_{44}Al_8Hf_2Co_2$ BMG using flash annealing. They found that when the energy stored along the path at 42 deg was insufficient, the propagation direction of the shear band would change. Such a modification in the direction of propagation, they surmised, would improve the malleability of the glass.

3. *Shear bands*

Although BMGs exhibit high strengths and elastic limits, they also display poor ductility during mechanical deformation. This lack of ductility is caused primarily by the formation of shear bands (SBs) that results in undesirable effects, such as cracking during post-yield plastic deformation.[4,93,94] SBs are often attributed to defects and structural inhomogeneity in the glassy matrix that result in stress concentrations.[95] The inhomogeneity may be a consequence of different factors, such as the local production of free volume or the restructuring of short-range order motifs. Once initiated, the shear band initiates and then propagates until the applied strain is fully accommodated by the shear accumulated within the band.[96] It should be noted that the lack of plasticity in BMGs is especially apparent during tension, where the severe localization of plastic deformation will occur, resulting in fracture without appreciable elongation.[97]

There are two types of SBs that, namely primary and secondary, which can be observed on the surface of BMGs that experience failure during mechanical testing. Liaw's team observed such SBs after compression tests (with a strain rate of 5×10^{-5} s^{-1}) on $Zr_{64.13}Cu_{15.75}Ni_{10.12}Al_{10}$ BMG (see Figures 6(a) and (b)).[98] The primary SBs typically propagate through the material at ~ 45 deg while the secondary bands are generally smaller and branch off the primary type.

The microstructure of SBs has been examined, using TEM.[99–104] Jiang *et al.* observed that nanocrystalline phases had formed in the shear bands during deformation *via* TEM imaging.[100,101] It was hypothesized that the nanocrystal formation was caused by the deformation-assisted atomic transport. Another TEM investigation revealed that shear bands in amorphous alloys have thicknesses, which can range from 10 to 100 nm.[95]

The heat content generated during the operation of SBs has been widely studied.[41,105–107] Previously, the heat content has been determined, using several methods, such as measuring the width of hot band using a fusible coating method[107] or examining the entire work performed by shear using an approximated coefficient.[106] To elucidate the thermal behavior of shear bands, Liaw's group and his colleagues examined the shear-banding behavior in a Vitreloy 105 BMG, using an infrared camera (IR).[108] For their experiments, BMG samples were tension tested at RT under a loading rate of 44.5 N/s. During the experiment, an IR camera was used to record the changes in the surface temperature, using a frame rate of 725 Hz, which amounted to 1.4×10^{-3} s between frames.

Figures 7(a) and (b) display a sample undergoing tension with the corresponding heat map, as detected by the IR camera. As can be observed in Figure 7(b), the temperature reached a maximum of ~ 296 K at the shear-band-initiation site. Furthermore, the temperature decreased along the shear-band, where it reached a local minimum of 294.4 K at its end. It was found that the mean width of these higher temperature bands was approximately 0.40 mm. From the results, the authors estimated that the temperature increase in the shear band could be as high as 650 K.

From the results, a free-volume-exhaustion mechanism was proposed to explain how propagating shear bands can stop in the absence of dislocations and grain boundaries.[108] According to the theory, the extra free volume is distributed in an elongated plastic zone ahead of the shear-band tip during shear-band propagation. During this process, the free volume "leaks out" of the

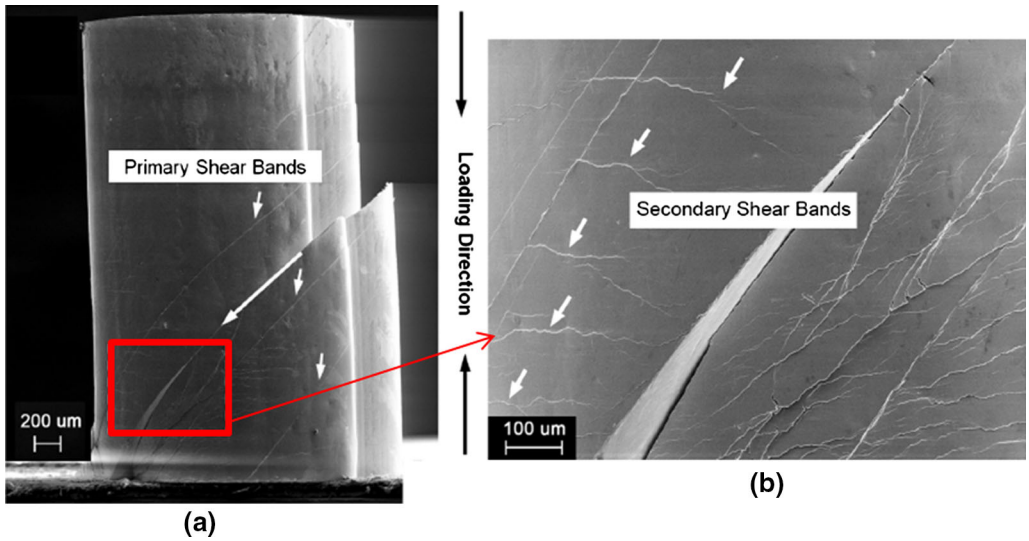

Fig. 6—(*a*) Fractured $Zr_{64.13}Cu_{15.75}Ni_{10.12}Al_{10}$ BMG sample after compression testing at a strain rate of 5×10^{-5} s^{-1} and (*b*) a magnified region, as indicated by a red rectangle in (*a*), which displays the interaction between multiple secondary SBs (Reprinted from Ref. [98] under the terms of the Creative Commons CC BY-NC-ND) (Color figure online).

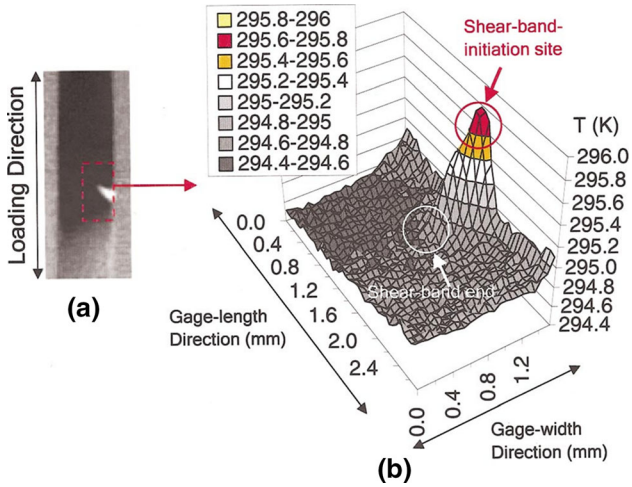

Fig. 7—Characterization of a shear band in a BMG specimen during tensile testing observed by thermography with an IR-camera frame rate of 725 Hz: (*a*) a thermographic image of a shear band during the experiment; (*b*) three-dimensional (3D) temperature profile of the shear band in the third image of (*a*) (reproduced from Ref. [108] with permission).

plastic zone around the shear-band tip, resulting in a decrease in the shear strain along the band. This decrease in the shear strain and free volume content is accompanied by a decrease in the temperature. Ultimately, the free volume and temperature in the mobile plastic zone will decrease until they go below a threshold value, and the shear band becomes immobilized.

Liaw's group and his colleagues also developed a model to estimate the probability of shear-band propagation given the shear-band-tip temperature.[108] For their model, they assumed that the free volume can only migrate either within or without the plastic zone of the shear band. The probability that the free volume migrates within the shear band is written as:

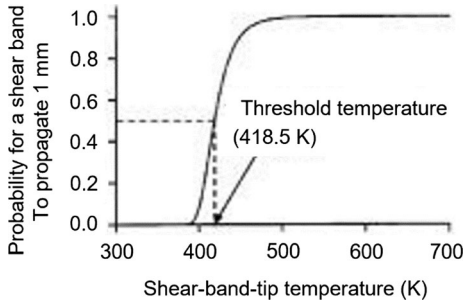

Fig. 8—The probability that a shear band will propagate 1 mm plotted as a function of the shear-band-tip temperature (reproduced from Ref. [108] with permission).

$$P = \left[1 - 0.008 \frac{e^{-\frac{\Delta G}{kT_0}}}{e^{-\frac{\Delta G}{kT_i}} + e^{-\frac{\Delta G}{kT_0}}}\right]^N \quad [2]$$

where ΔG is the activation energy for an atomic jump, k is Boltzmann's constant, T_0 is environmental temperature, and T_i is the temperature inside the plastic zone. For the present work, ΔG is set at 2 eV,[80] T_0 is the RT, and N is the number of atomic jumps. Using Eq. [2], the authors calculated the probability that a shear band would propagate 1 mm (see Figure 8) as a function of the shear-band-tip temperature. Initially, the probability has a sharp increase until it reaches a temperature of ~ 450 K, where there is a 90 pct chance that the shear band will propagate 1 mm. Furthermore, the probability reached about 50 pct at a temperature of 418.5 K.

B. *Plastic Deformation Behavior and Serrated Flow Phenomenon*

During dynamic strain aging, a BMG will exhibit the serrated flow, which is a type of plastic-deformation behavior. This phenomenon can be observed in the form

of fluctuations in the stress–strain or stress–time graph and can be comprised of a mix of decreasing and increasing stress values or rapid drops in the applied stress.[109] Serration behavior is important since it is typically linked to plastic instabilities that is accompanied by a loss in the ductility as well as the degradation of the surface quality of a material.[109,110] This type of deformation behavior has been found to occur not only in BMGs,[98,111–116] but also in Al-Mg alloys,[117–122] steels,[123–129] and high-entropy alloys (HEAs).[96,109,124,130–136] In contrast to crystalline alloys, where the serrated flow is typically due to the locking of dislocations by solute atoms,[123,130,137] the serrated plastic flow in BMGs occurs due to shear-banding dynamics.[98,112,124]

The serrated flow typically depends on the temperature or the applied strain rate, and has been categorized into five distinct types.[138] These types are known as A, B, C, D, and E (see Figure 9).[96,124] Furthermore, serrations can exhibit combinations of different serration types such as A + B and B + C. These different serrations exhibit characteristically different behavior. For instance, Type-A serrations are characterized by the periodic behavior and are generally associated with high strain rates, while Type-B serrations contain rapid fluctuations and have been associated with chaotic dynamics.[117] In contrast to Type-A and B serrations, Type-C serrations consist of relatively-larger stress-drop events, while Type-D serrations exhibit a stair-stepping pattern. Lastly, Type-E serrations display irregular fluctuations that occur with diminutive work-hardening during band propagation.[138]

In BMGs, the serrated flow occurs due to different mechanisms, such as shear-band formation and propagation as well as the agglomeration of liquid-like sites and flow-defect units.[4,139–142] As for shear bands, they are generally initiated by the local structural softening that is attributed to free-volume generation.[143] The activation and percolation of the flow units, on the other hand, are activated by factors, such as an applied stress or exposure to an elevated temperature.[144]

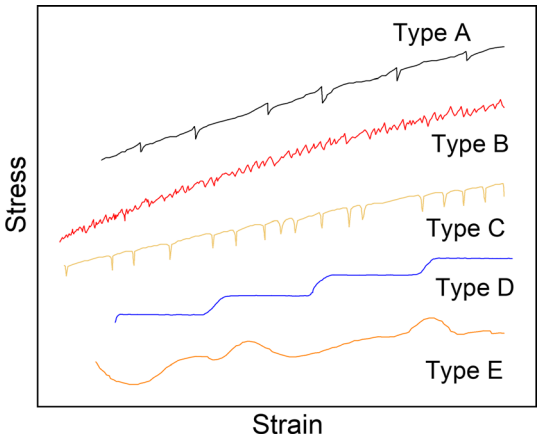

Fig. 9—The five types of serrations that may occur during plastic deformation (Reprinted from Ref. [96] under the terms of the Creative Commons CC BY 4.0).

Figure 10 features a basic schematic of the serration event that is attributed to the flow-defect accumulation that is followed by the shear-band initiation and propagation in a BMG.[96,139] During the first step of the process (step I in the graph), the applied stress results in the stress concentrations that are caused by differences in the moduli between the glassy matrix and the flow units, resulting in the activation of the flow units. During the next step, which is labelled II in the graph, the flow units expand and coalesce with neighboring regions. In step III, the applied stress reaches a local peak that is followed by the shear-band initiation in the amalgamated liquid-like region, yielding the propagation of the shear band and subsequent stress drop. During the stress drop, the stored elastic energy is dissipated until a sufficient amount is released, and the shear band is arrested. Upon arrest (step IV), the stress begins to increase, and the process repeats.

C. *Methods Used to Analyze Serrated Flows in BMGs*

1. *Mean-field theory*

The mean-field theory (MFT), which posits that the long-range behavior of the serration statistics is universal and does not depend on the small-scale structural details.[145,146] Furthermore, the model assumes that typical materials have weak spots and that a slowly-increasing shear stress or a slow shear rate triggers weak spots to slip.[98] This technique has been used to predict the distribution of avalanches sizes in a wide range of systems. These systems include bulk alloys, slowly-compressed nano-crystals, earthquakes, the magnetization of soft magnetic materials, and granular materials.[43,98,131,145,147–152] The associated mean-field model consists of a power-law distribution of stress-drop values that is multiplied by an exponential cutoff function. The model predicts that the distribution of stress-drop magnitudes obeys the following relationship[98]:

$$D(S,\Omega) \sim S^{-\kappa} D'\left(S\Omega^{-\lambda}\right) \qquad [3]$$

where $D(S, \Omega)$ is the distribution of stress-drop magnitudes based on some testing parameter, Ω, $D(S\Omega^{-\lambda})$ is an exponentially decaying function, κ and λ are universal exponents. It should be mentioned that the testing parameter could, for example, be the strain rate or the test temperature. According to the MFT, these exponents are $\kappa = 1.5$ and $\lambda = 2$,[153] which is related to the maximum observed stress drop, S_{max}, as $S_{max} \sim \Omega^{\lambda}$.

Another important statistic is known as the complementary cumulative distribution function (CCDF), C (S, Ω), which is also known as the survival function. This quantity defines the probability that a stress-drop magnitude greater than S will occur and is typically written as[98]:

$$C(S,\Omega) = \int_{S}^{\infty} D(S',\Omega)\mathrm{d}S' \sim \Omega^{-\lambda(\kappa-1)} C'\left(S\Omega^{-\lambda}\right) \qquad [4]$$

where, $C'\left(S\Omega^{-\lambda}\right)$ is a universal scaling function such that $\lambda(\kappa - 1) = 1$, based on the MFT in the steady-state

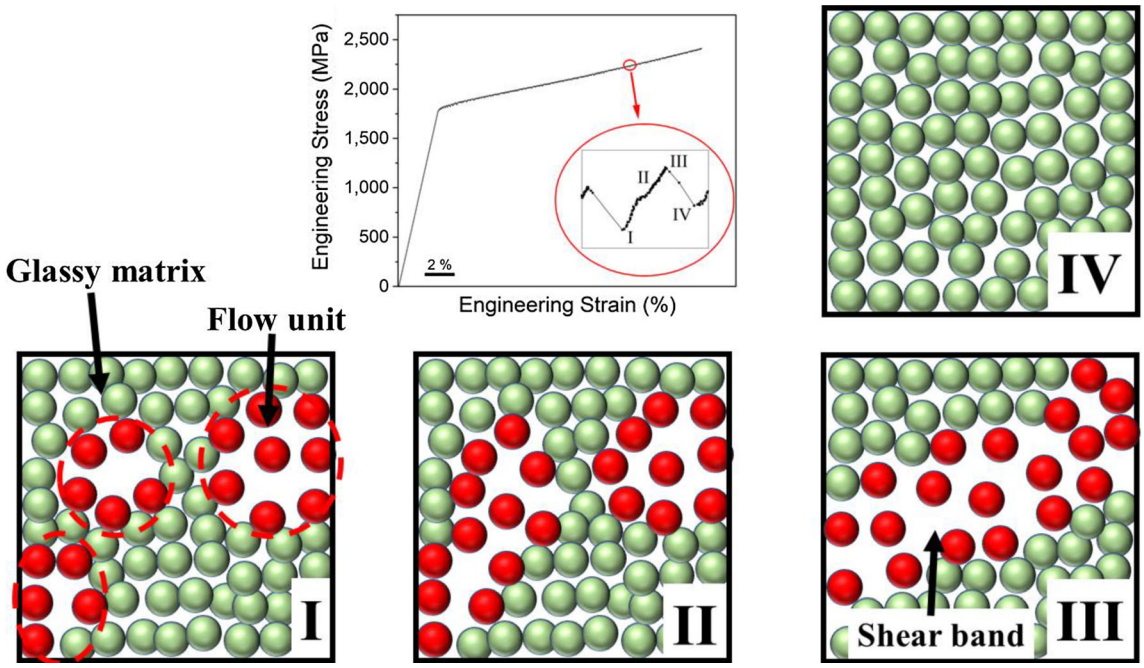

Fig. 10—The basic serration process that results from the flow defect accumulation during compressive deformation in a BMG where the numbered sections represent the different stages during the serration event as: I. activation of flow units in the liquid-like regions during compression, II: growth and amalgamation of the liquid-like cites with neighboring cites as the stress increases, III: initiation of a shear band when a critical stress is reached, IV: a stress-drop that is followed by the shear-band arrest and restoration of the local structure in the shear plane (Reprinted from Ref. [96] under the terms of the Creative Commons CC BY 4.0).

condition.[148] Once the CCDF is determined for each strain rate, the critical exponents are tuned until the curves are superimposed (scale collapse).[98,146,150,151] Importantly, the exponents determined from this scale collapse allow one to predict the stress-drop statistics for any strain rate, making the MFT model a very powerful predictive tool.

2. *Complexity analysis*

Many different phenomena, such as biological signals,[154–157] financial-time series,[158,159] chaos,[160] and serrated-flow behavior in BMGs and other alloy systems,[39,40,109,123,161,162] have been analyzed, using entropy-based calculations. For these calculations, the sample entropy quantifies the degree of complexity of the system.[154,155,163,164] The complexity of a dynamical system is typically correlated with the amount of irregularity inherent in the system.[157] It is important to note that the complexity of the time-series should not be equated with the variation in the signal.[165]

As for the serration behavior in conventional alloys, it has been reported that higher sample entropy values correspond to the amount (or variety) of interactions that transpire during plastic deformation, such as the solute atom–dislocation interactions.[109,129,162] In BMGs, on the other hand, serration behavior that is relatively more complex has been attributed to a greater amount of free-volume defects and shear-band interactions.[39,40] Furthermore, it has been hypothesized that higher sample entropy values indicate that a BMG can better adapt to an applied load.[39]

An example of an algorithm that has been used to calculate the complexity of dynamical behavior is the refined composite entropy multiscale entropy (RCMSE) method,[164] which has been implemented to study a host of phenomena, including the cognitive function,[166] noise,[160] and serrated flows in BMGs.[39,40] The discussion below will give a basic step-by-step procedure on how to evaluate the serration time data, using this algorithm.

As an initial step, the underlying strain-aging trend that occurs during plastic deformation is omitted from the stress *vs* time data. This step is completed by applying a moving average or polynomial fitting to the data and deleting the underlying trend from the original time series.[123,167] After the trend is eliminated, one evaluates the coarse-grained time series, $y^{\tau}_{k,j}$, via the following equation[164]:

$$y^{\tau}_{k,j} = \frac{1}{\tau} \sum_{i=(j-1)\tau+k}^{j\tau+k-1} x_i; \quad 1 \le j \le \frac{N}{\tau} \quad 1 \le k \le \tau \qquad [5]$$

here x_i is the ith data point in the given stress–time series, k defines at which point in the given data to initiate the algorithm, τ is the scale factor (typically ranges from 1 to 20), and N is the total number of points from the original time series. Next construct the template vectors of dimensions with sizes of m and $m + 1$:

$$y^{\tau,m}_{k,i} = \left\{ y^{\tau}_{k,i} y^{\tau}_{k,i+1} \cdots y^{\tau}_{k,i+m-1} \right\}; \quad 1 \le i \le N - m; \quad 1 \le k \le \tau \qquad [6]$$

In general, m is set to 2 to decrease the standard error in the sample-entropy results.[155] Next, determine whether the template vectors match (for m, $m + 1$) via the following equation [160]:

$$d_{ab}^{\tau,m} = y_a^{\tau,m} - y_{b\infty}^{\tau,m} = \max\left\{\left|y_{1,a}^{\tau} - y_{1,b}^{\tau}\right| \cdots \left|y_{i+m-1,a}^{\tau} - y_{i+m-1,b}^{\tau}\right|\right\} < r \quad [7]$$

here a r value of 0.15σ (σ is the standard deviation of the data) is chosen to make sure that the sample entropy values are independent of the variance of the stress-time data.[109] Once the number of matching pairs are determined, one totals them up for m, $m + 1$. One then solves for the RCMSE values, as a function of τ, for the stress–time series by[164]:

$$\mathrm{RCMSE}(\boldsymbol{y}, \tau, m, r) = \mathrm{Ln}\left(\frac{\sum_{k=1}^{\tau} n_{k,\tau}^{m}}{\sum_{k=1}^{\tau} n_{k,\tau}^{m+1}}\right) \quad [8]$$

where $n_{k,\tau}^{m}$ and $n_{k,\tau}^{m+1}$ are the total numbers of matching vectors, as determined from Eq. [7].

D. *Experimental Studies*

1. *Serrated flow behaviors*

Liaw's group and his colleagues examined and modeled the serration behavior of $Zr_{64.13}Cu_{15.75}Ni_{10.12}Al_{10}$ pillars that were compressed at constant strain rates ranging from 5×10^{-5} to 1×10^{-3} s^{-1}.[98,168] For the tests, the samples were cylindrical with a length of 4 mm and diameter of 2 mm (aspect ratio of 2). The results of the experiment can be observed in Figure 11, which features the engineering stress *vs* time data. The results indicate that the time until rupture increased with a decrease in the strain rate, where it was a maximum for the strain rate of 5×10^{-5} s^{-1}. For strain rates of 2×10^{-4} and 1×10^{-3} s^{-1}, the samples failed before they could reach the steady-state condition. The insets of the figure show a magnification of the serration curves, which display the sudden, pronounced decrease in the stress that is characteristic of the serrated flow.

Figure 12 shows the results of the MFT modeling and analysis of the data from Figure 11, where the CCDF was plotted as a function of the stress-drop, S. The CCDF curves display a parabolic shape in which the maximum stress drop increased with a decrease in the strain rate. This result agrees with the MFT model, which states that larger stress drops occur more frequently in samples that are strained at a slower rate.[169] The inset displays the collapsed curves with the corresponding universal exponents, κ and λ, which were determined to be 1.42 ± 0.20 and 0.22 ± 0.02, respectively. The value for λ, which is significantly lower than the expected value of 2 according to the MFT, was thought to be due to the samples breakage before they could reach the steady-state condition at the higher strain rates.

Fig. 13—The detrended stress-time data for the $Zr_{55}Cu_{30}Ni_5Al_{10}$ BMG subjected to compression in the (*a*) constrained conditions with strain rates of 2×10^{-5} to 2×10^{-3} s^{-1}, and the (*b*) unconstrained conditions with strain rates of 5×10^{-5} to 2×10^{-3} s^{-1} (reproduced from Ref. [39] with permission). ▶

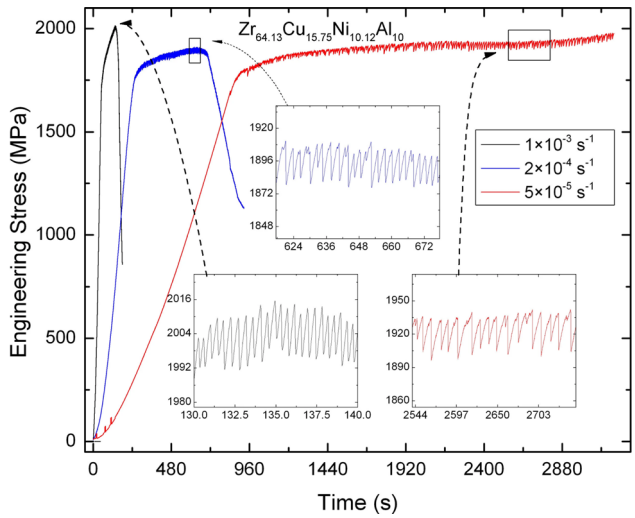

Fig. 11—Compression stress-time profiles for the $Zr_{64.13}Cu_{15.75}Ni_{10.12}Al_{10}$ BMG cylindrical samples compressed at strain rates of 1×10^{-3}, 2×10^{-4}, and 5×10^{-5} s^{-1} (RT) (Reprinted from Ref. [98] under the terms of the Creative Commons CC BY-NC-ND).

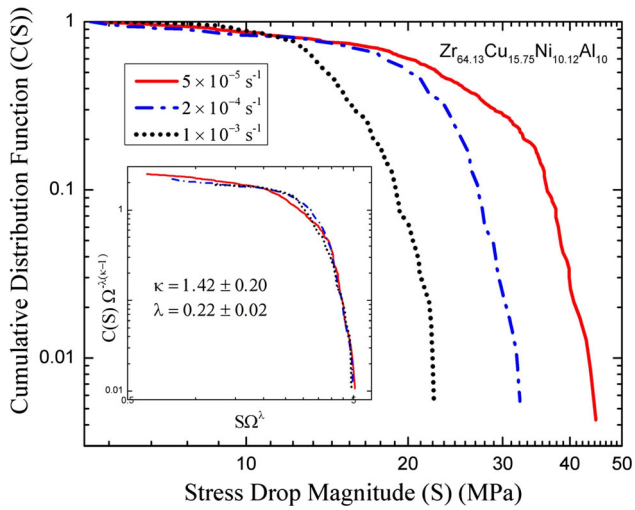

Fig. 12—The CCDF curves for the $Zr_{64.13}Cu_{15.75}Ni_{10.12}Al_{10}$ BMG cylindrical samples compressed at strain rates of 1×10^{-3}, 2×10^{-4}, and 5×10^{-5} s^{-1} (*RT*). The inset features the curves that were scale collapsed with MFT exponents of $\kappa = 1.42 \pm 0.20$ and $\lambda = 0.22 \pm 0.02$ (Reprinted from Ref. [98] under the terms of the Creative Commons CC BY-NC-ND).

In another study, Liaw's group and his colleagues examined the serration behavior of Vitreloy 105 that was subjected to uniaxial compression in the constrained and unconstrained conditions.[39] Samples were tested at RT and strain rates of 2×10^{-5} to 2×10^{-3} s^{-1}. The resulting detrended stress–time data for the constrained

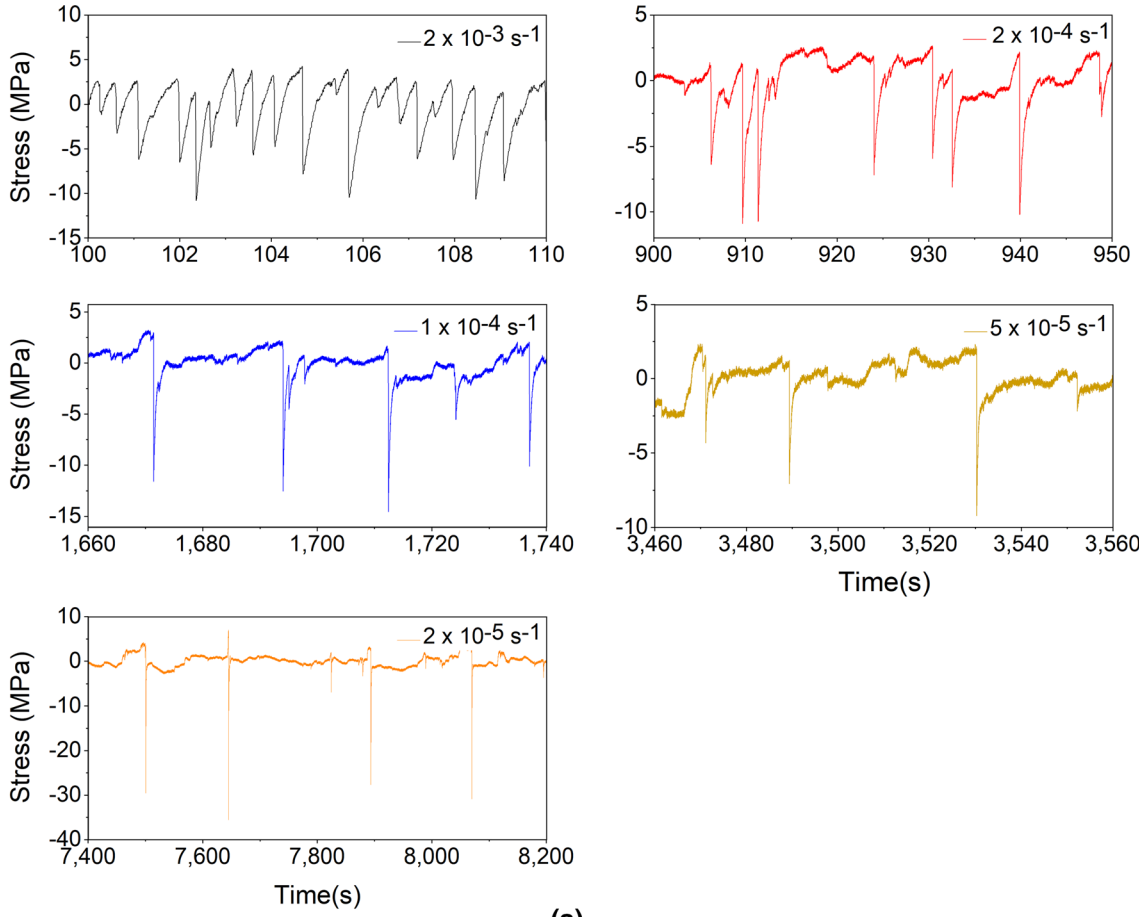
2 x 10-3 s-1
2 x 10-4 s-1
1 x 10-4 s-1
5 x 10-5 s-1
2 x 10-5 s-1
Stress (MPa)
Time(s)

(a)

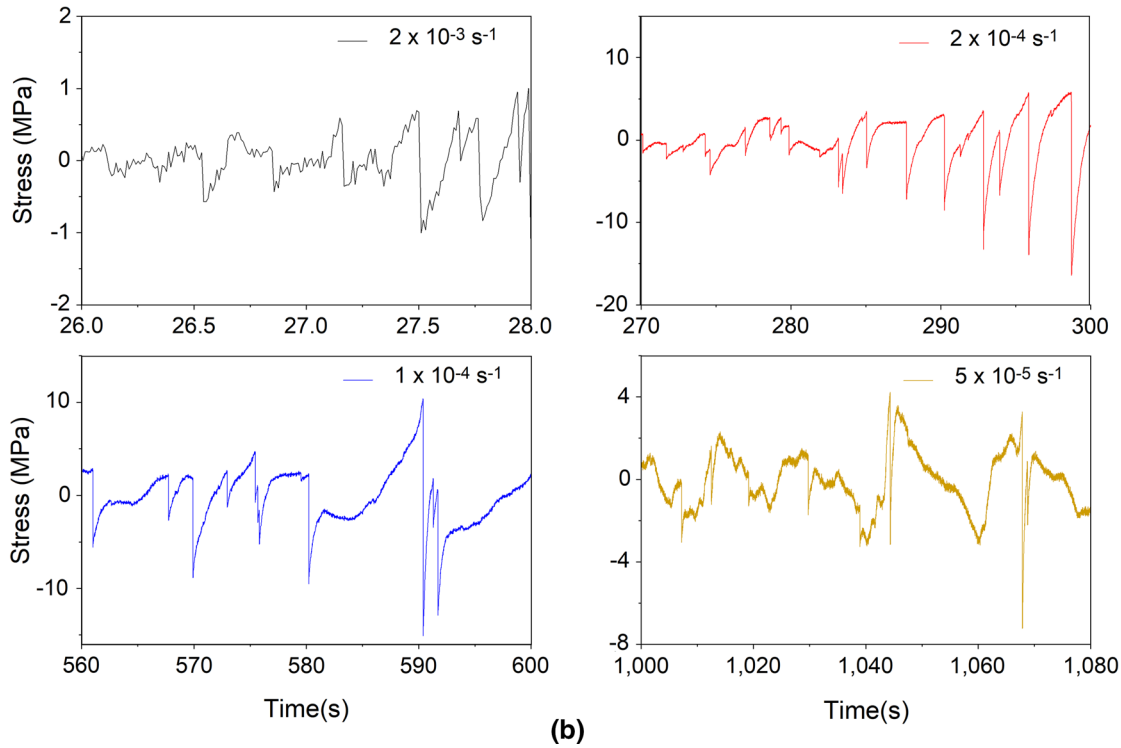
2 x 10-3 s-1
2 x 10-4 s-1
1 x 10-4 s-1
5 x 10-5 s-1
Stress (MPa)
Time(s)

(b)

and unconstrained conditions is presented in Figures 13(a) and (b), respectively. For Figure 13(a), it is apparent that the time between successive serrations decreases with an increase in the applied strain rate. It can also be observed that the irregularity of the stress fluctuations increases with respect to the strain rate. As compared to the other strain-rate conditions (for the constrained geometry), the stress drops are significantly larger for the sample tested at 2×10^{-5} s^{-1}. As for Figure 13(b), which displays the results for the samples tested in the unconstrained condition, there was a similar decrease in the time between stress-drops, as was observed in Figure 13(a). Furthermore, the irregularity of the serrated flow also increases with an increase in the strain rate. Moreover, the irregularity of the serrated flow also increases with an increase in the strain rate. Finally, it was also determined that the time before failure increased with an increase in the strain rate.

Figure 14(a) features the sample-entropy values for the specimens tested in the constrained condition for strain rates of 2×10^{-5} to 2×10^{-3} s^{-1}. It is apparent that the sample entropy curves exhibited an overall increase with the scale factor, which suggests that the serrated flow exhibited complex behavior across multiple scales. Moreover, the sample-entropy curves

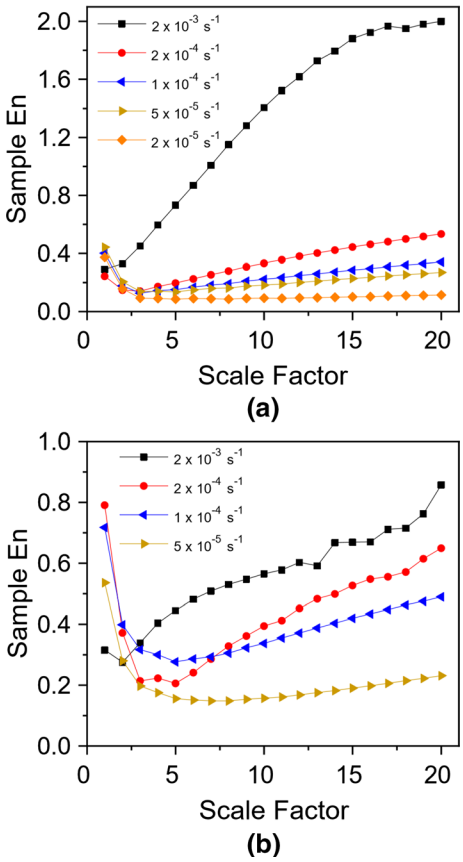

Fig. 14—Sample-entropy results for the $Zr_{55}Cu_{30}Ni_5Al_{10}$ BMG subjected to compression in the (*a*) constrained conditions for strain rates of 2×10^{-5} to 2×10^{-3} s^{-1} and the (*b*) unconstrained condition for strain rates of 5×10^{-5} to 2×10^{-3} s^{-1} reproduced from Ref. [39] with permission).

displayed an increasing trend as the strain rate increased, indicating that an increase in the strain rate led to an increase in the complexity of the serrated flow. This increase in the sample-entropy curve was most pronounced for the strain rate of 2×10^{-3} s^{-1}. Similar to Figure 14(a), the sample-entropy curves from Figure 14(b) also generally increased with the strain rate. It should also be mentioned that for the strain rate of 2×10^{-3}, the sample entropy was markedly greater (by a factor of ~ 2) for the sample compressed in the constrained condition. This result suggests that at the highest strain rate, the sample compressed in the constrained condition exhibited more complex dynamical behavior during the serrated flow.

From the results, it was surmised that the increasing complexity of the serration behavior with strain rate was a result of the increase in the defect creation.[39] This increase in the free volume content with the strain rate has also been reported in Reference 170. In this scenario, the created free-volume results in a greater number of free volume and anti-free volume defects[171,172] that can interact with propagating microcracks during the serrated plastic deformation. Here, such an increase in the number and variety of interactions is an indication of more complex dynamics. On a final note, it was suggested that the higher sample-entropy values and longer sample lifetimes indicate that the complexity of the serrated flow may correspond to the capacity of a BMG to accommodate an applied load.

In a similar investigation, Liaw's group and his colleagues studied the effect of annealing and strain rate on the complexity of the serrated flow in Vitreloy 105 during compression.[40] Before testing, some of the samples were annealed in a sealed quartz tube at a temperature of 300 °C for 1 week. Subsequent bulk X-ray diffraction characterization confirmed the amorphous structure of the annealed samples. For compression testing, samples were subjected to strain rates of 2×10^{-5} and 2×10^{-4} s^{-1} in the unconstrained condition. A data acquisition rate of 100 Hz was used.

Figures 15(a) through (d) present the detrended stress *vs* time data for the as-cast and thermally-annealed samples that underwent compression at strain rates of 2×10^{-5} and 2×10^{-4} s^{-1}. The serrations for the annealed samples were noticeably different, as compared to those for the as-cast sample. For instance, there were a greater number of serrations in the annealed samples such that the serrated flow appeared more irregular. As for the strain rates, there was also a greater number of stress-drops in the samples that were tested at 2×10^{-4} s^{-1}, for both the as-cast and annealed specimens.

The corresponding sample-entropy results are presented in Figures 16(a) through (d). For all the conditions, the sample-entropy curves increased with the scale factor, indicating that the serrations exhibited complex behavior at all scales. As with a previous investigation,[39] the sample entropy markedly increased with the strain rate. Furthermore, annealing of the sample (300 °C, 1 week) also led to a significant increase in the sample-entropy values. From the above results, it can be said that annealing and increasing the strain rate

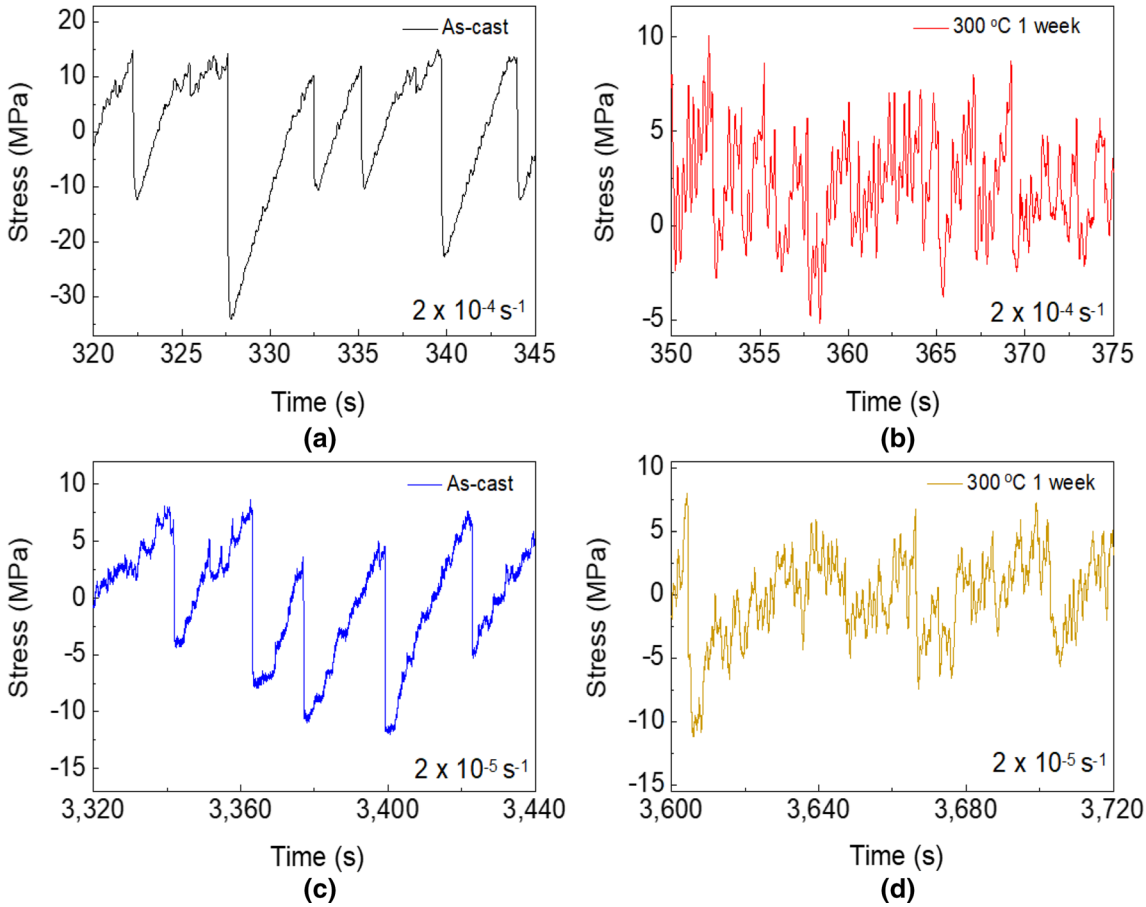

Fig. 15—The detrended stress-time data for the compressed (*a*) as-cast Vitreloy 105 with a strain rate of 2×10^{-4} s^{-1}, (*b*) annealed (300 °C, 1 week) Vitreloy 105 with a strain rate of 2×10^{-4} s^{-1}, (*c*) as-cast Vitreloy 105 with a strain rate of 2×10^{-5} s^{-1}, and (*d*) thermally annealed (300 °C, 1 week) Vitreloy 105 with a strain rate of 2×10^{-5} s^{-1} (Reprinted from Ref. [40] under the terms of the Creative Commons CC BY 4.0).

resulted in an increase in the complexity of the serration behavior in the Vitreloy 105.

It has been reported that annealing of a BMG leads to a decrease in the amount of free-volume defects in the glass.[84,173] Based on the above discussion, it would be expected that annealing should result in a decrease in the complexity of the serrated flow. However, it was surmised that the higher complexity in the annealed sampled was a result of more localized secondary shear bands that exhibit more correlated behavior during the serrated flow.

Liaw's group and his colleagues performed another study on the serration behavior in compression tested Vitreloy 105.[41] Samples were compressed at RT, using a Material Test System (MTS) 810 machine. Here, the sample underwent compression at a strain rate of 2×10^{-3} s^{-1} with a data acquisition rate of 100 Hz. To observe the dynamic surface temperature evolution of the samples during testing, a FLIR SC5000 Infrared (IR) Imaging System with a frame rate of 300 Hz was used.

Figures 17(a) and (b) show both the temperature evolution (blue) and the stress (red) as a function of time. It is apparent that the stress-drops coincide with the abrupt rise in the temperature. Furthermore, the end of the stress-drop is accompanied by the end of the heat-releasing process where the heat band widens due to the heat dissipation. After the stress-drop event, the heat continues propagating to the surrounding low-temperature region, which leads to a significant decrease in the surface temperature. After a certain amount of time, another serration event occurs, and the process repeats. It was also found that temperature bursts occurred during smaller stress-drop events (see Figure 17(b)). Figure 17(c) displays the calculated magnitudes of the temperature rise as a function of the stress-drop values. As can be seen, there is a strong linear correlation between the two quantities.

Importantly, the heat content carries the information regarding the extent to which the sample deformed. Therefore, this quantity should be associated with each individual serration event since this factor is necessary to better understand the shear-band evolution. To help gain a better understanding of this phenomenon, a spatiotemporal modeling procedure was proposed to derive and couple the thermographic data with the heat content for each stress-drop event. To accomplish this goal, the temperature change during a serration was calculated *via* a one dimensional thin-film based heat-diffusion equation[41]:

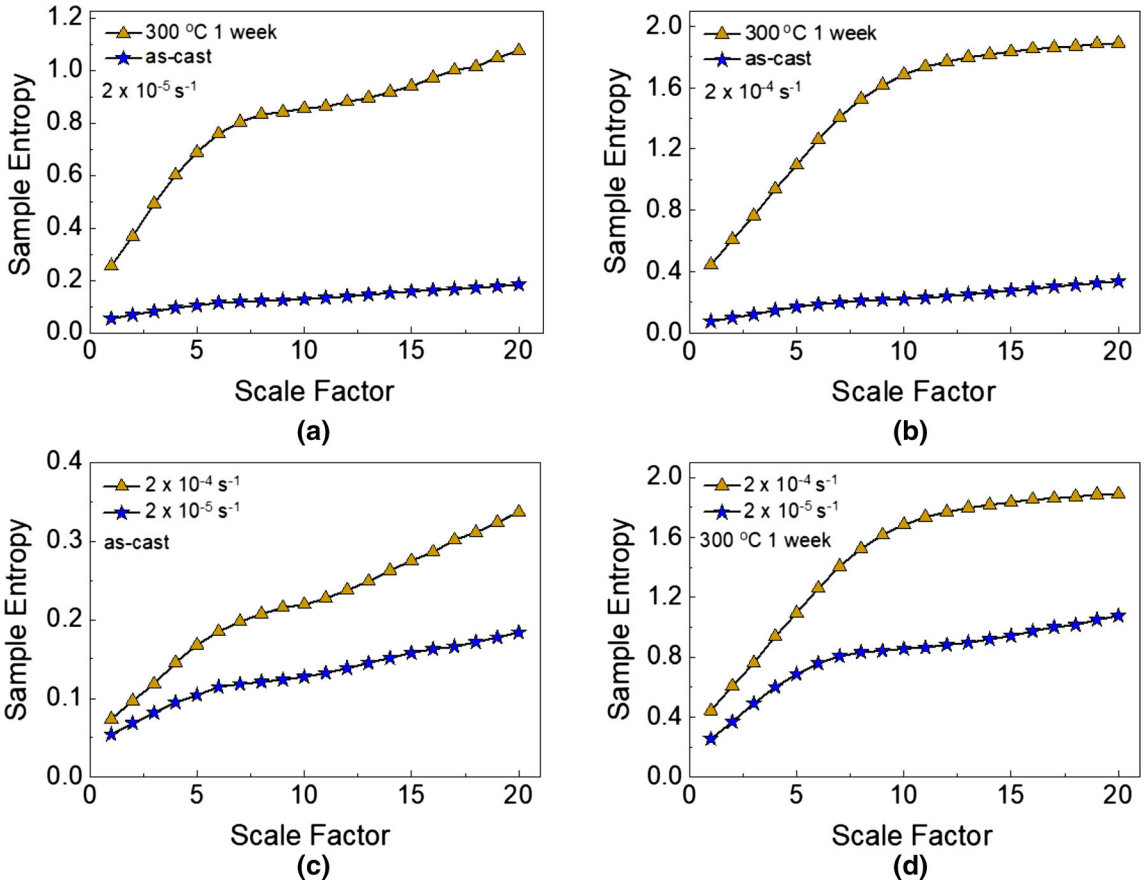

Fig. 16—The sample entropy, as a function of the scale factor, for the compression tested (*a*) as-cast Vitreloy 105 with a strain rate of 2×10^{-4} s^{-1}, (*b*) thermally-annealed (300 °C, 1 week) Vitreloy 105 with a strain rate of 2×10^{-4} s^{-1}, (*c*) as-cast Vitreloy 105 with a strain rate of 2×10^{-5} s^{-1}, and (*d*) thermally-annealed (300 °C, 1 week) Vitreloy 105 with a strain rate of 2×10^{-5} s^{-1} (Reprinted from Ref. [40] under the terms of the Creative Commons CC BY 4.0).

$$\Delta T = \frac{H}{\rho C_p} \cdot \frac{1}{\sqrt{4\pi\alpha(t+t_c)}} e^{-\frac{x^2}{4\alpha(t+t_c)}} \quad [9]$$

where H is the heat content, ρ (6730 kg/m^3 [174]) is the density, C_p (330 J/kg K[175]) is the specific heat capacity of the Vitreloy 105 BMG, t is the elapsed time from the first frame, t_c is the time between the beginning of the heat generation and first frame camera captured, x is the distance from the shear-band center, and α is the thermal diffusivity (3×10^{-6} m^2/s[106]) of the Vitreloy 105 BMG. From Eq. [9], one can solve for H and t_c, using the experimentally determined temperature profile during a serration event.

The thermal profile and temperature distribution (as a function of space and time) can be observed in Figures 18(a) and (b). A surface-fitting technique that is based on the globally-optimized least-squares method was used to determine H and t_c. Then, the H was plotted with respect to the accumulated energy stored for each serration event, which was calculated from the stress–stress curves (see Figure 18(c)). From the results, it was determined that the average conversion rate of the stored energy to the heat is 0.71 ± 0.17.

From the results, the authors made several important conclusions.[41] Firstly, the local temperature increase amplifies the thermal fluctuations of atoms that further facilitate the activity of STZs. These fluctuations affect their surroundings in such a manner that may eventually trigger an avalanche of STZ activities, resulting in the stress-drop event. Second, shear banding results in an increase in the free-volume content in the shear-band plane that increases the likelihood that another shear-band initiation will occur here, as compared to other planes. Third, the deformation during the serrated flow can be divided into two stages, namely immature and mature shear-band stages. During the first stage, a shear-band plane is formed that acts as a potential sliding path. Here, the heat generated at the top and bottom ends of the shear-band plane correspond to non-uniform heat generation inside this plane. During the second stage, the activated weak zones percolate from both ends of the shear-band plane such that a continued heat band forms as more heat is generated.

2. *Fatigue behaviors*

In addition to examining the serrated flow in BMGs, Dr. Liaw's group and his colleagues have also performed very important research regarding the fatigue behavior in this type of material system.[32,176–180] For example, Liaw's group and his colleagues compared the fatigue behavior of a zirconium-based BMG,

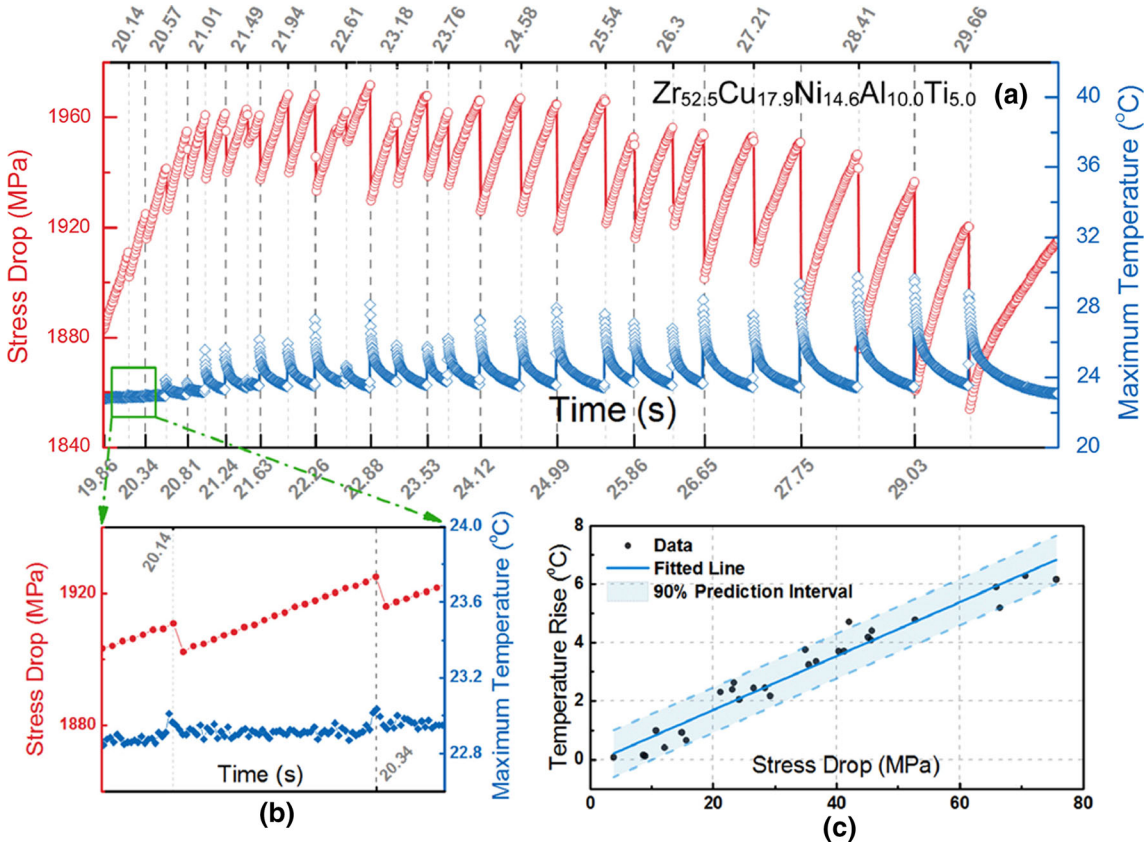

Fig. 17—(*a*) The stress-drop *vs* time and maximum temperature data for each frame, (*b*) a magnified region for times ranging from 19.9 to 20.5 s from (*a*), as demarcated by the green rectangle, and (*c*) the linear relationship between the stress-drop values and the temperature. (reproduced from Ref. [41] with permission).

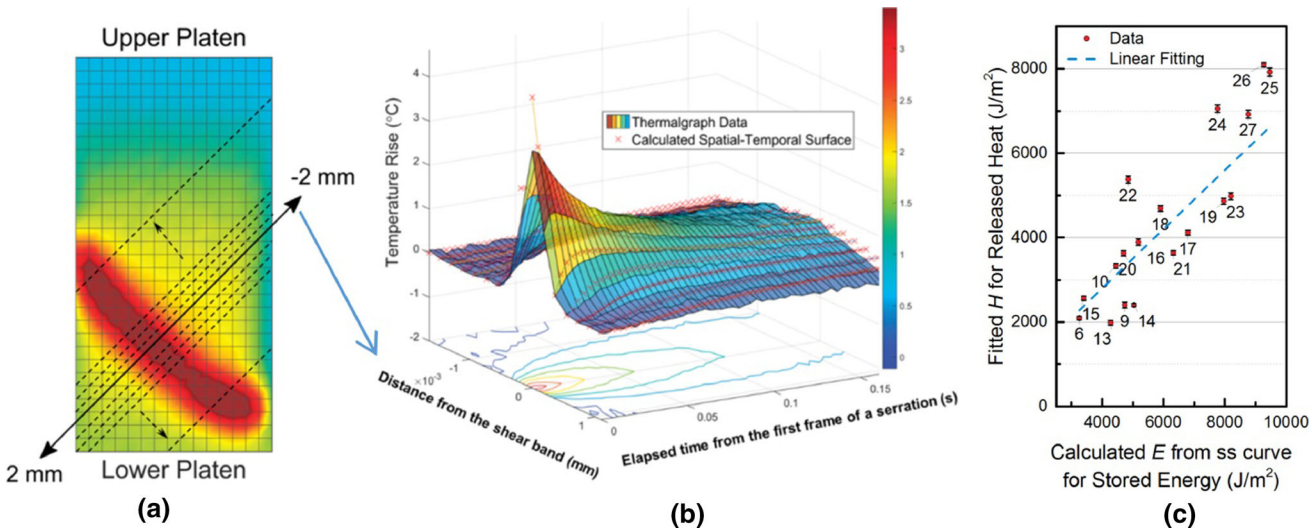

Fig. 18—(*a*) The linear profile of the temperature data that was used for the spatial calculation. The lines represent the data used to achieve average values. (*b*) Spatial-temporal surface modeling of the temperature data from the thermograph. (*c*) The relationship between the released heat and the stored energy that was obtained from the spatial-temporal surface. The marked numbers indicate the sequence of serration events (reproduced from Ref. [41] with permission).

Zr-10Al-5Ti-17.9Cu-14.6Ni [fabricated at the Oak Ridge National Laboratory (BAM-11) and developed at the California Institute of Technology (Vitreloy 105)] with other high-strength alloys such as D6AC steel, Ti-6Al-4V alloy, and 300 M steel.[32,176] For the experiments, the BAM-11 BMG round-bar notched samples underwent tension fatigue testing at various stress ranges with a load ratio (R) of 0.1 (minimum/maximum

stress) and a frequency of 10 Hz. Each fatigue test was conducted until sample failure or for a total of 10^7 cycles. The fatigue-endurance limit, which is based on the applied stress range defined at 10^7 cycles, for the above BMG was found to be 907 MPa. Furthermore, the fatigue ratio, which is the fatigue-endurance limit divided by the ultimate tensile strength, was determined to be 0.53. Figure 19 shows the stress-range/fatigue life for Vitreloy 105 BMG and other alloys. The former displays noticeably greater values, as compared to the other materials. However, the authors noted that these comparatively better fatigue properties that were exhibited by the BMG may have been related to the differences in the chemical composition and/or the variations in specimen geometries and testing procedures.

In a later study, Liaw's group and his colleagues examined the four-point-bending fatigue behavior of a Vitreloy 105 BMG.[177] Here, samples were subjected to RT bending tests at frequencies of 10 Hz and a load ratio of 0.1. The fatigue tests were performed until sample failure or for a total of 10^7 fatigue cycles. The fatigue-endurance limit, which is based on the stress amplitude, was determined to be ~ 425 MPa, which is equivalent to a fatigue ratio of 0.25. SEM imaging revealed the presence of particles on the fracture surfaces (see Figures 20(a) through (d) and 21(a) and (d)).

Specifically, there were three types of particles observed on the fracture surface. The first set of particles had diameters that ranged from 5 to 20 μm and located in isolated or small groups (see Figure 20). The second group of particles, which can be seen in Figures 21(a) through (d), formed arcs across the fracture surface. Similar to the first set of particles, most of the arcs consisted of particles that had diameters of 5 to 20 μm. The last set of particles, which were contained in "large sheets" of material, were smaller than the other two sets where their diameters ranged from 3 to 5 μm (see Figures 22(a) through (c)). These particles are Al-, Ti-, Cu-, Ni-rich oxides. Importantly, it was determined from the results that the fatigue lifetime was inversely proportional to the quantity of the particles observed.

In a more recent study, Liaw's group and his colleagues developed the first statistical framework for modeling the S–N behavior in BMGs.[178] For the experiment, they performed four-point-bending tests on a $Zr_{50}Cu_{30}Al_{10}Ni_{10}$ BMG samples with an inner span of 10 mm and outer span of 20 mm.

Furthermore, samples were subjected to a load ratio of 0.1, and a sinusoidal waveform was employed with a frequency of 10 Hz. One of the models that they developed to analyze the fatigue behavior, which is based on a Weibull distribution, was a size-effect fatigue-life model that incorporated a mechanistic understanding of fatigue failure in BMGs. The model is written as:

$$F(N|\beta,\theta_0(S)) = 1 - e^{-h^{-1}\left(\frac{N}{\theta_0(S)}\right)^{\beta}} \quad [10]$$

where N is the number of cycles to failure, β is a Weibull shape parameter, h is the thickness of the material under bending, and $\theta_0(S)$ is a stress-dependent Weibull scale parameter that is given by:

$$\log(\theta_0(S)) = \eta_0 + \eta_1 \log(S - S_0(h)), \quad S > S_0(h) \quad [11]$$

here η_0 and η_1 are material based fitting parameters. The importance of the model arises from its mechanistic understanding as to how shear bands affect the fatigue

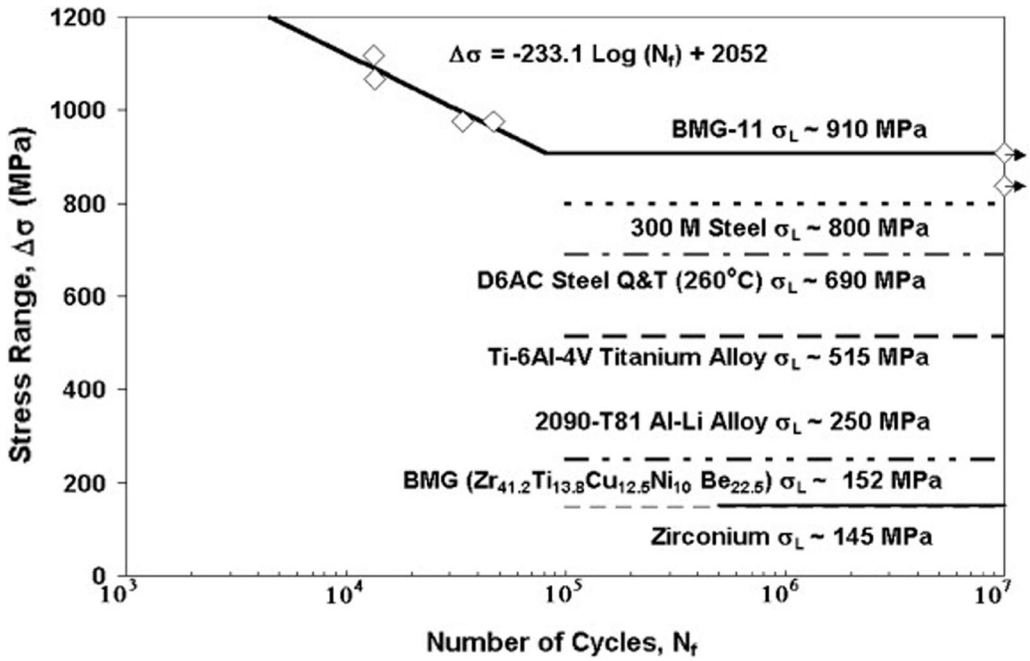

Fig. 19—The stress-range/fatigue-life data of notched Vitreloy 105 (BAM-11) specimens tested in air and compared with the fatigue endurance limits of high-strength alloys (reproduced from Ref. [32] with permission).

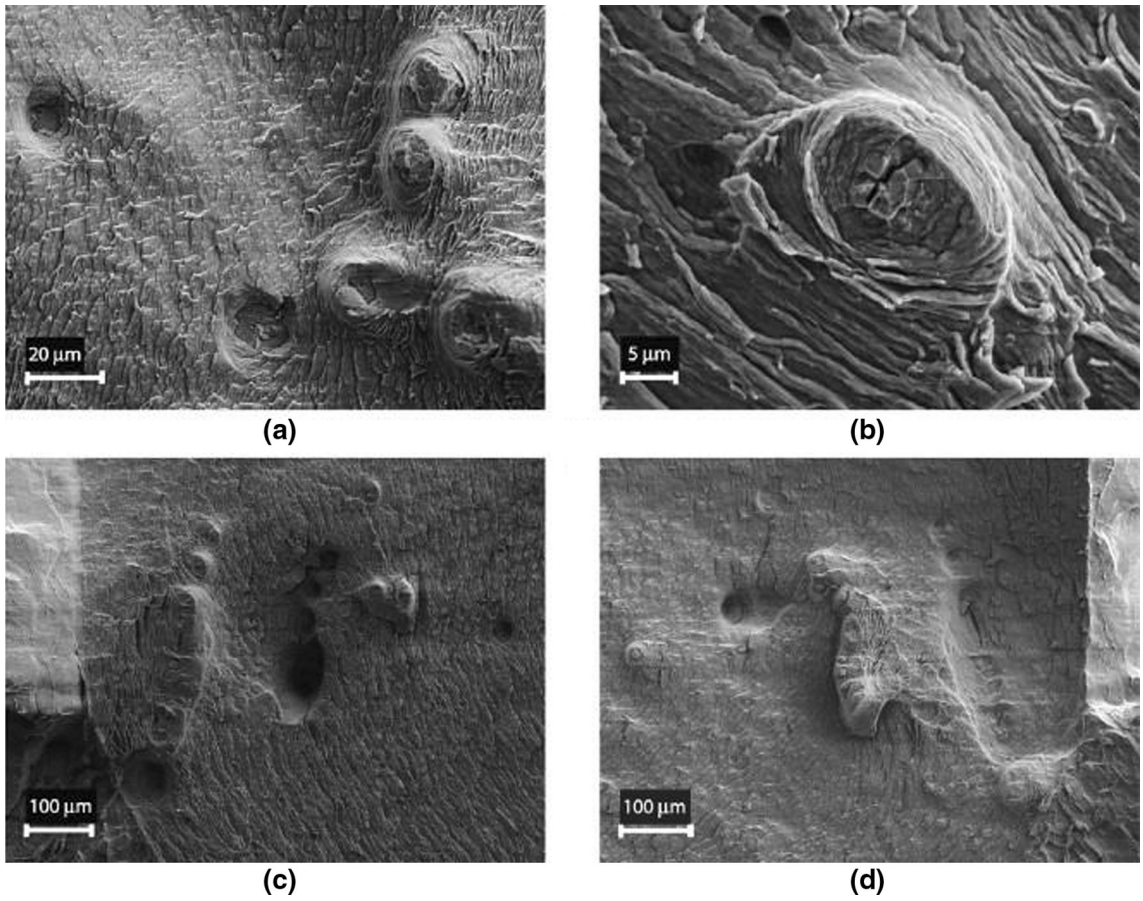

Fig. 20—Fractographs of the particle-and-crater morphology in (*a*) small groups and (*b*) in isolation. The particles on the fracture surface in (*c*) corresponded to craters on the opposite surface in (*d*), and *vice-versa* (reproduced from Ref. [177] with permission).

and failure tolerance of the BMG. Figure 23 displays the median fatigue lives in addition to the 95 pct predictive intervals, as predicted by the model from Eq. [10] for the $Zr_{50}Cu_{30}Al_{10}Ni_{10}$ BMG. Here, data was based on samples with thicknesses of 2 and 3 mm. In Figure 23, thicker samples with less numbers of shear bands tend to exhibit greater fatigue life. The findings indicated that the results of the model support the theory that the number of shear bands formed during the bending tests can play a role in the fatigue life of the BMG.

3. *Corrosion resistance studies*

Hua *et al.*[181] compared the corrosive-wear resistance of a $Pd_{40}Cu_{30}Ni_{10}P_{20}$ BMG to conventional alloys, such as CoCrMo, 316L stainless steel, and Ti6Al4V alloys. Here, the samples were exposed to a phosphate buffer solution (PBS) and were then characterized, using multiple techniques, including wear experiments and potentiodynamic-polarization tests (PPTs). Figure 24 presents the results of the wear tests where the BMG displayed lower wear rates, as compared to the other alloys for sliding in air (dry) and PBS. The results of the PPTs is displayed in Figure 25 for the four materials. It was determined that the corrosion potentials of the Pd-based BMG, CoCrMo alloy, 316 L SS, and Ti6Al4V alloy were − 0.14, − 0.74, − 0.39, and − 0.47 V, respectively. This result indicates that the BMG exhibited a comparatively-greater surface stability, and hence corrosion resistance, as compared to the other alloys.

In a similar study, Hua *et al.*[182] compared the behavior of a $Fe_{41}Co_7Cr_{15}Mo_{14}C_{15}B_6Y_2$ BMG with a CoCrMo alloy and 316L stainless steel. They found that the wear rate was considerably lower, as compared to the other materials (see Figure 26). Furthermore, the BMG that was exposed to PBS had a lower wear rate, as compared to the dry condition. This trend is in contrast with the CoCrMo and 316 stainless steel where the wear rate increased. It was also reported that the Fe-based BMG exhibited the lowest corrosion current density during tribo-corrosion testing. The good anti-corrosion behavior of the Fe-based BMG was attributed to the protective surface oxide film that forms during exposure to the PBS. It was also suggested that $FeMoO_4$ could be formed on the surface, which hinders the propagation of the corrosion pit.[183] From the results, the authors surmised that the comparatively-good corrosion resistance that was exhibited by the BMG makes it an excellent candidate for biomedical applications.

Hua *et al.* also investigated the effects of partial crystallization on the corrosion performance of a $Zr_{68}Al_8Ni_8Cu_{16}$ BMG.[18] To induce crystallization in the BMG, samples were annealed at temperatures ranging from 673 K to 773 K using a ramp rate of

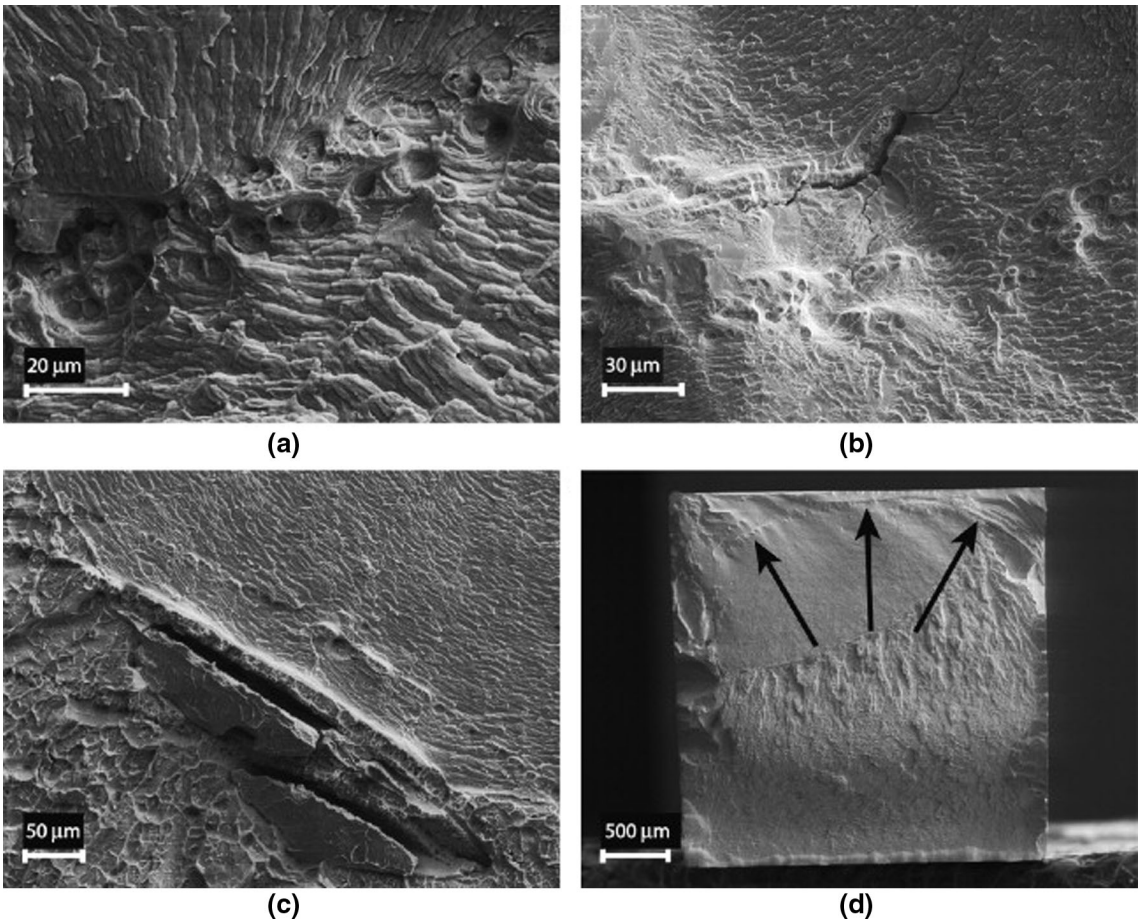

Fig. 21—Fractographs of (*a–c*) short and (*d*) long arcs of particles observed on the fracture surfaces of the bend samples. The arrows in (*d*) denote the arc of particles across the top portion of the bend sample[177] with permission.

20 °C/min. To minimize oxidation, samples were heated in pure argon. XRD determined that the crystallized samples contained Zr_2Ni and Zr_2Cu crystalline phases (see Figure 27). Further analysis of the patterns revealed that for annealing temperatures of 673 K and 713 K, the crystallinity of these phases was 10 and 77 pct, respectively. For the corrosion tests, PPTs were performed in which as-cast and annealed samples (673 K and 713 K) were immersed in a 1 M HCl solution for 1 week. The results of the tests showed that crystallization led to an increase in the corrosion current density. More specifically, this value increased from 1.42×10^{-3} A/m^2 for the as-cast sample to 2.55×10^{-3} and 1.68×10^{-2} A/m^2 for the samples annealed at 673 K and 713 K, respectively. Such a result indicates that crystallization of the BMG reduced the corrosion resistance of the alloy.

To complement the PPTs, weight loss measurements were performed to determine the corrosion rate of the samples. Figure 28 features the corrosion rate for the three samples, which are labeled Zr68A (as-cast), Zr68B (673 K), and Zr68C (713 K). It was determined that the weight loss of the as-cast, 673 K annealed, and 713 K annealed samples were 5.36, 5.95, and 7.95 g/m^{2}h, respectively. This result further corroborates those of the PPTs, where crystallizing the BMG reduced the corrosion resistance of the alloy.

III. RESEARCH ON HIGH-ENTROPY ALLOYS

A. *Design of New HEAs via Thermodynamic Calculations*

The empirical formation rules,[31] which were previously discussed from Section I, can provide an effective way to select solid-solution HEAs from alloy composition pools. However, this alloy-design approach could not provide either the structural information or the effects of temperature on phase formation in HEAs. To overcome this issue, Liaw's group and his colleagues have designed new HEAs, using the thermodynamic approach, *i.e.*, CALculation of PHAse Diagrams (CALPAHD) simulations.[43,44,46,49,55,77] Coupled with appropriate elemental databases, the multicomponent-phase diagram for HEAs can be predicted, prior to fabrication. CALPHAD describes the thermodynamic properties using phenomenological models. Thermodynamic and phase equilibria data are utilized to calculate the Gibbs free energies (G) for multicomponent systems, which can be described as:

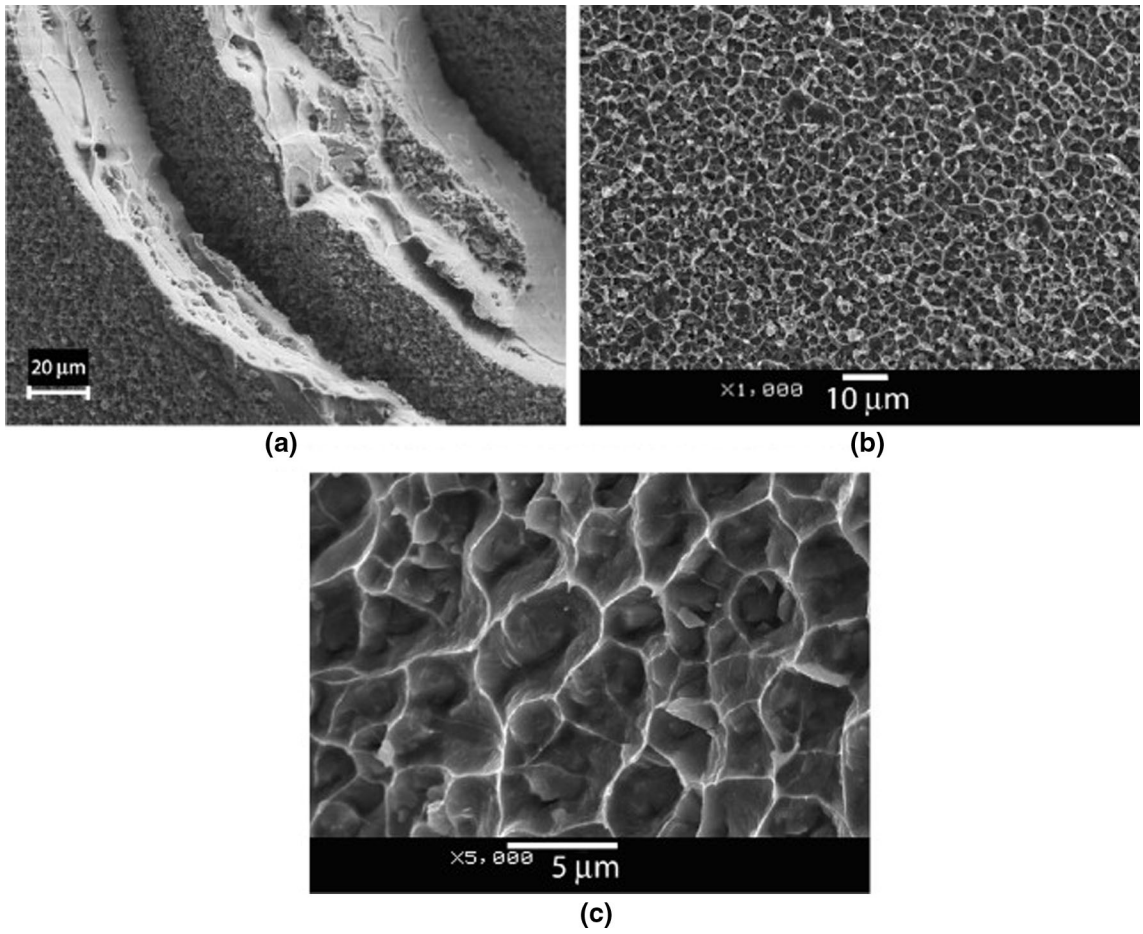

Fig. 22—SEM fractographs illustrating the morphology of (*a*) multiple large sheets of small particles that commonly form concentric arcs across the fracture surfaces in various locations. (*b* and *c*) Low and high-magnification images of a single sheet of particles (reproduced from Ref. [177] with permission).

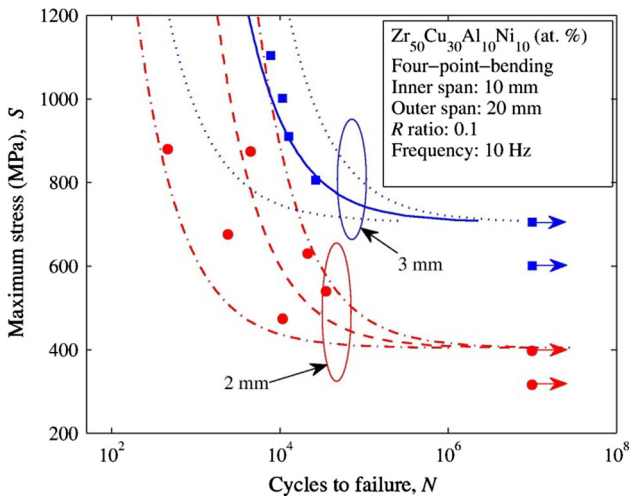

Fig. 23—Predictive results for the model represented by Eq. [10] (solid line: median fatigue life when $h = 3$ mm; dotted line: 95 pct predictive interval for fatigue life when $h = 3$ mm; dashed line: median fatigue life when $h = 2$ mm; dashed–dotted line: 95 pct predictive interval for fatigue life when $h = 2$ mm) (reproduced from Ref. [178] with permission).

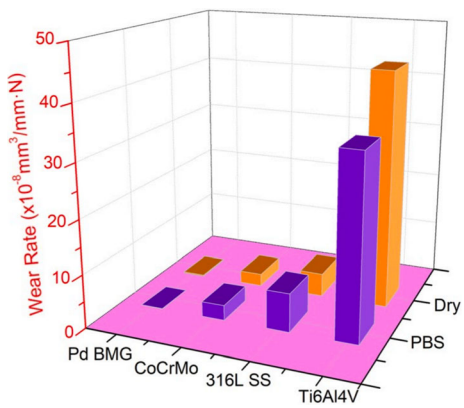

Fig. 24—Wear rates for the Pd-based BMG, CoCrMo alloy, 316 L stainless steel, and Ti6Al4V during sliding in air and the PBS solution (reproduced from Ref. [181] with permission).

$$G = \sum_{i}^{n} X_i G_i^0 + \Delta G^{\text{mix}} \qquad [12]$$

where X_i is the composition of the component, i, G_i^0 is the Gibbs energy of the component, i, and ΔG^{mix} is

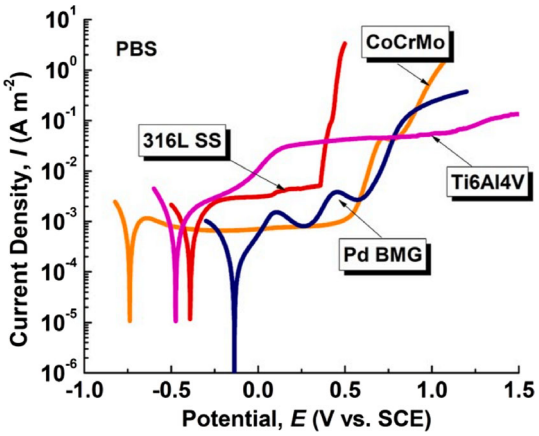

Fig. 25—Current density *vs* potential, as determined from the PPTs for the Pd-based BMG, CoCrMo alloy, 316 L stainless steel, and Ti6Al4V (reproduced from Ref. [181] with permission).

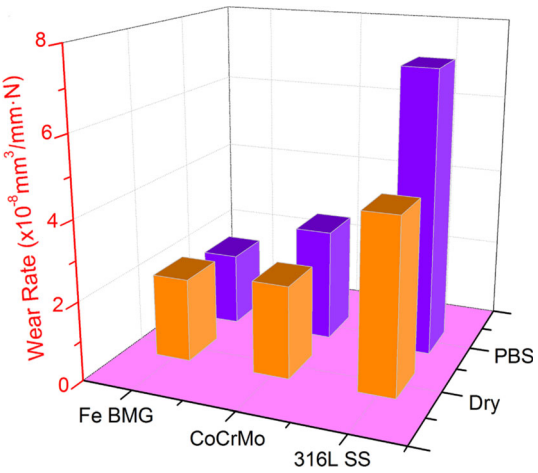

Fig. 26—Wear rates for the Fe-based BMG, CoCrMo alloy, and 316L stainless steel during sliding in air and the PBS solution (reproduced from Ref. [182] with permission).

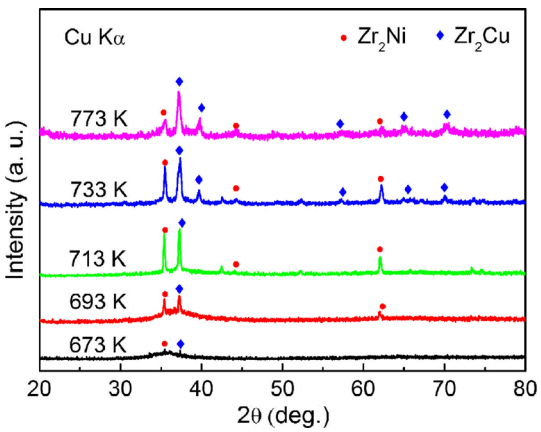

Fig. 27—The XRD patterns for the $Zr_{68}Al_8Ni_8Cu_{16}$ BMG annealed at temperatures ranging from 673 to 773 K (reproduced from Ref. [18] with permission).

the change of the Gibbs energy when mixing components, which can be expanded as:

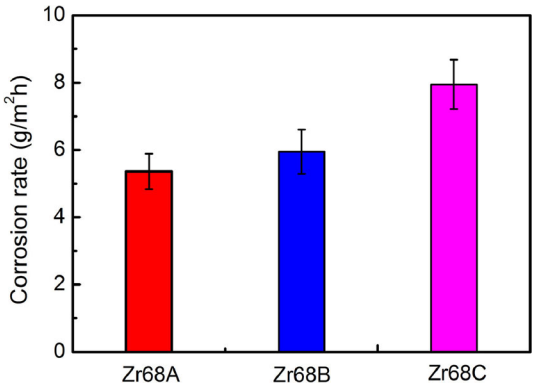

Fig. 28—Corrosion rates of the $Zr_{68}Al_8Ni_8Cu_{16}$ BMG samples for the as-cast (Zr68A), 673 K (Zr68B) and 773 K (Zr68C) conditions (reproduced from Ref. [18] with permission).

$$\Delta G^{\text{mix}} = \Delta^{\text{mix}}_{\text{ideal}} + G^{\text{XS}} = -TS^{\text{mix}}_{\text{ideal}} + G^{\text{XS}} \qquad [13]$$

where $\Delta G^{\text{mix}}_{\text{ideal}}$ is the ideal part of the change of the Gibbs energy when mixing, T is the temperature, $S^{\text{mix}}_{\text{ideal}}$ is the ideal configurational entropy (can be calculated as $R\sum X_i \ln X_i$), and G^{XS} is the excess Gibbs energy, which includes the non-ideal mixing enthalpy and entropy.

Using CALPHAD simulations, Liaw's group and his colleagues have designed large numbers of HEA compositions. In collaboration with Drs. Michael C. Gao and Chuan Zhang, his group has focused more on the design of Al-containing HEAs (Al_xCoCrFeNi),[43,46,55] lightweight HEAs (Al_xCrFeMnTi$_x$),[44,45] and refractory HEAs (NbTaTiV),[49,184] in which the results of their simulation efforts can be observed in Figure 29.

Figure 29(a) shows the calculated vertical section of the Al_xCoCrFeNi with x varying between 0 and 2. This predicted phase diagram clearly indicates that the phase relation is very sensitive to the Al contents in the Al_xCoCrFeNi HEA. The single-phase FCC can only be produced when the Al ratio is kept small, while the BCC and/or B2 phases will precipitate if a higher Al ratio is used, and a mixture of FCC + BCC phases and/or B2 phase should form when x is an intermediate value. In order to provide a better understanding of the stable phases and their fractions as well as the distribution of each alloying element within the different phases of the Al_xCoCrFeNi (x = 0.3, 0.5, and 0.7) HEA, equilibrium calculations were performed, as shown in right side of Figure 29(a). For the $Al_{0.3}$CoCrFeNi HEA, two kinds of disordered BCC phases were present at low temperatures. Furthermore, the sigma phase forms at temperatures below 720 °C but disappears at 350 °C, and the ordered $L1_2$ phase could form below 600 °C. With the increase of temperature, the ordered B2 phase forms at 1026 °C, but then the only single FCC phase could be found at temperatures ranging from 1,026 °C to 1402 °C. In the $Al_{0.5}$CoCrFeNi HEA, the ordered B2 phase could form in a larger temperature range that varied from 200 °C to 1350 °C. It was also found that the sigma phase begins to form at a temperature of 820 °C. Furthermore, the ordered $L1_2$ and disordered BCC phases could form at low temperatures. On the

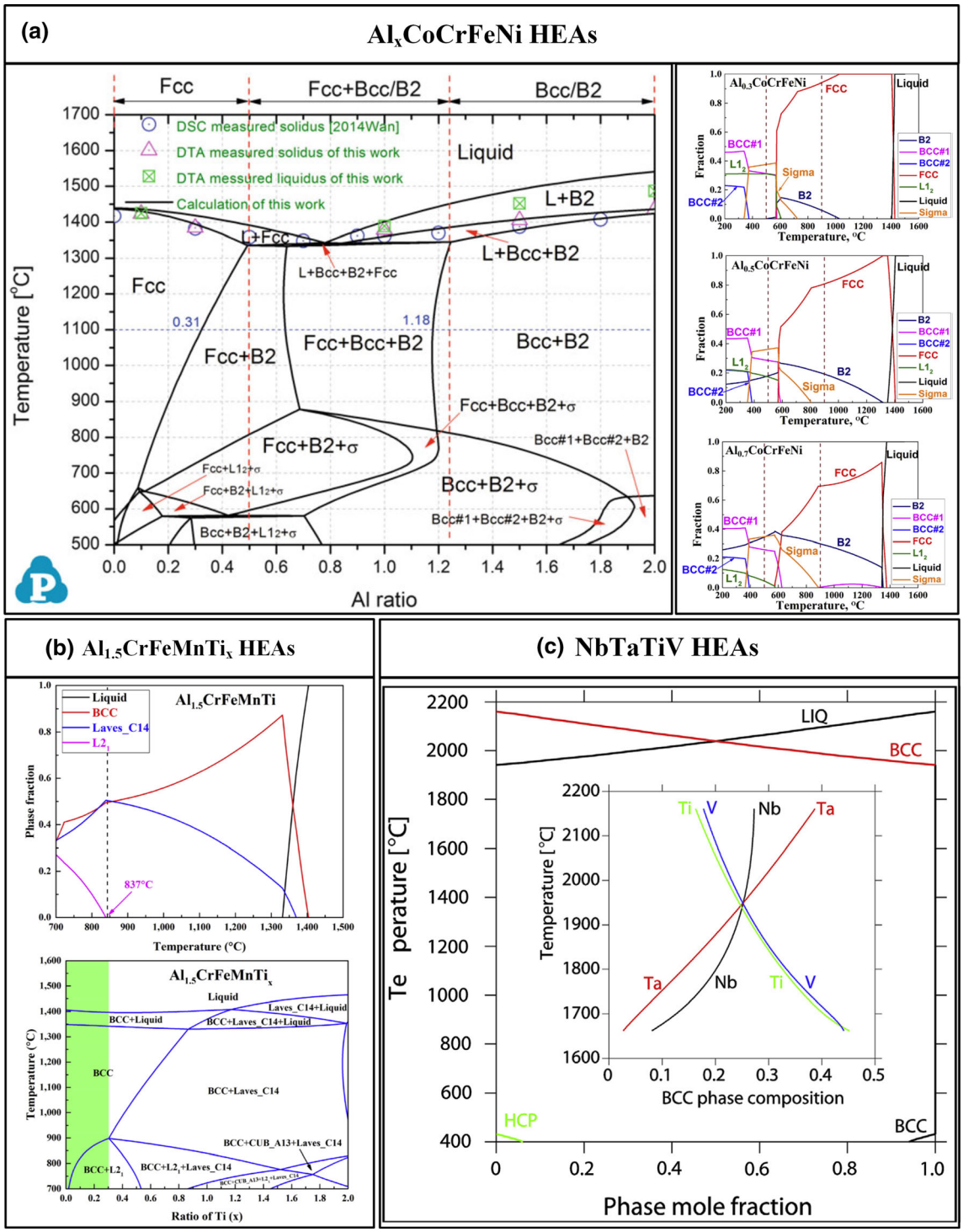

Fig. 29—CALPHAD-calculation data for (*a*) AlxCoCrFeNi HEA, (*b*) $Al_{1.5}CrFeMnTi_x$, and (*c*) NbTaTiV HEAs (reproduced from Ref. [45], [48], [49], [185] with permission).

other hand, the BCC phase is observed in a temperature range of 900 °C to 1350 °C for the $Al_{0.7}CoCrFeNi$ HEA. In addition, the sigma phase disappears at 350 °C, which was similarly observed in $Al_{0.3}CoCrFeNi$ and $Al_{0.5}CoCrFeNi$ HEAs. The trend of formation of $L1_2$ and two disordered BCC phases are also the same with $Al_{0.3}CoCrFeNi$ and $Al_{0.5}CoCrFeNi$ alloys.

The lightweight HEAs with the composition of $Al_{1.5}CrFeMnTi_x$ have also been designed by Liaw's group and his colleagues,[44,45] as presented in Figure 29(b). The BCC phase is the first one to form at about 1403 °C in the $Al_{1.5}CrFeMnTi$ alloy, and it is the primary phase in the higher temperature range of 700 °C to 1360 °C. It was also found that the fraction of

the C14 phase was relatively high (about 45 pct at 800 °C). According to the thermodynamic information, the $L2_1$ phase is stable at temperatures below 837 °C. Furthermore, the calculated isopleth of the $Al_{1.5}CrFeMnTi_x$ HEA (Figure 29(b)) indicate that the constituent phases (BCC + L21 + Laves-C14 structures) in the present composition of the $Al_{1.5}CrFeMnTi$ alloy. It is worth noting that a BCC + L21 two-phase region is observed in the calculated isopleth [highlighted by the light green region in Figure 29(b)].

In addition to the Al-containing and lightweight HEAs, Liaw's group in collaboration with Dr. Michael C. Gao have moved to design the refractory-type HEAs, as presented in Figure 29(c).[49] The predicted equilibrium and non-equilibrium phase mole fraction versus temperature plots for the NbTaTiV refractory HEA are illustrated in Figure 29(c). A single BCC solid-solution is predicted to form within the bulk composition of the $Nb_{23.8}Ta_{25.5}Ti_{24.9}V_{25.8}$ HEA, at. pct. Moreover, the calculated liquidus and solidus temperatures were calculated to be T_{liq} = 2161 °C and T_{sol} = 1941 °C, respectively. The BCC solid-solution decomposes into a minor HCP phase at the T_{dec} = 432 °C. The simulation predicts the formation of a single BCC solid solution with chemical segregation associated with Ta, Ti, and V during the entire non-equilibrium solidification. It is also found that the BCC phase is rich in Ta at earlier stages of solidification in the dendritic arms, while the interdendritic region is enriched in Ti and V in the latter stages, as the temperature decreases.

B. *Microstructural and Mechanical Properties of Various HEAs*

1. *Microstructural and mechanical properties of Al-containing HEAs*

The various, newly-designed HEAs, as determined by CALPHAD simulations (see above), have been experimentally verified by phase-identification methods, microstructural-investigations, and mechanical-behavior studies. These alloys include Al-containing (Al_xCoCrFeNi), lightweight HEAs ($Al_xCrFeMnTi_x$), and refractory HEAs (NbTaTiV). Figure 30 displays the features of the microstructures, phase constitutions, and phase fractions of both FCC and BCC/B2 phases in Al_xCoCrFeNi HEAs (x = 0.3, 0.5, and 0.7) after the homogenization treatment at 1250 °C.[48,55] The formation of a single solid-solution FCC phase (A1) in the $Al_{0.3}$CoCrFeNi HEA was observed from the back-scattered-electron (BSE) images and electron backscatter diffraction (EBSD) results, as exhibited in Figures 30(a) and (b). The randomly oriented equiaxed grains with a size of about 300 μm are clearly observed from the phase-identification map (Figure 30(c)). Note that the annealing twins also formed during the heat treatment. The $Al_{0.5}$CoCrFeNi HEA consists of the FCC (A1) and B2 phases with the volume fractions of 98 and 2 pct, respectively (Figures 30(d) through (f)). The microstructure was dramatically changed with an increase in the Al content to x = 0.7. Additionally, as presented in Figures 30(g) through (i), the formation of the solid-solution FCC (Al) phase with solid-solution BCC (A2) + B2 phases can be clearly observed. The volume fraction of the A2/B2 phases is 22 pct, which consists of the randomly-orientated FCC (Al) phase and [101]-oriented BCC (A2) + B2 phases. The phase identification of Al_xCoCrFeNi HEAs have further been obtained via neutron diffraction (ND), as shown in Figure 30(j). As consistent with these microstructural investigations, the $Al_{0.3}$CoCrFeNi HEA consists of a single FCC phase (A1), while the $Al_{0.7}$CoCrFeNi HEA has a combination of FCC (A1), BCC (A2), and B2 phases. The nano-scale structures for Al_xCoCrFeNi (x = 0.5 and 0.7) were further investigated by TEM, in which the results are featured in Figures 30(k) and (l). The presence of the B2 phase in the $Al_{0.5}$CoCrFeNi HEA was confirmed by the dark-field image, which is produced by the super-lattice spot (100). For the $Al_{0.7}$CoCrFeNi HEA, the TEM images of the BCC-structured phases indicate the formation of a BCC (A2) phase in the B2 matrix.

Figure 31 presents the tensile engineering stress-strain curves of the Al_xCoCrFeNi HEA subjected to a strain rate of 2×10^{-4} s^{-1} at RT.[48] The tensile yield strength (σ_y) and ductility of the $Al_{0.3}$CoCrFeNi HEA are 210 MPa and 97 pct, respectively. The yield strength is significantly improved when the Al content is increased whereas the ductility of the Al_xCoCrFeNi HEA is gradually decreased. The detailed values for the yield strength and ductility of the Al_xCoCrFeNi HEA (x = 0.3, 0.5, and 0.7) are listed in the Figure 31.

As seen in Figure 31, the $Al_{0.5}$CoCrFeNi HEA has an excellent combination of yield strength and ductility among the Al-containing HEAs. These exceptional properties eventually led Liaw's group and his colleagues to further study the additional mechanical properties, *i.e.*, fatigue behavior of this alloy.[52,53] The four-point bending high-cycle fatigue experiments were conducted at various applied loads or cycles until either specimen failure or 10^7 cycles were completed. Figure 32(a) shows the four-point-bending fatigue results plotted as the stress range versus the number of cycles to failure (or 10^7 cycles) to give the stress number of cycles to failure (S–N) curve. The maximum stress was calculated by the equation, $\sigma = \frac{3P(S_0 - S_i)}{2BW^2}$, where P is the applied load, S_0 is the outer span length (20 mm), S_i is the inner span length (10 mm), B is the thickness (3 mm), and W is the height (3 mm) of specimens. The typical fatigue behaviors for the above HEAs were obtained, indicating that the number of cycles to failure increases with a decrease in the stress level. Most of the sample failures occurred within 35,000 to 450,000 cycles with the maximum stress level of 1250 MPa. However, overall, the data points of the fatigue tests were noticeably scattered at various stress levels, especially in the lower stress ranges. The scattering of fatigue life in the S–N curve (Figure 32(a)) is probably due to the presence of different defect densities or microcracks in the samples. The ranges of fatigue-endurance limits, which were estimated by the Weibull mixture predictive model are 540 to 945 MPa. Based on the obtained results of four-point bending high cycle fatigue tests, Liaw's group and his colleagues further predict the fatigue life of the HEAs using the statistical models,

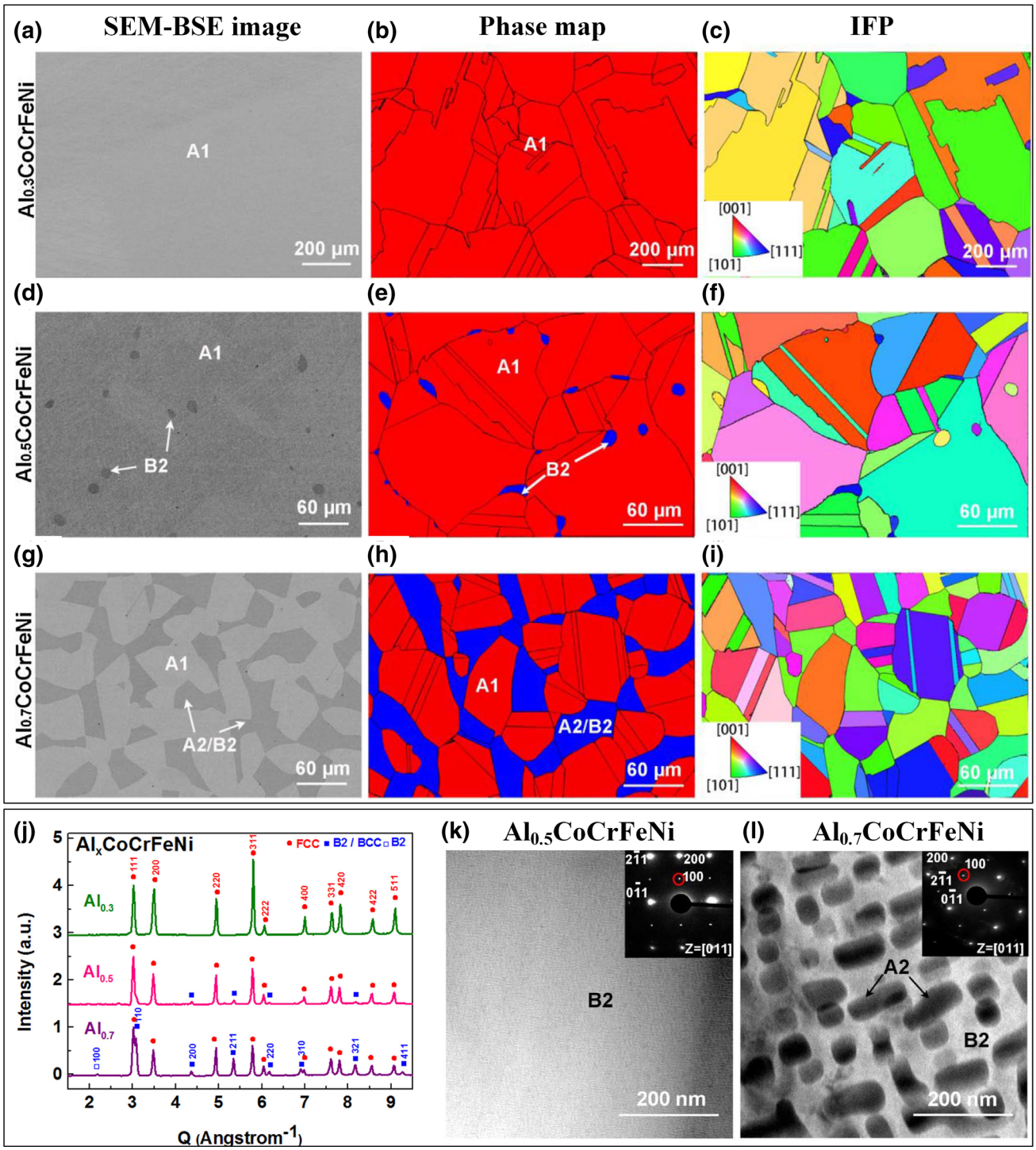

Fig. 30—The SEM-BSE images, phase map, and inverse pole-figure (IPF) of the homogenized (*a* to *c*) $Al_{0.3}CoCrFeNi$, (*d* to *f*) $Al_{0.5}CoCrFeNi$, and (*g* to *i*) $Al_{0.7}CoCrFeNi$ HEAs. (*j*) Neutron-diffraction pattern of the $Al_xCoCrFeNi$ HEA. Characterization of a disordered/ordered BCC phase (A2/B2) by the dark-field TEM in (*k*) $Al_{0.5}CoCrFeNi$ and (*l*) $Al_{0.7}CoCrFeNi$ HEAs (reproduced from Ref. [48], [55] with permission).

such as a Weibull predictive and Weibull mixture predictive models.[52,53] The results of the Weibull mixture predictive model show that data points of the $Al_{0.5}CoCrFeNi$ HEA can be categorized by two groups, as the strong and weak groups, which depends on the amounts of defects. The strong group has a predicted median time to failure of greater than 10^7 at 858 MPa. The fatigue ratio between the fatigue-endurance limit (based on the stress range) to ultimate tensile strength is 0.402 to 0.703, which are comparable with conventional materials, as illustrated in Figures 32(b) and (c). As seen in Figures 32(b) and (c), some of the materials, such as ultra-high strength steels and wrought aluminum alloy, show the lower fatigue ratios than HEAs, even though

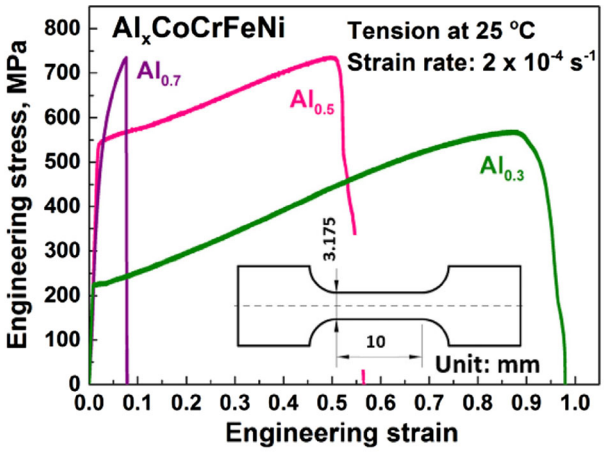

Alloys	Yield strength, σ_y (MPa)	Plastic strain, ε_p (%)
$Al_{0.3}CoCrFeNi$	210	97
$Al_{0.5}CoCrFeNi$	550	56
$Al_{0.7}CoCrFeNi$	600	8

Fig. 31—Tensile engineering stress-strain curves for $Al_xCoCrFeNi$ HEAs (x = 0.3, 0.5, and 0.7) (reproduced from Ref. [48] with permission).

they have higher tensile strengths. Overall, the fatigue limit of HEAs is significantly higher than other conventional alloys, indicating that the HEA have great potential for use in structural applications.

2. *Fatigue behavior of HEAs*

Recently, Li *et al.*,[186] have further reviewed the reported fatigue properties of HEAs to discover and design the good fatigue-resistant HEAs. Figure 33(a) shows the summarized plots of fatigue endurance limit (fatigue strength) versus ultimate tensile strength for various metallic materials. It was found that the fatigue strength of the CoCuFeMnNi HEA is higher than most of conventional alloys except steels, Ni-based superalloys, and BMGs. However, the multi-phase $Al_xCoCrFeNi_x$ HEAs indicate higher and similar fatigue strengths than the CoCuFeMnNi HEA, steels, Ni-based superalloys, and BMGs, whereas the metastable Fe-Mn-Co-Cr-Si-Cu HEA system shows higher fatigue strength than other conventional alloys. Li *et al.* have also summarized the fatigue ratio (based on stress amplitude) *vs* ultimate tensile strengths of HEAs and conventional alloys, as shown in Figure 33(b). As similar to the average slopes of fatigue strength in Figure 33(a), the multi-phase $Al_xCoCrFeNi_x$ HEAs indicate comparable fatigue ratios, compared to other conventional alloys, and the metastable HEAs possess higher fatigue ratios.

3. *Microstructural and mechanical properties of lightweight HEAs*

Liaw's group and his colleagues also designed lightweight and low-cost HEAs, such as $Al_xCrFeMnTi_y$ (x = 1.0, 1.5, 2.0, 3.0, and 4.0, y = 0.25 and 1.0) for high-temperature applications.[44,45] Figure 34 shows the XRD patterns of lightweight $Al_xCrFeMnTi_y$ HEAs. The major phases of all the alloys are a BCC phase while the additional two peaks that are centered at relatively-low angles (26 and 30 deg) are indexed as the Fe_2AlTi-type $L2_1$ structure. In case of the $Al_xCrFeMnTi$ (x = 1.5 and 2.0) HEA, the presence of an intermetallic C14 Laves phase was observed, as displayed in Figures 34(e) and (f). When the alloys contained a large amount of the Al content ($Al_{3.0}CrFeMnTi_{0.25}$ and $Al_{4.0}CrFeMnTi_{0.25}$), some complex structures could be observed in the XRD patterns, which were identified as Al_8Cr_5-type (cI52, I-43m) and $Al_{58.5}Cr_{10.3}Fe_{31.2}$-type (hR26, R3m) phases. Based on the phase identifications, the surface microstructures of these investigated lightweight HEAs were characterized by SEM, as shown in Figures 34(a′) through (f′). The simple solid-solution microstructures were observed for $Al_{1.0}CrFeMnTi_{0.25}$ and $Al_{2.0}CrFeMnTi_{0.25}$ HEAs, while $Al_{3.0}CrFeMnTi_{0.25}$, $Al_{1.5}CrFeMnTi$, and $Al_{2.0}CrFeMnTi$ HEAs exhibit multi-phase structures, which are consistent with XRD results. The black dots appearing on the SEM images are defects produced during the casting process.

In addition to these preliminary investigations on lightweight HEAs, Liaw's group and his colleagues have also focused on a particular composition, namely the $Al_{1.5}CrFeMnTi$ HEA. Here, they examined the phase and microstructural evolution as a function of the heat-treatment conditions.[45] Figures 35(a) through (e) show the microstructures of the $Al_{1.5}CrFeMnTi$ HEA, which are subjected to systematic annealing at temperatures of 750 °C, 850 °C, 1000 °C, and 1200 °C, respectively. As predicted by CALPHAD simulations that were discussed in the previous section,[45] the formation of multi-phases (BCC-based phase + C14 phase) in all the annealed samples were identified from the EBSD images. It was also found that the volume fraction and morphology of the composed phases significantly changed with an increase in the annealing temperature. Moreover, the embedded C14 phase within the BCC-based phase was observed after annealing at 750 °C and 850 °C. Furthermore, it was found that the BCC-based phase becomes the primary phase, and the volume fraction of the C14 phase was reduced when the annealing temperature reaches 1200 °C (see Figures 35(a) through (e)). The phase identifications for the as-cast and 750 °C and 850 °C-annealed $Al_{1.5}CrFeMnTi$ samples were characterized *via* synchrotron XRD patterns, or which the results are displayed in Figure 35(f). The complex diffraction patterns were seen in all samples, which indicates the presence of multi-phases, as determined by the other microstructural investigations. The major diffraction peaks were identified as a BCC phase whereas the minor diffraction peaks belong to the C14 phase. Furthermore, two unique low-angle diffraction peaks are present in the as-cast and 750 °C-annealed samples, which are identified as a $L2_1$ phase. However, the $L2_1$ peaks immediately disappear when the annealing temperature reached 850 °C, which implies that the $L2_1$ phase in this alloy system is thermodynamically unstable at high

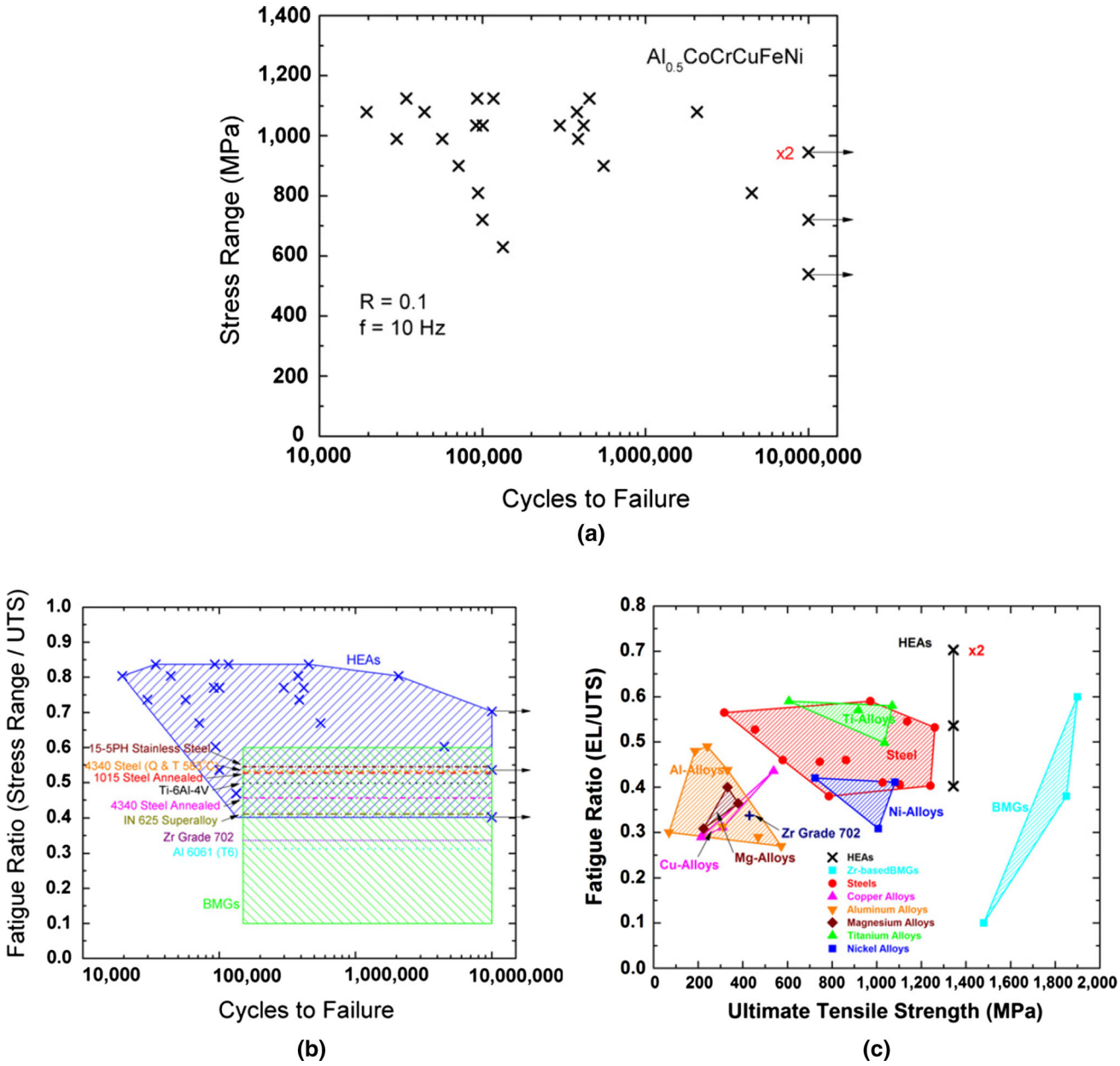

Fig. 32—Four-point bending fatigue results for HEAs, as illustrated by the (*a*) S–N curve for the $Al_{0.5}CoCrFeNi$ HEA plotted as the stress range versus the number of cycles to failure. (*b and c*) Comparison of the fatigue ratio [equal to a fatigue endurance limit (based on the stress range)/UTS] between $Al_{0.5}CoCrFeNi$ HEA and other structural materials (reproduced from Ref. [52] with permission).

temperatures. To further investigate the possible phase transformation at elevated temperatures (*RT*, 800 °C, 1000 °C, 1200 °C, and 1400 °C), the *in situ* neutron experiment was performed, as presented in Figure 35(g). Similar to the synchrotron-diffraction results, the as-cast alloy is composed of BCC, C14, and $L2_1$ phases. However, the absence of diffraction peaks is found for the $L2_1$ phase when the temperature exceeded 1000 °C. Moreover, the magnitudes of the diffraction peaks for the C14 phase are significantly reduced at a temperature of 1400 °C, indicating the decrease of the C14 phase at high temperatures. From the results of the microstructural investigations and phase evolution in the as-cast and annealed $Al_{1.5}CrFeMnTi$ HEAs, it was concluded that the size, morphology, coherency, and spatial distribution of the $L2_1$ phase were subsequently changed after annealing at 750 °C and 850 °C. Finally, the $L2_1$ phase has nucleation advantage due to the small interfacial energy between the $L2_1$ and BCC phases.[45]

4. *Microstructural and mechanical properties of refractory HEAs*

As described above, Al-contained HEAs show relatively-low yield strengths, as compared to conventional metallic alloys. Only one composition, an $Al_{0.3}CoCrFeNi$ HEA, consists of a single FCC phase. In case of lightweight HEAs ($Al_{1.5}CrFeMnTi$), the morphology and volume fraction of the composed phases are

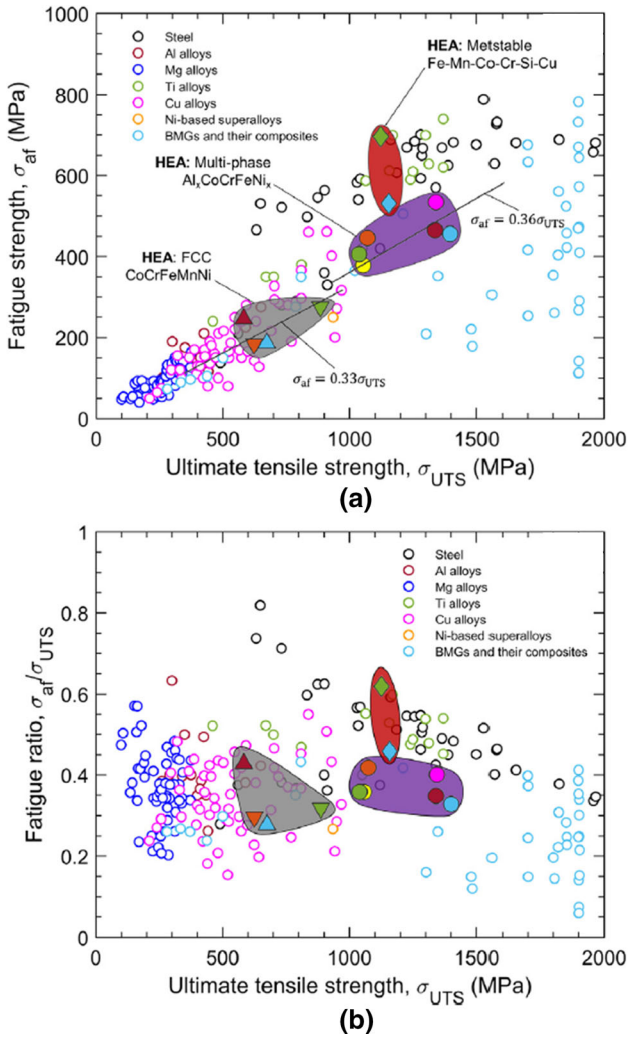

Fig. 33—Fatigue properties of HEAs compared to conventional alloys. (*a*) Fatigue strength (based on the stress amplitude) *vs* ultimate tensile strength. (*b*) Fatigue ratio (based on the stress amplitude) versus ultimate tensile strength (reproduced from Ref. [186] with permission).

dramatically changed at elevated temperatures, indicating low phase stability at high temperatures. Due to these features of microstructural evolution and mechanical properties of the two different types of HEAs, the $Al_{0.3}CoCrFeNi$ and lightweight HEAs are not good candidates for high-temperature applications. To overcome the shortcoming of the designed HEAs, Liaw's group and his colleagues developed the refractory HEAs,[49] which have exhibit excellent phase stability and desirable mechanical properties at elevated temperatures.

Figures 36(a) through (c) show the SEM and EBSD-phase-map images of the as-cast NbTaTiV refractory HEA. The typical dendritic microstructure without any second phases was observed in the as-cast condition, which is consistent with the CALPHAD prediction in the previous section.[49] Furthermore, the dendritic features of the microstructures originate from the chemical inhomogeneity, which is due to the various solidification temperatures of the constituent elements.

Fig. 34—XRD patterns and SEM images of a newly designed lightweight HEA. (*a and a′*) $Al_{1.0}CrFeMnTi_{0.25}$, (*b and b′*) $Al_{2.0}CrFeMnTi_{0.25}$, (*c and c′*) $Al_{3.0}CrFeMnTi_{0.25}$, (*d and d′*) $Al_{4.0}CrFeMnTi_{0.25}$, (*e and e′*) $Al_{1.5}CrFeMnTi$, (*f and f′*) $Al_{2.0}CrFeMnTi$ HEAs (Reprinted from Ref. [44] under the terms of the Creative Commons CC BY 4.0).

The results of the EBSD-phase map (Figure 36(b)) and ND pattern (Figure 36(c)) indicate the presence of a single BCC solid-solution phase. To achieve a homogeneous single phase without the compositional segregation in the as-cast alloy, the NbTaTiV alloy was subjected to a homogenization treatment of 1200 °C for 3 days. The simple microstructure was observed after the homogenization treatment, where no dendritic structure could be observed, as presented in Figure 36(d). Additionally, the ND pattern and EBSD-phase map show that the single BCC phase formed without the obvious formation of a secondary phase or phase transformation that could have occurred after the homogenization treatment (Figures 36(e) and (f)). In short, the chemical segregation in the as-cast state was effectively eliminated by a proper heat-treatment process, and the single-phase solid solution with the homogeneous elemental distribution was successfully produced.

In addition to the microstructural studies, as discussed above, the mechanical properties of these refractory HEAs have also been investigated *via* uniaxial compression tests. Figure 37(a) shows the compressive engineering stress–strain curves for the NbTaTiV refractory HEAs that were tested at *RT*, using a strain rate of 1×10^{-3} s^{-1}. The yield strengths of the as-cast and homogenization-treated alloys were 1236 and 1273 MPa, respectively. The results indicate that no fracture occurred at a compressive strain limit of 30 pct for both alloys, indicating that these HEAs exhibit high yield strengths. Moreover, the findings imply that the chemical inhomogeneity of the NbTaTiV refractory HEA does not significantly influence its mechanical properties. Additional compressive mechanical tests were performed at elevated temperatures, where the results are displayed in Figure 37(b). Here, the yield strength gradually reduced from 1273 to 688 MPa, as the temperature increased from RT to 900 °C. Similar to the *RT* results, the significant strain hardening is retained up to 800 °C whereas a slight reduction of the hardening capability occurred at 900 °C. The strengthening mechanism will be discussed in following section.

Overall, Liaw's group and his colleagues have designed and developed various HEA systems, such as Al-containing ($Al_xCoCrFeNi$), lightweight HEAs ($Al_xCrFeMnTi_x$), and refractory HEAs (NbTaTiV), using thermodynamic predictions (a CALPHAD approach). The phase identification, microstructural characterizations and mechanical properties of designed HEAs have been comprehensively studied, employing various experimental techniques, such as SEM, EBSD, TEM, XRD, synchrotron and ND. The phase formation, yield strength, and plastic strain of newly designed

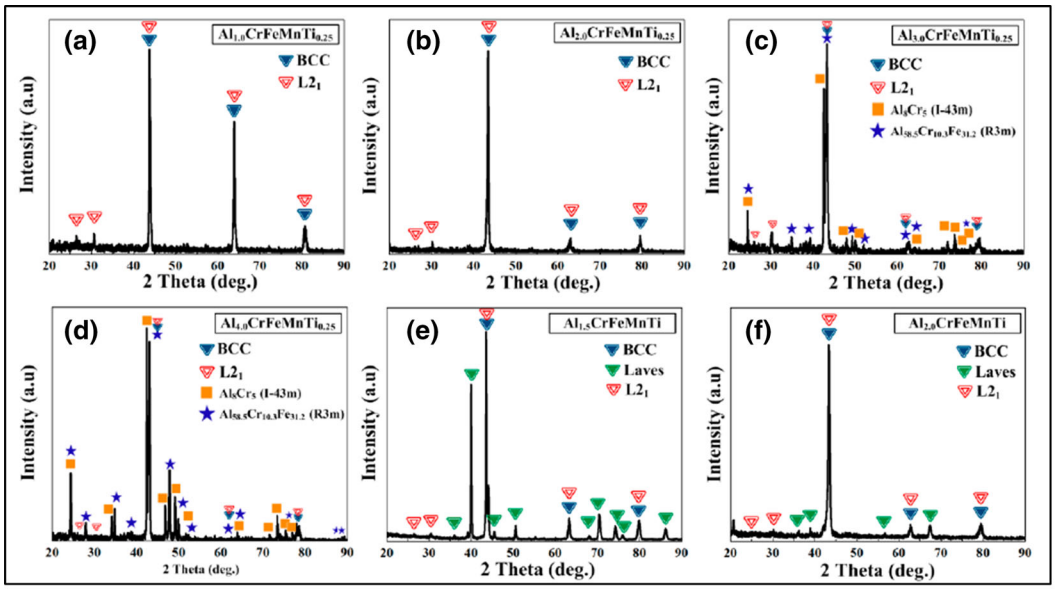
(a)
Al1.0CrFeMnTi0.25
BCC
L21
(b)
Al2.0CrFeMnTi0.25
BCC
L21
(c)
Al3.0CrFeMnTi0.25
BCC
L21
Al5Cr5 (I-43m)
Al58.5Cr10.3Fe31.2 (R3m)
(d)
Al4.0CrFeMnTi0.25
BCC
L21
Al5Cr5 (I-43m)
Al58.5Cr10.3Fe31.2 (R3m)
(e)
Al1.5CrFeMnTi
BCC
Laves
L21
(f)
Al2.0CrFeMnTi
BCC
Laves
L21
Intensity (a.u)
2 Theta (deg.)

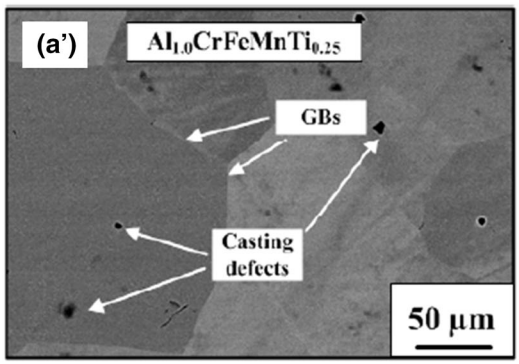
(a')
Al1.0CrFeMnTi0.25
GBs
Casting defects
50 μm

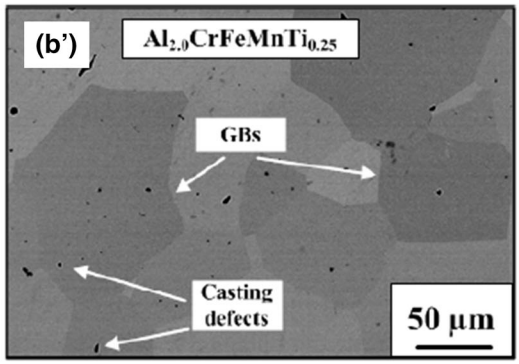
(b')
Al2.0CrFeMnTi0.25
GBs
Casting defects
50 μm

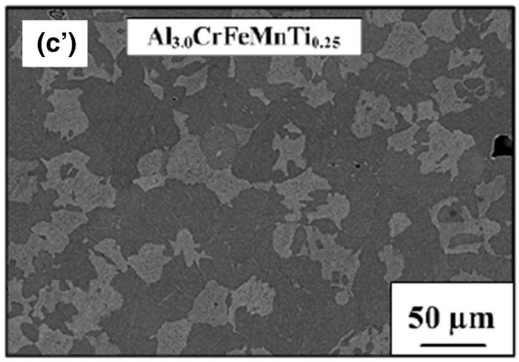
(c')
Al3.0CrFeMnTi0.25
50 μm

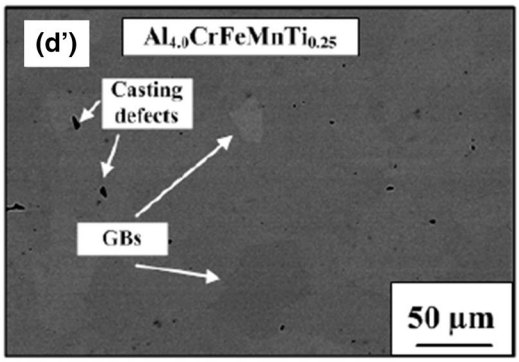
(d')
Al4.0CrFeMnTi0.25
Casting defects
GBs
50 μm

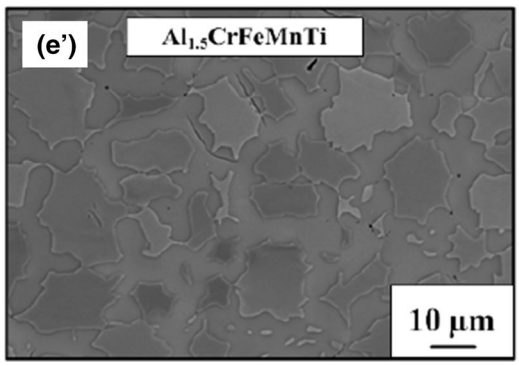
(e')
Al1.5CrFeMnTi
10 μm

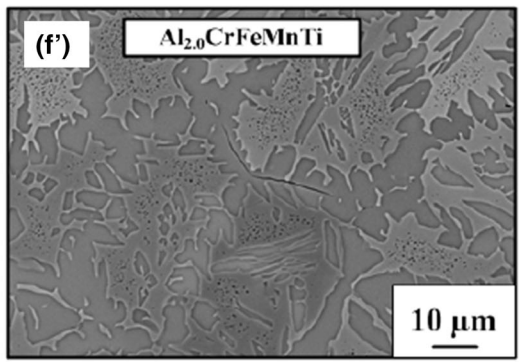
(f')
Al2.0CrFeMnTi
10 μm

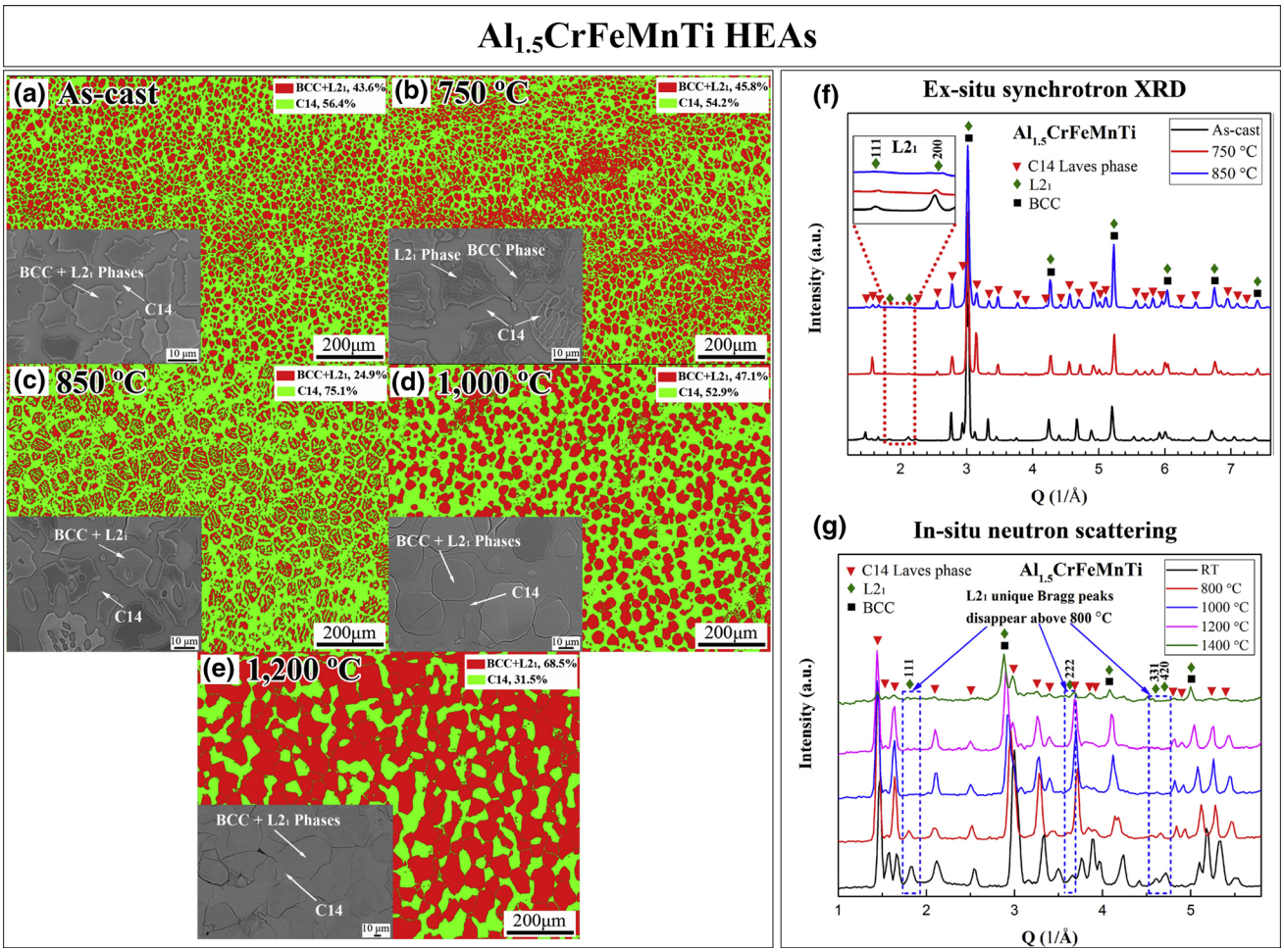

Fig. 35—SEM, EBSD-phase mapping, and diffraction patterns of the $Al_{1.5}CrFeMnTi$ HEAs. (*a*) as-cast state, (*b*) annealed state at 750 °C for 168 h, (*c*) annealed state at 850 °C for 168 h, (*d*) annealed state at 1000 °C for 504 h, and (*e*) annealed state at 1200 °C for 168 h. (*f*) The *ex-situ* synchrotron X-ray diffraction patterns in the as-cast, 750 °C- and 850 °C-annealed states. (*g*) The *in situ* neutron scattering at RT, 800 °C, 1000 °C, 1200 °C, and 1400 °C (reproduced from Ref. [45] with permission).

HEAs in Liaw's group and with his colleagues are summarized in Table I. The detailed and in-depth study of the microstructural evolution and deformation behavior of these designed HEAs *via* state-of-the-art experimental techniques and theoretical calculation will be elaborated upon in the following sections.

5. *Microstructural and mechanical properties of eutectic HEAs*

In addition to microstructural investigation and mechanical behaviors in Al-containing, lightweight, and refractory HEAs, Liaw's group and his colleagues have also architected a dual-phase heterogeneous lamella (DPHL)-structured eutectic high-entropy alloy (EHEA) with the composition of $AlCoCrFeNi_{2.1}$.[187] Figure 38 shows the microstructure of the as-cast EHEA and tailored DPHL HEA. The typical lamellar morphology was observed by EBSD and SEM images (Figures 38(a) and (b)). These lamellae consisted of B2 (NiAl-rich) and FCC (Fe- and Cr-rich) phases (Figure 38(e)), and annealing twins were occasionally observed in FCC grains (Figures 38(d) through (g)). There is also the precipitated-out BCC phase of different sizes in FCC lamellae, as presented in Figures 38(c) through (f). More specifically, they presented two types of NiAl-rich precipitates: the small and scarce P1 (intragranular B2 grains) and the large and primary P2 (intergranular B2 grains) (Figure 38(f)). These results reveal a complex phase decomposition from the initial FCC lamellae, which has now been detected in the EHEA category. Furthermore, as schematically illustrated in Figure 38(h), the presented DPHL-structured $AlCoCrFeNi_{2.1}$ EHEA indicates a two-hierarchical heterogeneity, which consisted of the submicron-grade FCC/B2 grains within the FCC lamellae and the micro-grade alternate FCC/B2 lamellae.

Figure 39(a) exhibits mechanical properties of as-cast, ultra-grained (UFG), complex and hierarchical (CH), and tree DPHL HEAs.[188] An UFG EHEA shows a twice higher yield strength than the as-cast EHEA but comes at loss of ductility. On the other hand, DPHL700 and DPHL740, which have inherited lamellar geometries, reveal a simultaneous strength-ductility enhancement, compared to the as-cast EHEA. The DPHL 660 exhibit a higher yield strength of 1490 MPa, and comparable ductility of 16 pct. The detailed values of

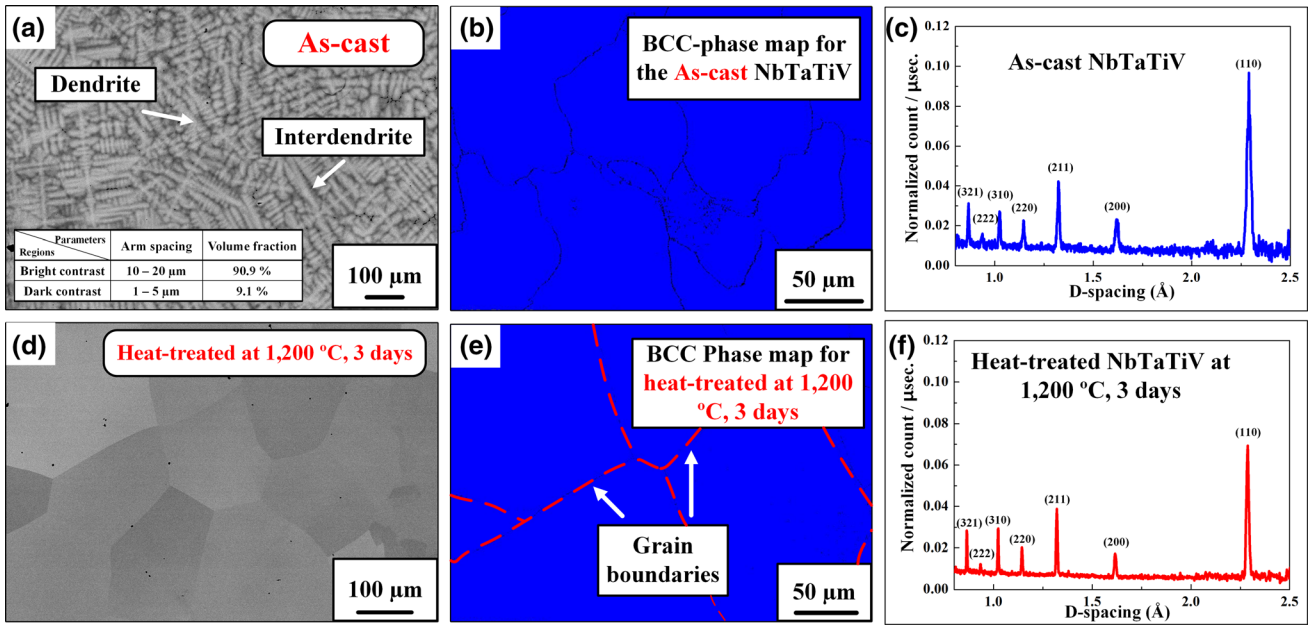

Fig. 36—Phase and microstructural characterization of as-cast and homogenized NbTaTiV refractory HEAs. (*a*) SEM image, (*b*) EBSD-phase mapping, and (*c*) neutron-diffraction pattern of an as-cast NbTaTiV refractory HEA. (*d*) SEM image, (*e*) EBSD-phase mapping, and (*f*) neutron-diffraction pattern of a homogenization-treated NbTaTiV refractory HEA (reproduced from Ref. [49] with permission).

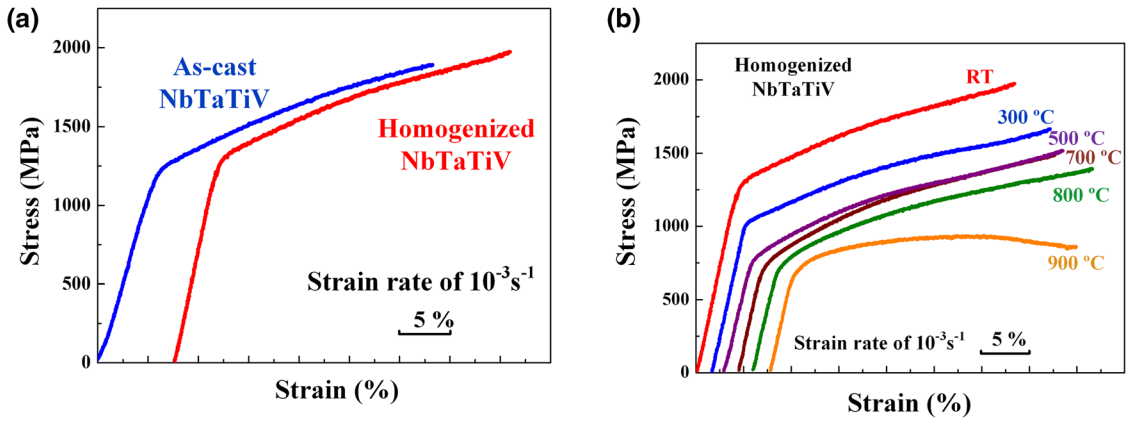

Alloys	Conditions	Yield strength, σ_y (MPa)	Plastic strain, ε_p (%)
NbTaTiV	As-cast	1,236	> 30
	Homogenized	1,273	> 30

Condition	RT	300 °C	500 °C	700 °C	800 °C	900 °C
σ_y (MPa)	1,273	1,034	778	723	720	688

Fig. 37—(*a*) Engineering compressive stress-strain curves of the as-cast and homogenization-treated NbTaTiV refractory HEA at RT. (*b*) Mechanical properties of NbTaTiV refractory HEA at elevated temperatures (reproduced from Ref. [49] with permission).

mechanical properties of the present HEAs are summarized in Table I. The significant enhancement of mechanical properties for the hierarchical DPHL HEAs could be reasonably explained by deformation processes. During tensile deformation, the soft FCC lamellar matrix is more susceptible to starting plastic deformation after the soft FCC and hard B2 phase co-deformed elastically. The existence of plastic-strain gradients in the soft lamellar matrix near lamella interfaces.[189,190] Consequently, this process produces a long-range back stress, which causes the difficulty of dislocation movement in FCC grains until B2 grains start to yield deformation.[191] Ultimately, under such two-hierarchical constraints, the FCC grains appear much stronger than when they are not constrained, producing so-called synergetic strengthening and elevating the yield strength of materials.[192] The good ductility for the complex and hierarchical EHEA mainly originated from the strong back-stress hardening effect. Such a hierarchical architecture can provide substantial domain boundaries separating areas of diverse hardness, consequently being particularly favorable to benefiting from back-stress hardening. In the hierarchical structure, there are coarse non-lamellar regions, which

consist of the soft FCC matrix and hard B2 phases. Although these regions allow significant strain partitioning to induce back-stress strengthening, the soft FCC phase also facilitate the material to yield at low stresses due to the absence of the lamellar constraint effects.[192] Figures 39(b) and (c) display a comparison of mechanical properties of the hierarchical DPHL HEAs with various traditional alloys and other reported HEAs. The tensile strengths and elongations of reported HEAs, including current DPHL HEAs, are separated from the general trend for traditional metallic materials, indicating a favorable tensile strength-ductility combination (Figure 39(b)). In contrast, the yield strength-elongation map in Figure 39(c) suggests that only current DPHL HEAs stand out from the mechanical trend. This trend reveals a common phenomenon/problem, from which it is currently possible to achieve great tensile strength-ductility balance in HEAs. Through the comprehensive work from Prof. Liaw's group and his colleagues, it provides a pathway for strengthening eutectic alloys and widens the design toolbox for high-performance materials based upon EHEAs.

C. *Serrated Flow-Behavior of HEAs*

Similar to BMGs, Liaw's group and his colleagues have performed a multitude of studies on the plastic serrated flow phenomenon in HEAs.[96,109,130–134,136,193] Figure 40 presents a schematic of the pinning–unpinning cycle, which features 4 stages of a serration.[96,130] During stage I, dislocations are caught and pinned by diffusing solute atoms. During stage II, the dislocation remains pinned while the stress increases until a critical stress is reached. In stage III, the critical stress is reached, and the dislocation is able to break free, resulting in a stress drop in the stress *vs* strain curve. Stage IV represents the repinning of the dislocation by solute atoms.

Other studies have analyzed the serration dynamics using different analytical techniques (see Section II–C–1).[109,131,134] For example, the RCMSE technique was used to analyze the serrated flow in an $Al_{0.5}CoCrCuFeNi$ HEA.[109] Here, samples were subjected to compression testing at strain rates ranging from 5×10^{-5} to 2×10^{-3} s^{-1} and temperatures of 400 °C to 600 °C. Figure 41 displays the stress–strain curves for the samples tested in the above conditions. As can be seen, serrations could be observed in all the conditions. Type-C serrations were observed in the samples tested at 600 °C, while Type-A or B serrations occurred in the samples tested at 400 °C and 500 °C. In terms of their microstructures, synchrotron XRD revealed that the samples tested below 600 °C consisted of only an FCC structure, while a combination of FCC and B2 structures was seen in the sample tested at 600 °C.

Figure 42 displays the results of the RCMSE analysis for the samples tested at 5×10^{-5} to 2×10^{-3} s^{-1} and temperatures of 400 °C to 600 °C. From the results, a few observations can be made. Firstly, the sample-entropy curves exhibited generally increasing trends (beyond a certain scale factor), which indicates that the serrated flow exhibited complex dynamical behavior in all the experimental conditions. Secondly, the sample-entropy curves were the greatest at 500 °C and lowest at 600 °C, for each strain rate. Third, the samples-entropy curves increased with respect to the strain rate, for all temperatures.

The above findings suggest the following matters. The relatively-lower complexity for the samples tested at 600 °C corresponded to Type-C serrations. These types of serrations are characterized by a two-step process that consists of the rapid pinning and unpinning of dislocations by solute atoms, which is characteristic of simple behavior. As for the serrations that occurred in the sample tested at 500 °C, the serrations were characterized by a three-step process that is likely attributed to more complex dynamics underlying the serrated flow, such as the solute atom-dislocation line, dislocation line-dislocation line, dislocation line-precipitate interactions, and solute atom–solute atom interactions.[109] Finally, the increase in the complexity of the serrated flow with the strain rate, as indicated by the increase in the sample-entropy curves, may be attributed to the following matters. The increase in the complexity from the lowest to highest strain rates may be caused by the decrease in the plastic relaxation time between successive drops. However, once the reloading time exceeds that of the relaxation time, new bands can form in the field of the unrelaxed internal stresses, leading to a hierarchy of length scales that corresponds to more complex dynamical behavior.[117]

D. *In-depth Study of Microstructural Evolution and Deformation Behaviors of Various HEAs Via State-of-the-art Facilities*

To gain a more comprehensive understanding of the microstructural evolution and mechanical behaviors of designed HEAs, such as the atomic-scale elemental distributions, dynamic structural evolution, and mechanical behavior, Liaw's group and his colleagues have conducted further experimental efforts through the use of TEM, atom probe tomography (APT), *in situ* TEM, and *in situ* neutron studies.

1. *In situ TEM studies for Al-containing HEAs*

Figure 43 illustrates the bright-field (BF) images of the $Al_{0.3}CoCrFeNi$ HEA, which were obtained by *in-situ* TEM, during heating from *RT* to 900 °C (Figures 43(a) through (e)), as well as during cooling down to RT (Figure 43(f)).[48] Importantly, these *in situ* TEM results provide information about the dynamic structural evolution of the designed Al-contained HEAs at elevated temperatures. Being consistent with CALPHAD simulations,[48] SEM and neutron-diffraction results in the previous section, the secondary phases are presented when the temperature increased up to 500 °C (Figures 43(b) and (c)). Above 500 °C, the proportion of secondary phases increases with an increase in temperature up to 900 °C (Figures 43(d) and (e)). However, the

Table I. The Phases, Yield Strengths, and Plastic Strains of Newly-Designed HEAs[44,45,48,49,55,187]

Alloys		Phases	Yield Strength (MPa)	Plastic Strain (Pct)
Al-contained HEAs	$Al_{0.3}CoCrFeNi$	single FCC	210	97
	$Al_{0.5}CoCrFeNi$	FCC + B2	550	56
	$Al_{0.7}CoCrFeNi$	FCC + B2 + BCC	600	8
Lightweight HEAs	$Al_{1.0}CrFeMnTi_{0.25}$	BCC + $L2_1$	—	brittle
	$Al_{2.0}CrFeMnTi_{0.25}$	BCC + $L2_1$	—	brittle
	$Al_{3.0}CrFeMnTi_{0.25}$	BCC + $L2_1$ + I-43m + R3m	—	brittle
	$Al_{4.0}CrFeMnTi_{0.25}$	BCC + $L2_1$ + I-43m + R3m	—	brittle
	$Al_{1.5}CrFeMnTi$	BCC + Laves (C14) + $L2_1$	—	brittle
	$Al_{2.0}CrFeMnTi$	BCC + Laves (C14) + $L2_1$	—	brittle
Refractory HEAs	as-cast NbTaTiV	single BCC	1236	> 30
	homogenized NbTaTiV	single BCC	1273	> 30
Dual-Phase Heterogeneous Lamella HEAs	DPHL740	FCC + B2	1154	25
	DPHL700	FCC + B2	1263	21
	DPHL660	FCC + B2	1490	16

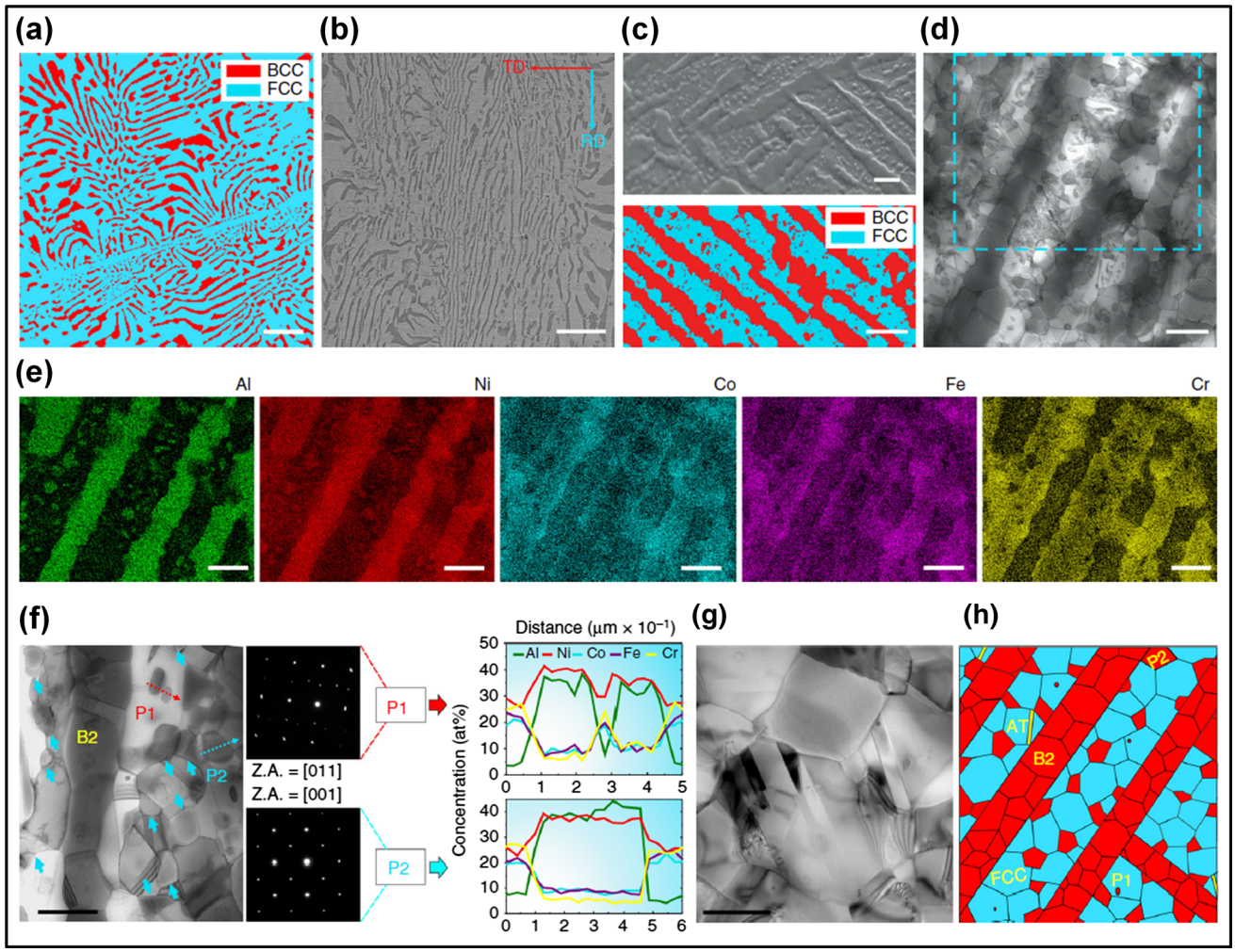

Fig. 38—Microstructures of the as-cast EHEA and the hierarchical DPHL700. (*a*) EBSD phase image of the as-cast EHEA. (*b* and *c*) Scanning-electron-microscope (SEM) image and EBSD-phase image of the DPHL HEA. (*d*) Scanning TEM (STEM) image exhibiting a more detailed DPHL structure. (*e*) EDS maps of the identical region marked in *d* showing the distribution of Al, Ni, Co, Fe, and Cr. (*f*) Enlarged STEM image and the corresponding selected-area diffraction patterns (SADPs) and EDS composition profiles. (*g*) TEM image showing annealing twins. (*h*) Microstructural schematic sketch of the DPHL structure.[187]

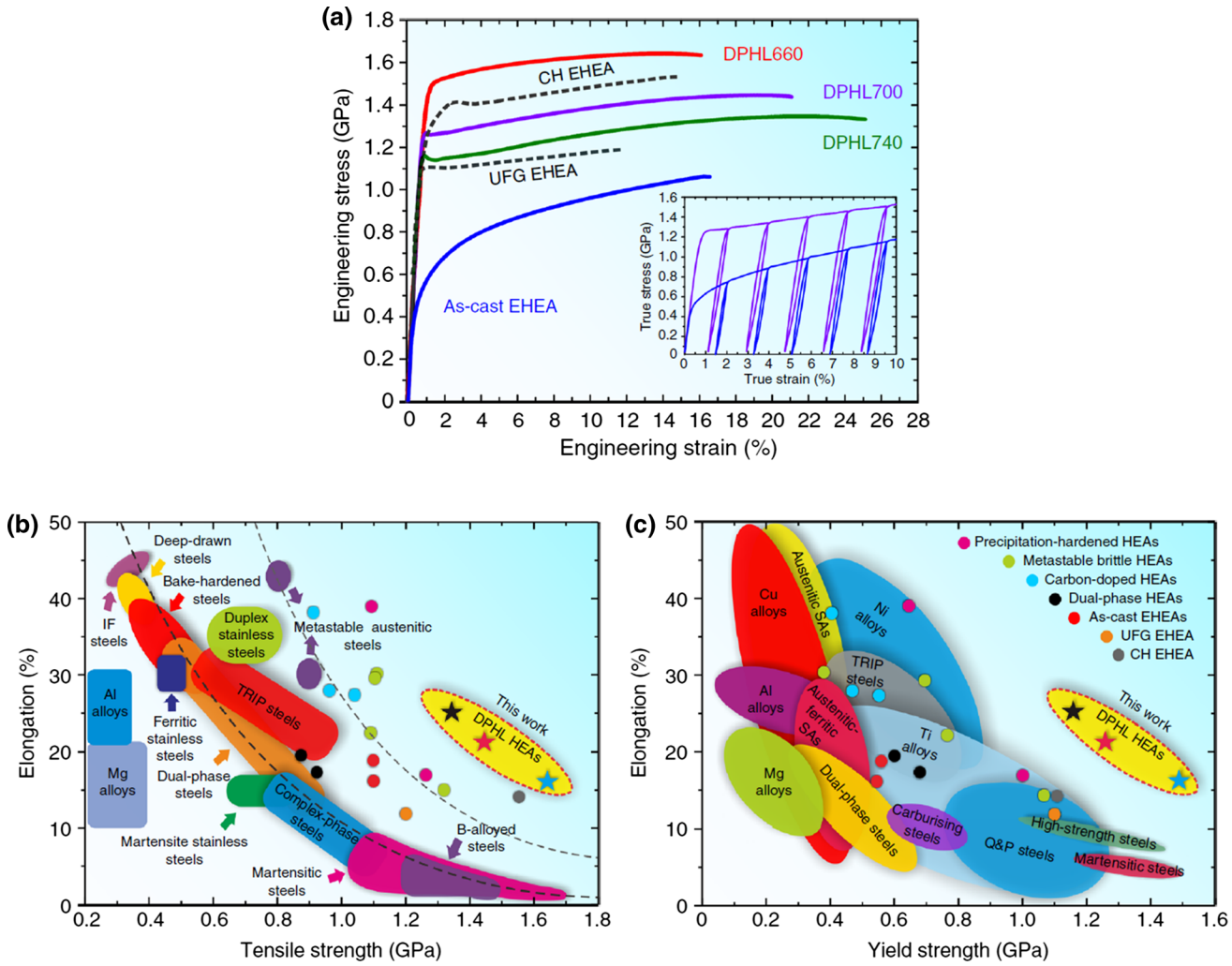

Fig. 39—(*a*) Mechanical properties of as-cast EHEA, UFG EHEA, CH EHEA, and three DPHL HEAs. (*b* and *c*) Tensile properties and yield strengths of the hierarchical DPHL HEAs in comparison with the traditional metallic materials and the previously-reported hardened HEAs.[187]

quantity of the secondary phases decreases as the temperature decreases from 900 °C to *RT*, as shown in Figure 43(f). Figures 43(g) through (l) present the BF-TEM images for the $Al_xCoCrFeNi$ HEAs (x = 0.3, 0.5 and 0.7) at RT and after heating at 500 °C for 10 minutes, respectively. The dislocations in the FCC solid-solution phase were observed at RT for the $Al_{0.3}CoCrFeNi$ HEA. Furthermore, all the HEAs ($Al_{0.3}$, $Al_{0.5}$, and $Al_{0.7}$) indicate the precipitation of secondary phases from the FCC solid-solution phase after heating at 500 °C for 10 minutes.

Interestingly, the apparent structural-evolution in the $Al_{0.7}CoCrFeNi$ HEA was observed before and after annealing at 900 °C for 10 minutes, as presented in Figures 43(m) through (r). The nano-sized BCC phase is homogenously-distributed in the FCC matrix without the presence of precipitation before annealing. The BCC and FCC phases have a perfect crystallographic-orientation relationship, namely $(110)_{BCC}//(200)_{FCC}$, $[001]_{BCC}//[001]_{FCC}$, as illustrated in the electron-diffraction-pattern that is presented in Figure 43(n). On the other hand, the formation of many precipitates in the FCC matrix was clearly observed after annealing at 900 °C for 10 minutes and then cooling down to *RT*. There are two types of precipitates, *i.e.*, equiaxial (Cr-rich σ phases) and rod-like (Al-rich θ phases) phases, which are identified by the electron-diffraction-patterns that are presented in Figures 43(p) and (q). The Cr-rich σ phases belong to a tetragonal system with a space group of $P4_2/mnm$ (136), and the Al-rich θ phases belong to a monoclinic system with a space group of C2/m (12). The electron diffraction pattern for the $Al_{0.7}CoCrFeNi$ HEA after annealing 900 °C for 10 minutes. Figure 43(r) indicates that the isolated precipitate is an FCC phase. Some satellite spots are distinguished from the main spots due to the presence of smaller-sized precipitates around it. This feature proves that the residual matrix can form the Ni-rich solid-solution. In short, these in-depth structural investigations *via in-situ* TEM provide a greater fundamental understanding of the phase stability and evolution of both the single-phase ($Al_{0.3}CoCrFeNi$) and dual-phase ($Al_{0.5}CoCrFeNi$ and $Al_{0.7}CoCrFeNi$) HEAs.

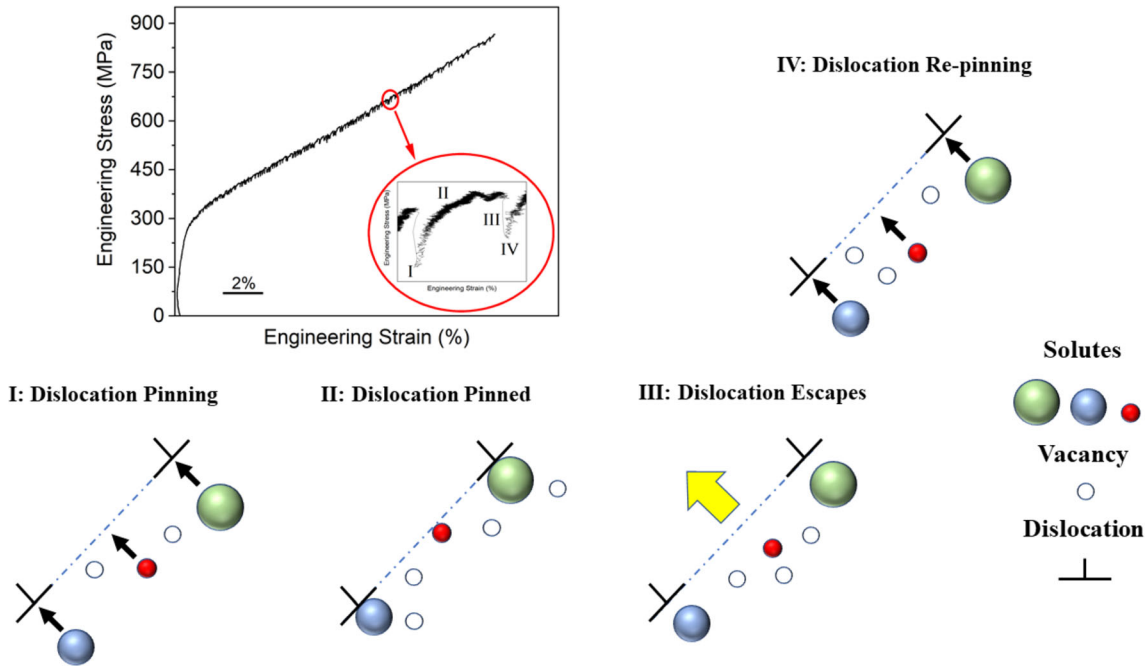

Fig. 40—A schematic of the serration process that results from the pinning and unpinning of dislocations by solute atoms. Each numbered section corresponds to the different interactions between the solutes and dislocations during the serration event as follows: (I) the solute atoms pin a moving dislocation, which corresponds to the onset of the serration; (II) the dislocation remains pinned as the stress increases; (III) after an enough stress builds up, the dislocation escapes; and (IV) the solute atoms catch and re-pin the dislocation (Reprinted from Ref. [96] under the terms of the Creative Commons CC BY 4.0).

2. *TEM and APT analyses for lightweight HEA*

Based on the phase identification and microstructural evolution results for the lightweight HEAs ($Al_{1.5}CrFeMnTi$),[45] which behave as a function of the heat-treatment condition (described in the previous section), the crystal structures of the constituent phases were further identified by TEM characterization, as shown in Figure 44.[45] Figure 44(a) exhibits the dark-field, selected area electron diffraction (SAED), and high-resolution TEM images of the as-cast $Al_{1.5}CrFeMnTi$ HEA. The dark-field image of $L2_1$ particles was taken, using the (101)-type superlattice reflection along the $\langle 001 \rangle_{L21+BCC}$ zone axis. The presence of highly-ordered spatially-distributed $L2_1$ particles in the BCC matrix with a size of ~ 30 nm can be observed. The morphology of BCC/$L2_1$ phases in the as-cast condition is similar to typical γ/γ' phases found in Ni-based superalloys. The significant increasing and coarsening of the $L2_1$ particles were observed after annealing at 750 °C (Figure 44(b)), which are consistent with the SEM results in Figure 34(e′). The misfit dislocations were present along the interface between the $L2_1$ precipitates and the BCC matrix, implying a large lattice misfit. After annealing at 850 °C for 168 hours, the size of the $L2_1$ particles significantly decreased (~ 4 nm), and the superlattice reflection spots unique to the $L2_1$ phase were must less noticeable, as indicated in Figure 44(c). The inverse fast Fourier transform (IFFT) image (Figure 44(c)) shows the short-range order in the $L2_1$ phase, indicating the nucleation stage of the $L2_1$ phase. With the nano-scaled structural investigation performed via TEM, the detailed chemical composition of the $L2_1$ and BCC phases present in the matrix of the as-cast, 750 °C and 850 °C-annealed samples were measured by the APT, as shown in Figures 44(d) through (f). In the as-cast condition, small Cr-rich particles can be observed in the large FeTi-rich $L2_1$ precipitates. From the proximity histogram, Cr migrates from the $L2_1$ precipitates to the Cr-rich particles, whereas Fe and Ti diffuse from the Cr-rich particles to the $L2_1$ precipitates. Figure 44(e) exhibits the elemental distributions of the constituent elements in the BCC and $L2_1$ phases for the 750 °C-annealed samples. Due to the long annealing process, the nano-scaled chemical inhomogeneity of Cr, Fe, Mn, and Ti was observed in both the BCC and $L2_1$ phases. The detailed decomposition amplitude in both phases are determined by the peak-to-trough Cr composition, as shown in Figure 44(e). For the 850 °C-annealed samples, the nano-scaled Cr-depleted $L2_1$ particles are observed in the BCC matrix, as displayed in Figure 44(f). A similar feature was observed for the chemical distribution of the as-cast and 750 °C-annealed samples (Fe and Ti are enriched in $L2_1$ precipitates, and Cr is enriched in BCC phases). The detailed composition of the BCC and $L2_1$ phases were determined from the proximity histogram, as presented in the graph from Figure 44(f). Therefore, these systematic TEM and APT experiments provided a much greater understanding of the structural evolution and elemental distribution of lightweight HEAs. Furthermore, it is anticipated that the results of these investigations will provide a road map to develop future novel lightweight HEAs.

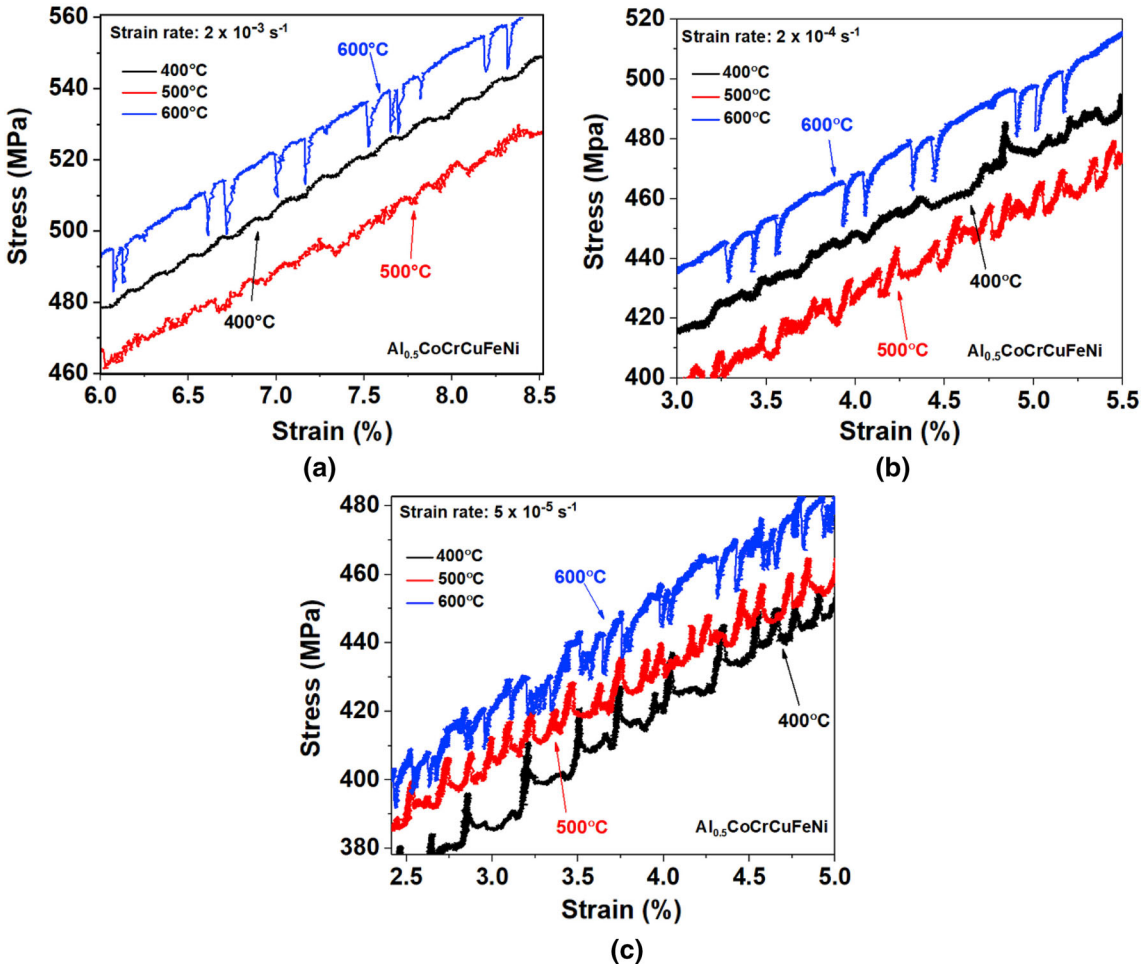

Fig. 41—Stress *vs* strain graph for the $Al_{0.5}CoCrCuFeNi$ HEA samples tested at strain rates of (*a*) 2×10^{-3} s^{-1}, (*b*) 2×10^{-4} s^{-1}, and (*c*) 5×10^{-5} s^{-1} for temperatures of 400 °C to 600 °C (reproduced from Ref. [109] with permission).

3. *Neutron diffraction studies*

In addition to the dynamic phase and structural investigations of $Al_xCoCrFeNi$ and $Al_{1.5}CrFeMnTi$ HEAs, which involved various state-of-the-art microscopy techniques (*in-situ* TEM and APT), Liaw's group and his colleagues have also examined the phase formation and transformation in $Al_{1.3}CoCrCuNi$ HEA (RT to elevated temperatures) via ND with aerodynamic levitation.[47] Figure 45(a) shows the schematic for the levitation ND experiment. The $Al_{1.3}CoCrCuNi$ HEA specimen was simultaneously levitated *via* flowing gas and heated up to its melting temperature (~ 1400 °C) using a laser beam. It is important to note that this levitation method allows one to examine the intrinsic phase transformation of the alloy since it eliminates any possibility that the sample will undergo any phase transformations due to contact with the container. As for the experiment, the ND patterns can be obtained at different temperatures by changing the heating laser power. Figure 45(b) presents the ND patterns from the levitation study of the $Al_{1.3}CoCrCuFeNi$ HEA. The presence of multi-phases (FCC + BCC + B2 phases) in the HEA was identified from the ND pattern at *RT*. Typically, the phase transformation from the FCC (triangle symbols) to BCC/B2 (square symbols) phases is clearly observed as the temperature increases from 20 °C to 1400 °C. Furthermore, the B2 superstructure reflection persists from *RT* to 1150 °C. However, as can be seen in Figure 45(c), the intensity of the B2-related diffraction peaks disappear once the temperature exceeded 1150 °C, in which the primary phase is the disordered BCC solid-solution. Based on the results of this experimental effort, Liaw's group and his colleagues suggested that the levitated ND experiments are an appropriate technique to investigate the real-time phase transformation in various designed HEAs.[47]

As described above, Liaw's group and his colleagues have focused on the phase and microstructural investigation of HEAs, using various state-of-the-art techniques such as *in-situ* ND experiments.[46] With the comprehensive deformation behavior and microstructural information on these HEAs that were gained from these experiments, they have established the strong link between phases/microstructures and mechanical behaviors. Figure 46 shows the schematic for the setup of the ND during tension deformation. The neutron beam impinges on the sample at a 45 deg angle of incidence, relative to the loading direction. The diffracted neutron

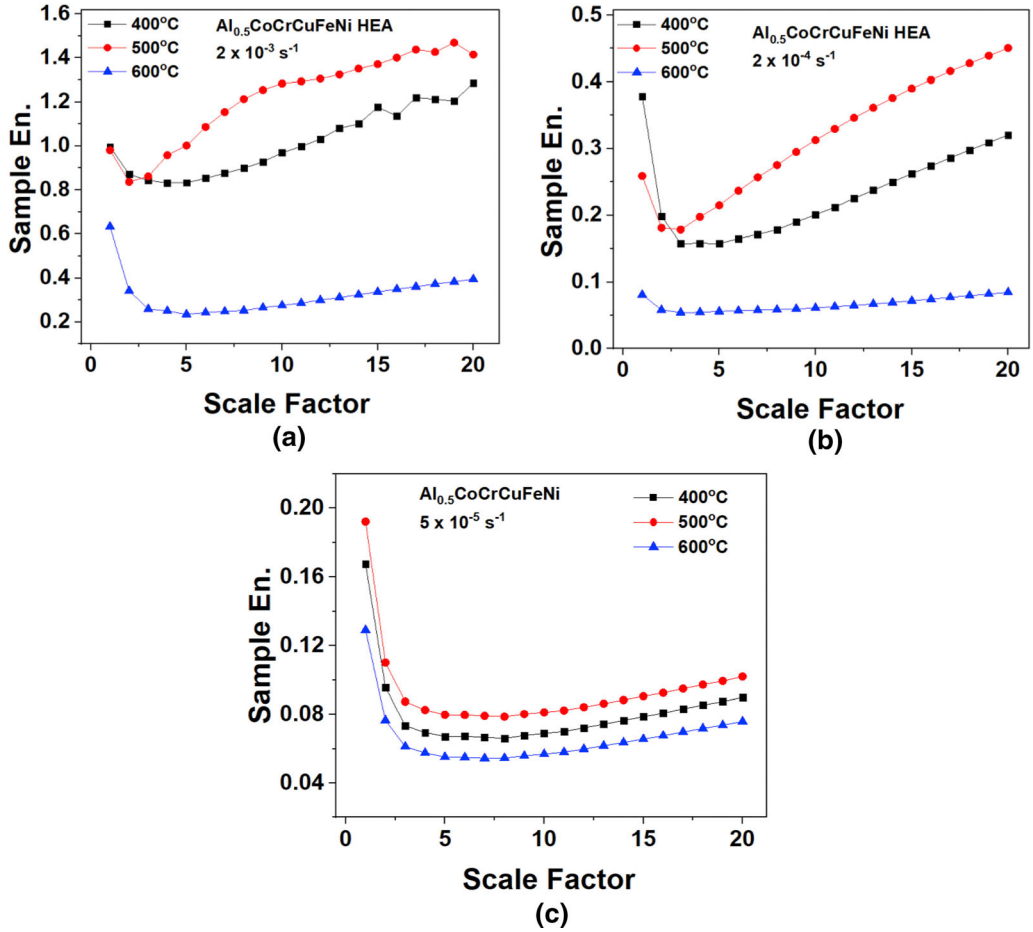

Fig. 42—The results of the RCMSE analysis (sample entropy *vs* scale factor) for the $Al_{0.5}CoCrCuFeNi$ HEA samples tested at strain rates of (*a*) 2×10^{-3} s^{-1}, (*b*) 2×10^{-4} s^{-1}, and (*c*) 5×10^{-5} s^{-1} and temperatures of 400 °C to 600 °C, where the sample entropy was plotted for scale factors ranging from 1 to 20 (reproduced from Ref. [109] with permission).

beams are collected by two sets of detectors that are positioned perpendicular to the path of the incident beam.

The neutron is a unique probe for investigating the structures of various materials due to its high penetration depth. Furthermore, the ND can be used for conducting a precise characterization of the atomic structures of various HEAs, such as crystallographic textures and lattice constants of composed phases. Moreover, this technique allows for the measurement of bulk components as well as the detection of light-weight elements, such as hydrogen, carbon, and lithium, which cannot be observed from the XRD methods. Importantly, when the samples are subjected to continuous mechanical tests, the *in-situ* neutron experiments can provide three critical pieces of information about bulk HEAs. These pieces of information include the evolution of (I) d-spacing, (II) diffraction peak intensity, and (III) diffraction peak width, during elastic and plastic deformation. Additionally, the evolution of diffraction peak positions (d-spacing) can provide the lattice strains of the average phases and crystallographic orientations. The evolution of the lattice strains as a function of the applied stress (during elastic deformation) can help elucidate the elastic deformation behavior of HEAs. In addition, the lattice strain evolution is a measure of the elastic modulus for the composed phases and each grain orientations. The excellent merits of ND, as discussed above, led Liaw's group and his colleagues to use this method to investigate the deformation behavior of an $Al_{0.3}CoCrFeNi$ HEA. The results of their experiments found that single FCC solid-solution phase remained in the matrix after the homogenization treatment and multi-phase formation and after long-time heat-treatment at 700 °C for 500 hours.

The *in situ* ND, where the sample was subjected to continuous tension, has been used to examine the lattice-strain changes as a function of stress in $Al_{0.3}CoCrFeNi$ HEA after the homogenization treatment of 1250 °C for 2 hours. Here, the macroscopic stress–strain behavior during *in situ* tension at RT was measured (Figure 47(a)). In the elastic region, the machine is operating in the stress-control mode, *i.e.*, the tension tests are interrupted, and the stress level is held for 10 minutes at values of 20, 40, 60, 80, 100, 120, and 140 MPa. Subsequently, the experiment is performed in the strain-control mode. The macroscopic stress-strain curve is shown in Figure 47(a). As can be seen, the yield strength is around 145 MPa. The neutron-scattering geometry allows for the simultaneous

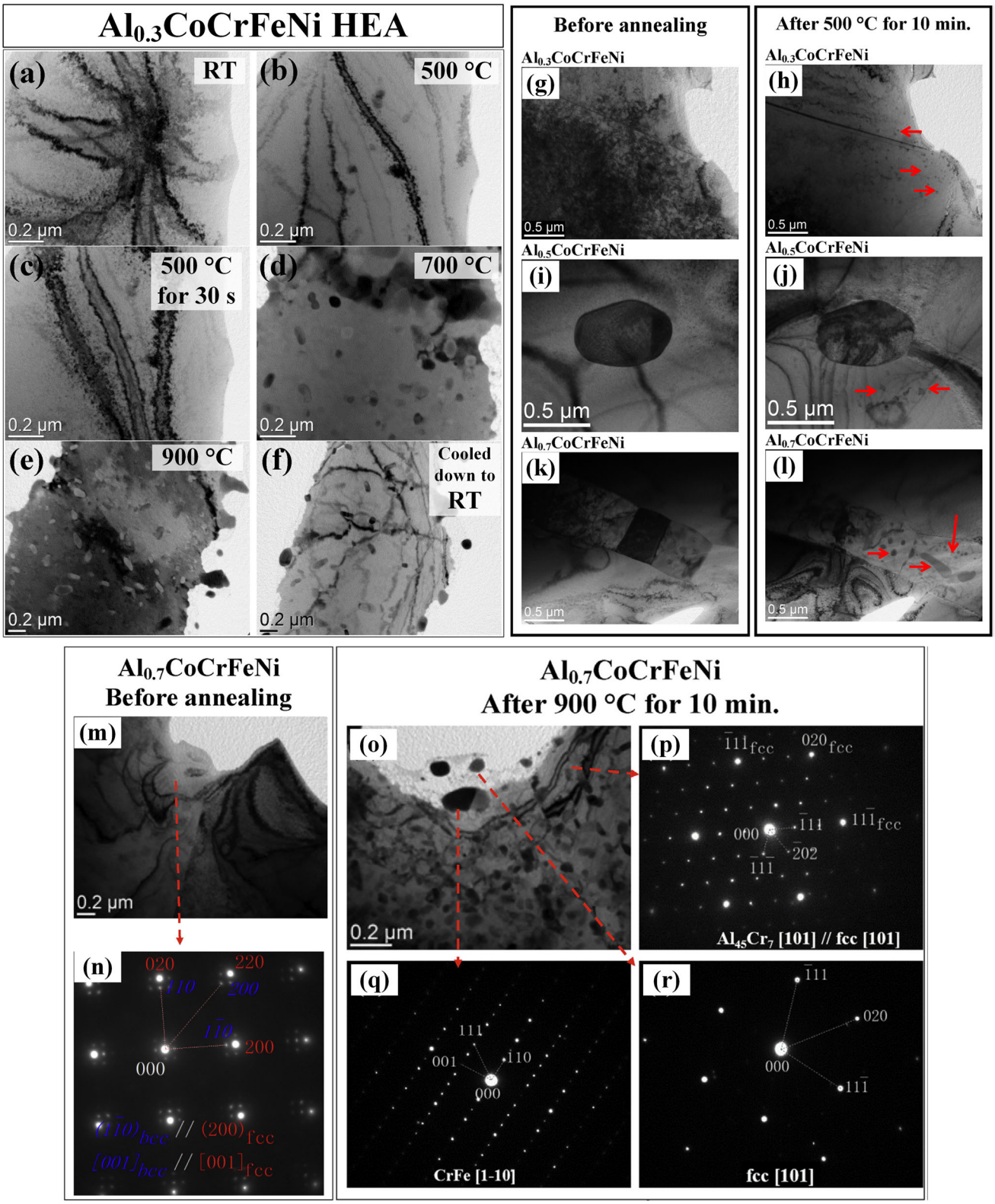

Fig. 43—TEM images of $Al_xCoCrFeNi$ HEAs during *in-situ* TEM heating. $Al_{0.3}CoCrFeNi$ at (*a*) RT, (*b*) reaching 500 °C, (*c*) 500 °C for 30 s, (*d*) reaching 700 °C, (*e*) reaching 900 °C, and (*f*) cooled down back to RT. The snapshots of $Al_xCoCrFeNi$ HEAs before and after heating at 500 °C for 10 mins. (*g and h*) $Al_{0.3}CoCrFeNi$, (*i and j*) $Al_{0.5}CoCrFeNi$, and (*k and l*) $Al_{0.7}CoCrFeNi$ HEAs. (*m*) A BF image and (*n*) energy-diffraction-pattern (EDP) of the $Al_{0.7}CoCrFeNi$ HEA before heating. The BF image (*o*) and EDPs (*p–r*) of the $Al_{0.7}CoCrFeNi$ HEA after heating at 900 °C for 10 mins. (reproduced from Ref. [48] with permission).

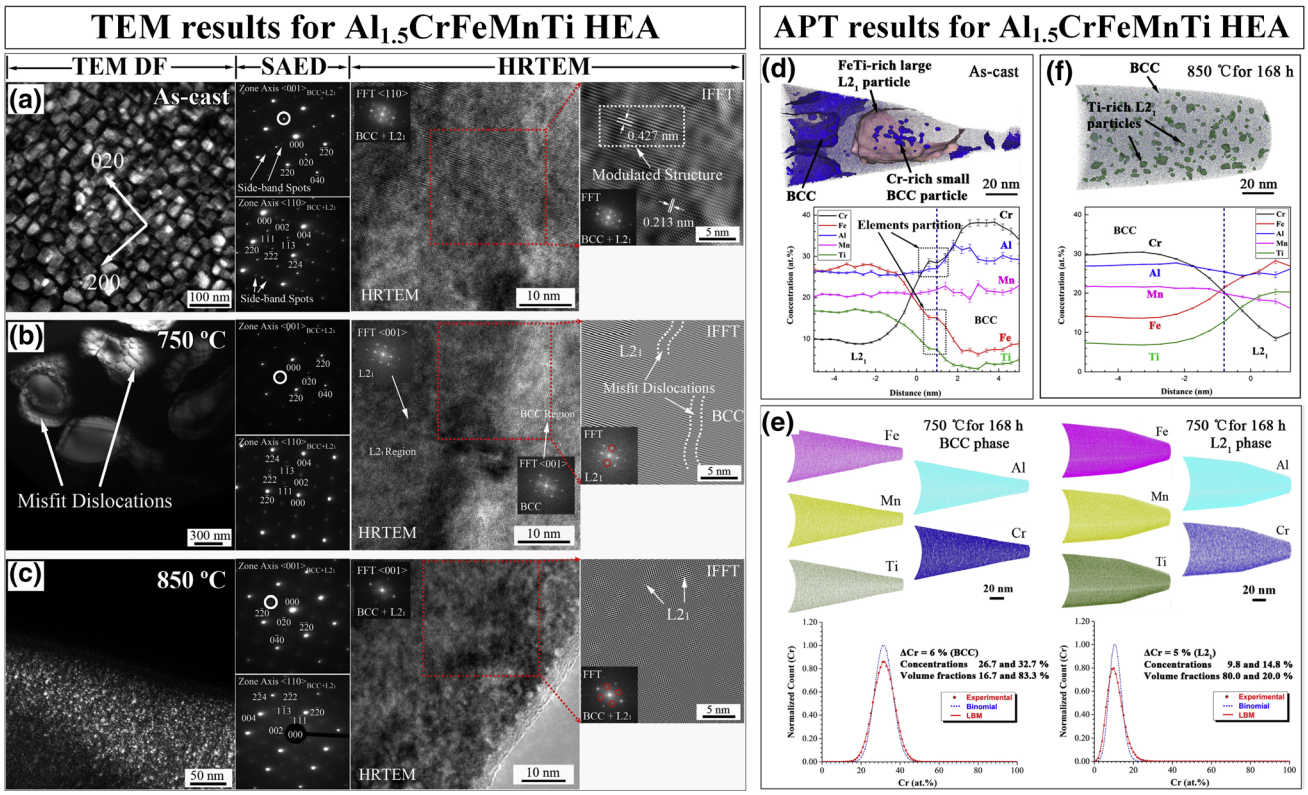

Fig. 44—TEM images of $Al_xCoCrFeNi$ HEAs during *in-situ* TEM heating. $Al_{0.3}CoCrFeNi$ at (*a*) RT, (*b*) reaching 500 °C, (*c*) 500 °C for 30 s, (*d*) reaching 700 °C, (*e*) reaching 900 °C, and the (*f*) cooled to RT. The snapshots of the $Al_xCoCrFeNi$ HEAs before and after heating at 500 °C for 10 mins. (*g and h*) $Al_{0.3}CoCrFeNi$, (*i and j*) $Al_{0.5}CoCrFeNi$, and (*k and l*) $Al_{0.7}CoCrFeNi$ HEAs. (*m*) A BF image and (*n*) energy-diffraction-pattern (EDP) of the $Al_{0.7}CoCrFeNi$ HEA before heating. The BF image (*o*) and EDPs (*p-r*) of the $Al_{0.7}CoCrFeNi$ HEA after heating at 900 °C for 10 mins (reproduced from Ref. [45] with permission).

measurement of two scattering vectors, as shown in Figure 46. Figures 47(b) and (c) show the typical diffraction patterns (RT, 10-minute data collection) of the $Al_{0.3}CoCrFeNi$ HEA after the homogenization treatment of 1250 °C for 2 hours. All peaks are indexed to an FCC structure, as presented in Figures 47(b) and (c). The intensity difference between Figures 47(b) and (c) indicate that the material has a strong texture. The lattice-strain evolution of the (200), (220), (311), and (331) planes within the homogenized (1250 °C, 2 hours) $Al_{0.3}CoCrFeNi$ HEA during tensile deformation at *RT* is displayed in Figure 47(d). The results signify that the lattice-strain change is strongly dependent on the grain orientations, indicative of the strong elastic anisotropy. The {200} grains present the largest elastic strain along the loading direction and a significant shift, relative to their linear-elastic response, which manifests the elastic–plastic transition. The {311} grains exhibit the second largest elastic strain while maintaining nearly a linear response. The {220} and {113} grains, on the other hand, display a lower elastic strain, indicating that they have a larger elastic stiffness. The macroscopic true stress-strain curve during *in-situ* tension at *RT* for $Al_{0.3}CoCrFeNi$ HEA after aging at 700 °C for 500 hours is presented in Figure 47(e), where the 0.2 pct proof stresses of $Al_{0.3}CoCrFeNi$ was determined as 300 MPa. Figures 47(f) and (g) show the ND patterns for $Al_{0.3}CoCrFeNi$ HEA after aging at 700 °C for 500 hours. It is clearly found that the secondary phase, B2 phase, was detected after long-time aging with primary FCC phase. The evolution of the $\{hkl\}$ lattice strains of the FCC matrix and B2 phase, as a function of the applied true stress at RT, are illustrated in Figure 47(h). In contrast to the lattice-strain evolution for homogenization-treated samples in Figure 47(d), the load transfer from the FCC matrix to B2 phase during plastic deformation was found, manifesting that the slope of the elastic strain of the FCC phase is increased, relative to the linear-elastic response, while the slope of the elastic strain of the B2 phase is reduced. As a result, the heat treatment introduces the secondary B2 phase into the FCC matrix, resulting in an increase in the yield strength from 145 to 300 MPa. During tensile deformation, the reduced slope of the elastic strain of the B2 phase reflects that the precipitate is still deforming elastically, and the additional plastic strain from the FCC matrix is transferred to the B2 phase.

As we described above, the deformation behaviors and strengthening mechanism for the FCC-structured $Al_{0.3}CoCrFeNi$ HEA, using the *in-situ* neutron experiments. However, the yield strength of the Al-containing HEAs, including the $Al_{0.3}CoCrFeNi$ HEA are lower than the BCC-structured HEAs, as mentioned in previous sections. Hence, Liaw's group and his colleagues went on to explore the unique deformation behaviors for refractory-type HEAs, employing the *in situ* neutron

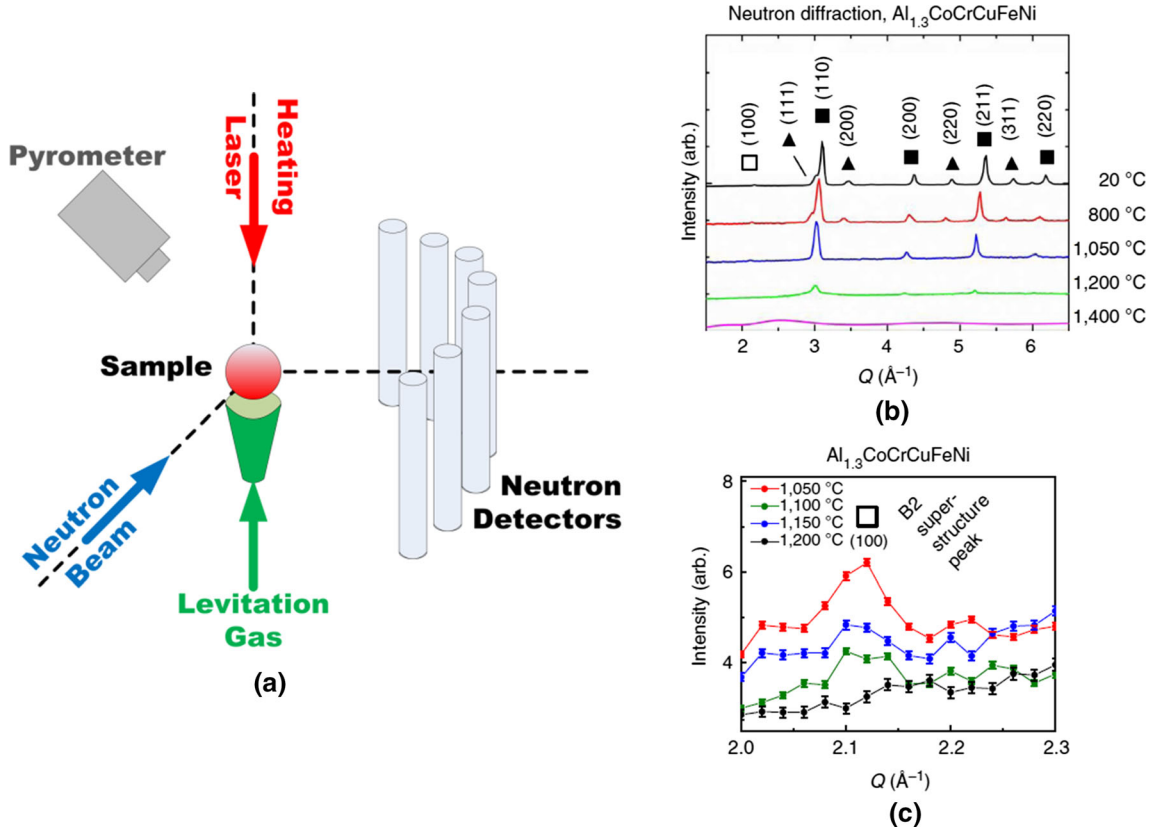

Fig. 45—(*a*) Schematic of the setup for the levitated ND experiment, and (*b*) ND patterns for the $Al_{1.3}CoCrCuFeNi$ HEA at various temperatures (The open square represents the disordered BCC phase, the solid squares are the BCC/B2 structures, and the triangles are FCC structures). (*c*) The weak B2 superstructure peak is present at temperatures up to at least 1150 °C.[47]

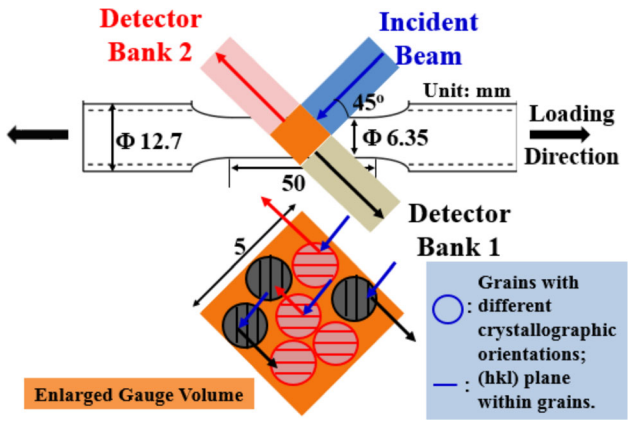

Fig. 46—Schematic of the sample dimension (unit in mm) and position for ND measurements of lattice-strain distributions during *in-situ* tensile loading for the $Al_{0.3}CoCrFeNi$ HEA. The beam size is 5 mm (reproduced from Ref. [46] with permission).

experiments as similar to the previous works in the $Al_{0.3}CoCrFeNi$ HEA. The *in-situ* ND with compression tests on the homogenization-treated NbTaTiV refractory HEA were carried out by Liaw's group and his colleagues to investigate the elastic-deformation behavior of grains with different orientations at elevated temperatures.[49,51] Figure 48 shows the lattice-strain evolution along the axial and transverse directions of the {110}, {200}, {211}, and {310} planes, during elastic deformation at elevated temperatures (*RT*, 500 °C, 700 °C, and 900 °C). The lattice strains were obtained from the following equation[49]:

$$\varepsilon_{hkl} = \frac{d_{hkl} - d^{i}_{hkl}}{d^{i}_{hkl}} \qquad [14]$$

where d_{hkl} is the *hkl* lattice spacing of the corresponding applied stress, and d^{i}_{hkl} is the *hkl* lattice spacing before loading. The slope of the lattice-strain evolution *vs* the applied stress, during elastic deformation, determines the diffraction elastic constants for the specific {*hkl*}-oriented planes. Different from the deformation behavior of the FCC-structured $Al_{0.3}CoCrFeNi$ HEA in Figure 47(d),[46] the variation in the diffraction elastic constants among all the oriented grains is not clearly observed, indicating the elastically-isotropic deformation behavior, as presented in Figure 48(a).

Unlike the lattice-strain evolution at *RT*, different slopes in the lattice strain *vs* applied stress at elevated temperatures are observed due to the increased elastic anisotropy, as presented in Figures 48(c), (e) and (g). At higher temperatures, where the overall stiffness is reduced, the anisotropy increases. The {200}-oriented grain exhibits the largest elastic lattice strain with the lowest stiffness, and the {310} grains undergo the second largest elastic strain with a nearly-linear response. On

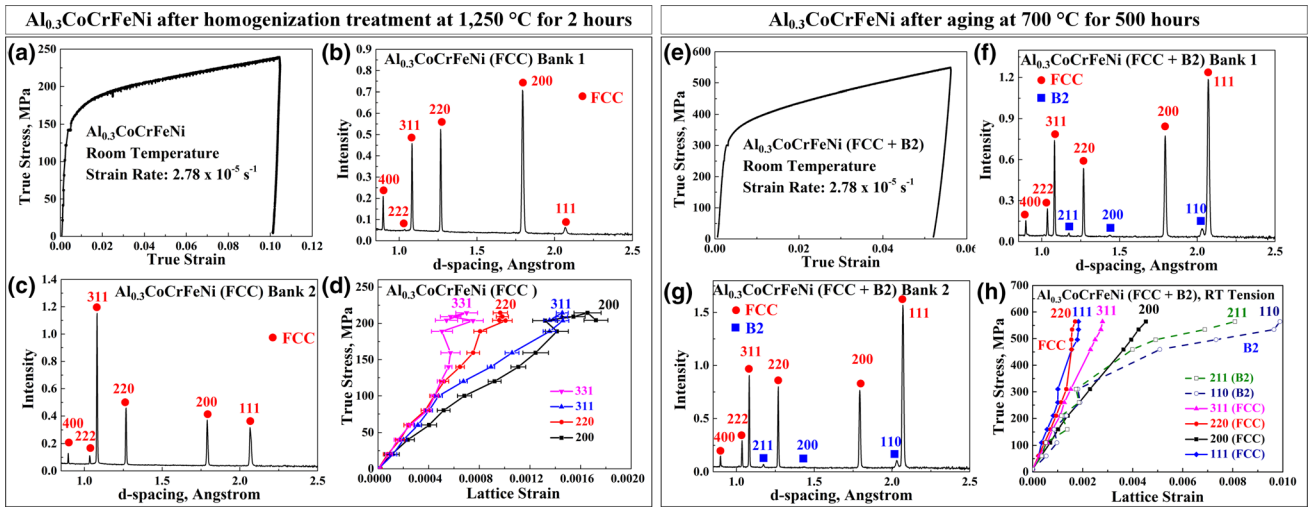

Fig. 47—*In situ* neutron-diffraction results for the $Al_{0.3}CoCrFeNi$ HEA after the homogenization treatment at 1250 °C for 2 h and aging at 700 °C for 500 hours. (*a and e*) The tensile stress-strain curves, (*b and f*) ND patterns, detected by Bank-1 detector, (*c and g*) ND patterns, detected by Bank-2 detector, and (*d and h*) evolution of lattice-strain result, obtained from the loading direction detector, of the current HEA as a function of applied stress during tension (reproduced from Ref. [46] with permission).

the other hand, the {110} and {211} grains display lower lattice strains and higher directional strength-to-stiffness ratios than other orientations. Moreover, the diffraction elastic moduli, E_{hkl}, of the different crystallographic planes at elevated temperatures shows almost the same values of elastic moduli in different orientations. This trend indicates that the NbTaTiV HEA exhibits the unique elastic-isotropic-deformation behavior at *RT*. Moreover, the elastic anisotropy gradually increases at elevated temperatures, but the variation in the rate of increase is not significant, which can be distinguished from other conventional alloys, including FCC-structured $Al_{0.3}CoCrFeNi$ HEA.

To better understand the underlying elastic-deformation behavior of the NbTaTiV refractory HEA, as a function of temperature, the macroscopic elastic, shear, and bulk moduli (E_M, G_M, and K_M) was obtained from the diffraction elastic moduli (E_{hkl}) and Poisson's ratio (ν), by applying the Voigt, Reuss, and Kroner models.[194, 195] Figures 48(b), (d), (f), and (h) indicate the reciprocal diffraction elastic moduli ($1/E_{hkl}$ and ν_{hkl}/E_{hkl}) as a function of the elastic-anisotropy factor, A_{hkl}, $\left[\frac{h^2k^2+k^2l^2+l^2h^2}{(h^2+k^2+l^2)^2}\right]$, which were obtained from the experimental elastic-lattice strain and calculated by the Voigt, Reuss, and Kroner models at room and elevated temperatures. It was found that the Kroner model is in the best agreement with the experimental data for all temperature ranges, as compared to the Voigt and Reuss models. The calculated single-crystal elastic constants, C_{ij}, macroscopic elastic (E_M), shear (G_M), bulk (K_M) moduli, and Poisson's ratio (ν) at room and elevated temperatures are listed in Figure 48. Further analysis of the elastic moduli was performed, using the resonant-ultrasound-spectroscopy.[51] The elastic constants, C_{ij}, were determined from ~ 45 resonances where the frequencies ranged from 100 to 650 kHz, by employing an iteratively inverse fitting process of the measured resonances.[51] The obtained values of the elastic moduli for the NbTaTiV alloy are summarized in Figure 48, indicating good agreement with the *in-situ* neutron data.

4. *Characterization of mobile dislocation in refractory HEA*

With the investigation of elastic-deformation behaviors above, the plastic-deformation behaviors of the NbTaTiV alloy, the line-profile modeling and analyses as a function of the macro-strain and temperatures are further conducted to confirm the dislocation motions. The plastic deformation leads to significant broadening of diffraction peaks, which is mostly caused by the formation of inhomogeneous strain fields. The inhomogeneity of the sub-grain structure is usually more associated with the accumulation of dislocations.[196] Hence, it gives rise to strain fluctuations with the strain field around dislocations responsible for diffraction-peak broadening.[197] Liaw's group and his colleagues have investigated the evolutions of diffraction-peak widths at different strain levels for the NbTaTiV refractory HEA, employing the Williamson–Hall peak-broadening analysis approach.[51,198]

Figure 49 exhibits the Williamson–Hall (W–H) plots for the NbTaTiV alloy corresponding to the macro-strain range from 0 to 15 pct. The response of linear fitting of the plot, which is obtained from the assumption of specific types of dislocations, refers to the dominant mobile dislocation character during plastic deformation.[199] When treating q and C_{h00} values as pure screw dislocations (q = 2.2244 and C_{h00} = 0.2415), the non-monotonous deviation of ΔK as a function of K^2C gradually increases with an increase in the macro-strain, as exhibited in Figure 49(a). On the other hand, when the values of ΔK and K^2C obtained with the pure edge-dislocation consideration (q = 0.0673 and C_{h00} = 0.1937), the obtained data follows a linear trend at all strain levels, as exhibited in Figure 49(b). These results reveal that edge dislocations are the dominant type of mobile dislocations of the NbTaTiV refractory

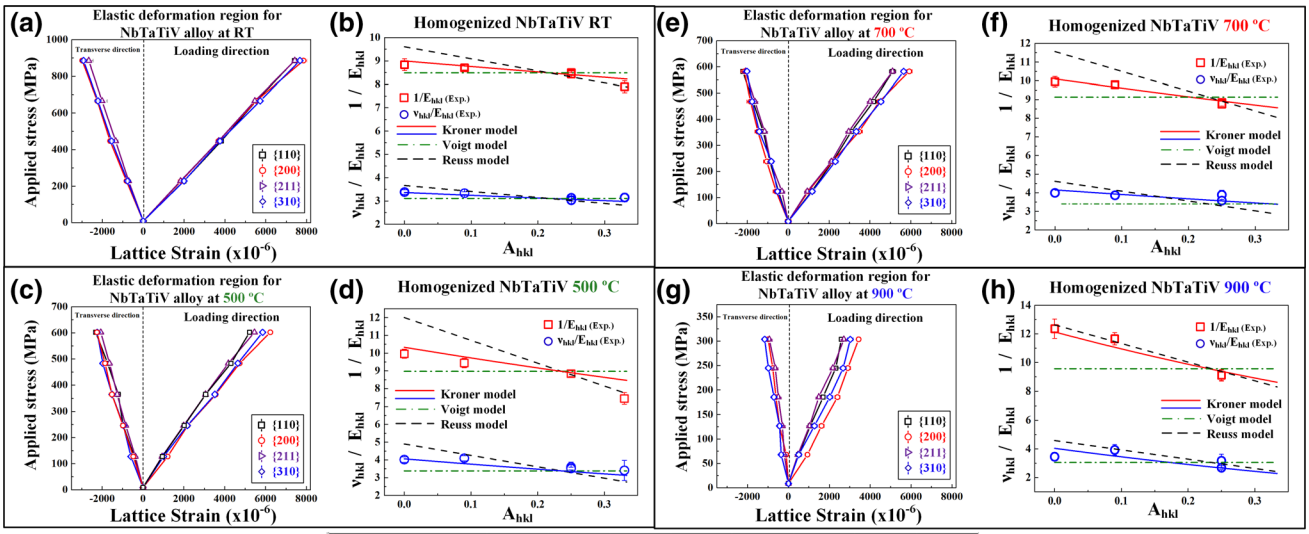

Conditions	Parameters	C_{11} (GPa)	C_{12} (GPa)	C_{44} (GPa)	C' (GPa)	E_M (GPa)	G_M (GPa)	K_M (GPa)	ν
Experimental Results	In-situ neutron at RT	196.8	121.4	46.7	37.7	117.3	42.9	146.6	0.368
	In-situ neutron at 500 °C	190.5	129.9	46.0	30.3	107.6	38.9	150.1	0.382
	In-situ neutron at 700 °C	184.3	122.5	45.9	30.9	107.9	39.3	143.1	0.376
	In-situ neutron at 900 °C	134.9	76.8	46.7	29.1	102.3	38.7	96.1	0.325
	RUS at RT	197.9	109.5	44.2	44.2	119.9	44.2	139.0	0.356
Theoretical Calculation Results	First-principles calculation at -273 °C	211.8	131.2	31.6	43.3	97.3	34.8	158.1	0.397
	First-principles calculation at RT	190.2	111.6	33.5	39.3	98.6	35.7	137.8	0.381
	Machine learning at RT	-	-	-	-	-	36.6	146.3	-

Fig. 48—Lattice-strain evolution in the NbTaTiV refractory HEA as a function of the applied stress, obtained from the *in-situ* ND experiments during the elastic deformation and plots of elastic moduli of differently-oriented crystals as a function of the elastic-anisotropy factor and fitting with the Kroner, Voigt, and Reuss models at (*a and b*) RT, (*c and d*) 500 °C, (*e and f*) 700 °C, and (*g and h*) 900 °C. The experimentally and theoretically obtained single-crystal and macroscopic-elastic moduli of the NbTaTiV alloy at elevated temperatures are summarized in table (Reprinted from Ref.,[51] under the terms of the Creative Commons CC BY-NC).

HEA is in the initial condition (non-deformed) at elevated temperatures. Moreover, with increasing macro-strains (up to 15 pct deformed), the ⟨111⟩ {110} edge dislocation remains as a dominant mobile dislocation character at room and elevated temperatures (Figures 49(b) through (d)).

Typically, the BCC metallic materials contain edge dislocations, which move faster than screw dislocations due to their core properties of dislocations during plastic deformation.[200] The critical stress, which forces the edge-dislocation movement, is quite small (< 10 MPa for the pure BCC Fe), leading to the easy annihilation of the edge dislocations, which results in the screw/edge anisotropy in the apparent mobility deviation.[200] Therefore, the remaining dislocations tend to have more screw character in BCC metals. In contrast to the conventional BCC metals, the dominant mobile dislocations of the investigated NbTaTiV BCC refractory HEA, which has severely distorted lattices, are close to ⟨111⟩ {110} edge dislocations with increasing macro-strain, as presented in Figure 49(b).

To support the results of identification of type of mobile dislocations, using W–H modeling, the visible evidence of the type of mobile dislocations was provided by the TEM study. Figures 49(e) and (f) show the filtered the high-angle-annular-dark-field (HAADF) scanning-transmission-electron-microscopy (STEM) image of the 15 pct RT-deformed NbTaTiV HEA, which are acquired along the [108] zone axis. The formation of edge dislocations is clearly observed with extra planes on the image, described by the symbol, "⊥", which is consistent with line-profile modeling, using W–H results (Figure 49(b)). It is found that these edge dislocations were formed on different oriented planes, indicated by various colored symbols of edge dislocations. Based on the reported comprehensive

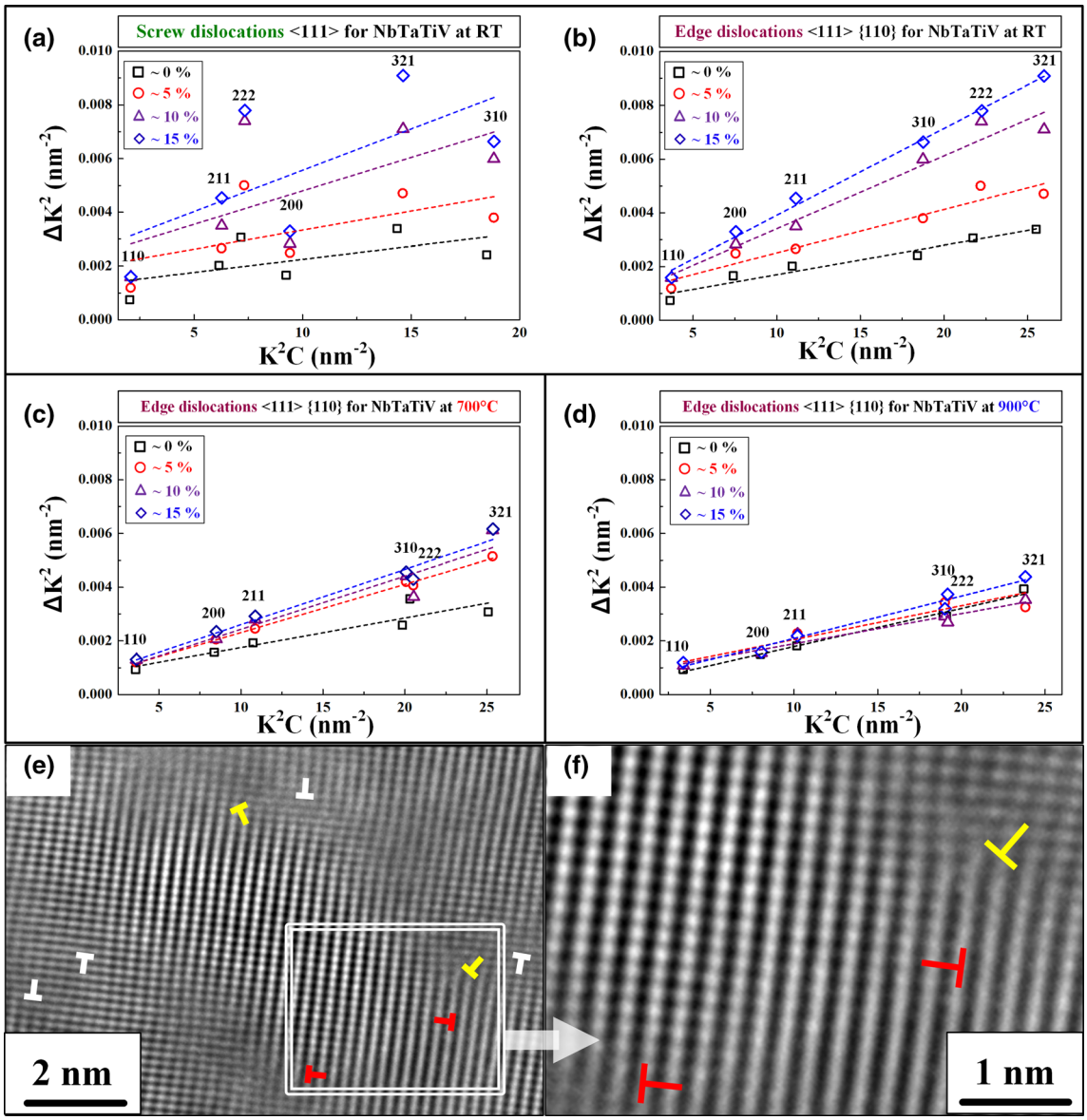

Fig. 49—Neutron-diffraction pattern line-profile modeling for the homogenized NbTaTiV alloy during plastic deformation at elevated temperatures. HAADF-STEM images of the RT-deformed NbTaTiV alloy. The peak-broadening analysis, ΔK^2, as a function of K^2C, for the sample compressed from 0 pct to 15 pct, considering the dominant type of dislocations as a pure (*a*) ⟨111⟩ screw dislocation at RT, (*b*) ⟨111⟩ {110} edge dislocation at RT, (*c*) ⟨111⟩ {110} edge dislocation at 700 °C, and (*d*) ⟨111⟩ {110} edge dislocation at 900 °C, respectively. (*e*) and (*f*) The visible investigation of the presence of edge dislocations for the 15 pct RT-deformed NbTaTiV HEA by the HAADF-STEM study (Reprinted from Ref. [51] under the terms of the Creative Commons CC BY-NC).

investigations of dislocation motions from Liaw's group and his colleagues above, it is clearly concluded that the severely-distorted lattice induces the deviation of the formation of dislocations from their neutral dislocation planes, which consequently, leads to a significant reduction in the mobility of edge dislocations during plastic deformation. Thus, the edge dislocations are believed to be the dominant dislocation type for the BCC refractory HEA, which is atypical, as compared to the conventional BCC metals and alloys.

In addition, Chen *et al.*[201] have investigated the dislocation motion in BCC-structured Co16.67Fe36.67-Ni16.67Ti30 HEA, using the atomistic simulation to confirm the dislocation mobility of edge and screw dislocations, compared with the α-Fe and Fe-5 at. pct Al solid solution. Different from the conventional BCC metals, the BCC HEAs inhomogeneity-imposed trapping of nanoscale segments of the moving dislocation constitutes the primary resistance to dislocation motion. The resultant inhomogeneities, while locally promoting kink nucleation on screw dislocations, trap them against propagation with an appreciable energy barrier, replacing kink nucleation as the rate-limiting mechanism. Edge dislocations encounter a similar activated process of nanoscale segment detrapping, with a comparable activation barrier. As a result, the mobility of edge dislocations, and hence their contribution to strength,

becomes comparable to screw dislocations. Wang *et al.*[202] further investigated the multiplicity of dislocation pathways at various temperatures in a refractory medium entropy alloy (MoNbTi), using the experimental observation coupled with atomistic calculations. Their results have confirmed the multiplanar non-screw dislocation dominant slip in MoNbTi, encouraged by the broad dispersion in the glide resistance for dislocations, owing to the atomic-scale chemical inhomogeneity. The ability of dislocations to choose the easy gliding direction and plane in the random field of multiple atomic species results in an excellent combination of strength and plasticity in the MoNbTi alloy with non-screw dominant dislocations, which is also an unusual mechanical characteristic, compared to conventional metallic alloys.

E. *Corrosion Resistance and Biocompatibility Studies*

Liaw's group and colleagues have performed multiple studies, which have examined the biocompatibility and corrosion behavior of HEAs.[146,203–208] Hua *et al.* examined the biocompatibility of a $Ti_xZrNbTaMo$ HEA (x = 0.5, 1, 1.5, and 2).[203] Here the samples biocompatibility was assessed, using multiple experimental techniques, such as wear and corrosion behavior testing. For corrosion testing, samples underwent PPTs in a PBS solution. For the wear behavior tests, samples were tested by a HSR-2M tribology tester using a 6-mm-diameter Si_3Ni_4 ball. The wear volume of the samples was evaluated employing a MT-500 Probe-type material surface-profile measuring instrument.

Results of the PPTs indicate that the HEAs exhibited corrosion rates that were comparable to the Ti6Al4V. In terms of the wear tests, Figure 50 displays a comparison of the wear rates for the HEAs and the Ti6Al4V under dry and wet sliding in the PBS solution, respectively. As indicated by the graph, the wear rates of the HEAs were all below 3.0×10^{-7} $mm^3 \cdot N^{-1} \cdot mm^{-1}$ for both the wet and dry sliding conditions. This trend is in contrast to the Ti6Al4V alloy, which had wear rates exceeding 3.0×10^{-7} $mm^3 \cdot N^{-1} \cdot mm^{-1}$ for both conditions. Furthermore, the wear rate for the wet-sliding condition in the HEAs was either lower or within a standard deviation of the dry-sliding condition. In contrast, the wear rate for the Ti6Al4V alloy was significantly greater for the wet sliding, as compared to the dry-sliding condition. It was surmised that the comparatively-better anti-corrosion and wear properties exhibited by the HEAs was likely a consequence of its multi-principal element composition. Based on the above results, the authors concluded that the Ti-Zr-Nb-Ta-Mo HEAs would perform better in biological environments, as compared to the Ti6Al4V alloy, making it a potential candidate for applications in the field of orthopedic-implant materials.

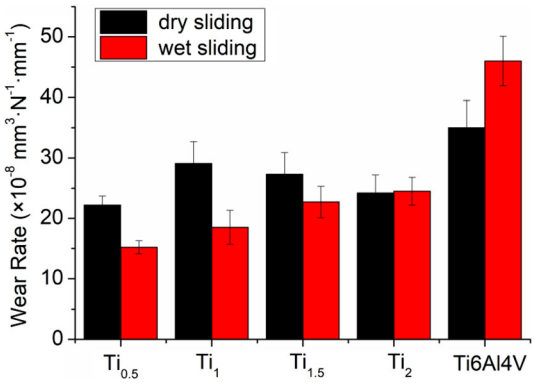

Fig. 50—Comparison of the wear rates for the $Ti_xZrNbTaMo$ (x = 0.5, 1, 1.5, and 2) HEAs and Ti6Al4V alloy under dry and wet sliding in the PBS solution, respectively (reproduced from Ref. [203] with permission).

In Reference 146 Shi *et al.* investigated the potentiodynamic-polarization behavior of a $Al_xCoCrFeNi$ (x = 0.3, 0.5, and 0.7) HEA exposed to a 3.5 weight percent (wt pct) NaCl solution. Here, samples were subjected to scan rates ranging from 10 to 1000 mV/min, from an initial potential of − 0.25 V *vs* the open circuit potential until the current density attained a value of 1 mA/cm^2. For reproducibility, the corrosion tests were performed 3 times per experimental condition.

The results of XRD characterization revealed that with an increase in the Al content, the alloy transformed from containing a solely FCC structure to containing both FCC and BCC phases. To complement the results of the XRD characterization, energy-dispersion X-ray spectroscopy (EDS) was also performed, see Figures 51(a) through (c). In Figure 51(a), the elements were distributed homogeneously in the $Al_{0.3}CoCrFeNi$. In contrast, the $Al_{0.5}CoCrFeNi$ and $Al_{0.7}CoCrFeNi$ HEA samples contained FCC and BCC regions that were (Al, Ni) and (Fe, Cr)-rich, respectively.

In terms of the corrosion tests, it was found that increasing the Al content in the alloy led to a decrease in its corrosion resistance. This decrease in the resistance was due to the corresponding rise in the amount of (Al, Ni)-rich, Cr-depleted BCC regions that are prone to attack by the Cl^- ions. The authors were also able to apply the MFT [see Eq. [4]] to the current fluctuations that occurred in the $Al_{0.3}CoCrFeNi$ HEA sample during the polarization tests. Figure 52 displays the CCDF curves for the current fluctuations. Where the scan rates varied from 50 to 300 mV/min. The inset of the figure shows the scale collapse with the corresponding MFT exponents of 1.39 and 0.23. It was suggested that the deviation of the first exponent from the model's prediction of 1.5 may be due to non-steady state fluctuations.[98]

Ching *et al.* examined the electronic structure, interatomic bonding, and mechanical properties of 13 bioinspired HEAs using advanced computational techniques, such as the Vienna *Ab initio* Simulation Package (VASP).[209,210] To determine the mechanical properties, they used the response analysis scheme [211] on a fully-relaxed BCC supercell (consisting of 250 atoms) structure that was produced *via* the VASP. Here, the stress was determined by the following equation:

$$\sigma_i = \sum_{j=1}^{6} C_{ij}\varepsilon_j \qquad [15]$$

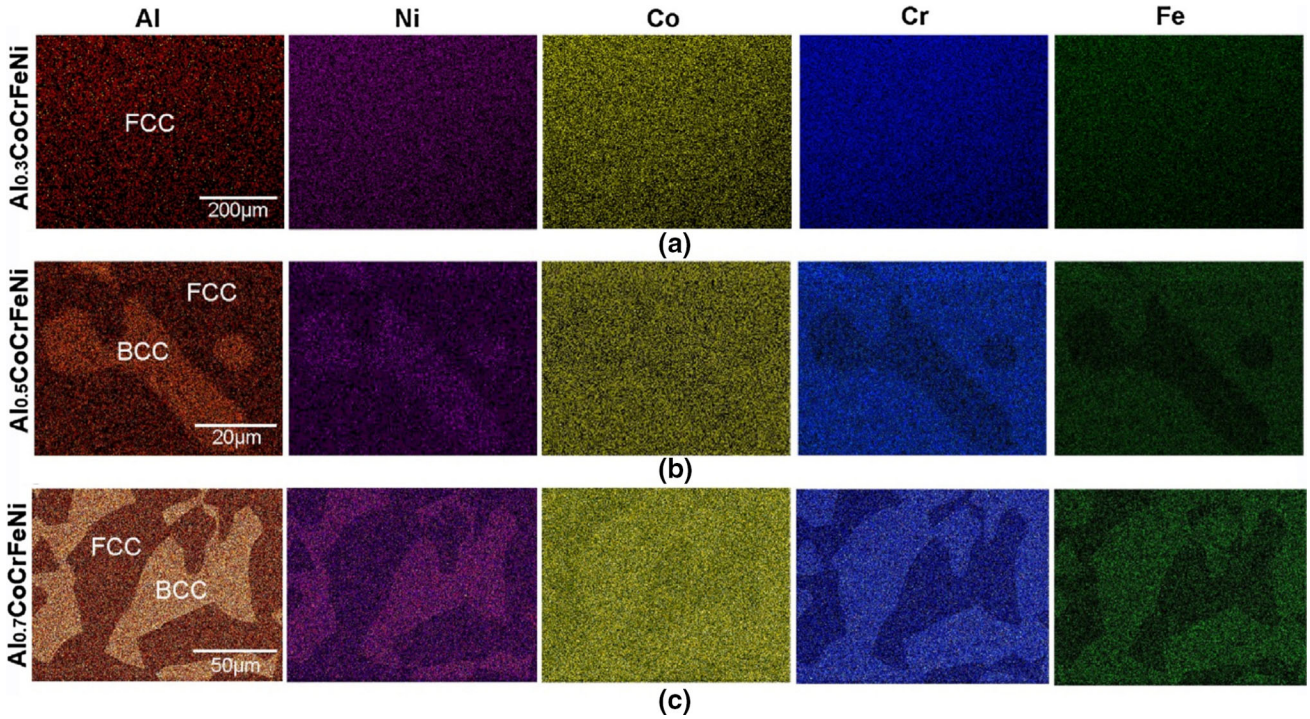

Fig. 51—EDS mappings that show the phase and elemental distribution in the (*a*) $Al_{0.3}CoCrFeNi$, (*b*) $Al_{0.5}CoCrFeNi$, and (c) $Al_{0.7}CoCrFeNi$ HEAs (reproduced from Ref. [146] with permission).

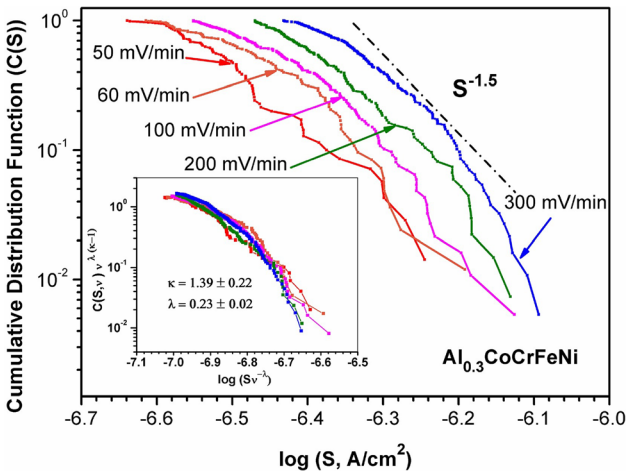

Fig. 52—The CCDF curves for the $Al_{0.3}CoCrFeNi$ HEA sample that underwent polarization tests at scan rates ranging from 50 to 300 mV/min. The inset of the figure features the scaling collapse of the curves with the MFT universal exponents of 1.39 and 0.23 (reproduced from Ref. [146] with permission).

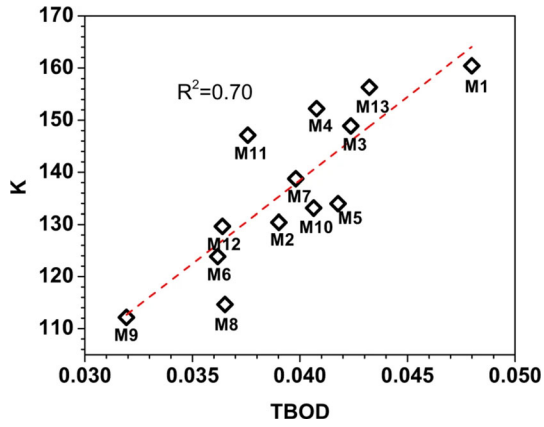

Fig. 53—Plot of the bulk modulus *vs* TBOD for 13 HEAs (Reprinted from Ref. [209] under the terms of the Creative Commons CC BY 4.0).

where C_{ij} is the elastic coefficient, and ε_j is the strain. From here, factors, such as the porosity, stress tensor, bulk modulus, shear modulus, Young's modulus, and Poisson's ratio could be obtained, using the Voigh-t-Reuss–Hill polycrystalline approximation.[212] In addition to the above factors, quantum mechanical metrics, such as the total bond order density (TBOD) and partial bond order density, were also determined. Figure 53 displays the bulk modulus, K, as a function of the TBOD. It is apparent from the figure that that there was a clear correlation between K and the TBOD.

The results of the study led to the following important conclusions. First, the investigation provided a proof-of-concept that supercell modeling can provide a guideline on how to introduce porosity to reduce the Young's modulus in HEAs to improve their biocompatibility. Second, quantum mechanical metrics, such as TBOD and the partial bond order density (PBOD), could be implemented to better understand the structure of HEAs. Thirdly, the methods and approaches used in this study can be readily extended to other multi-phase HEAs. Lastly, it is possible to more realistically model

biocompatible HEAs in an aqueous solution or body fluids to better understand their behavior in environments typical of implant materials.

F. *Structural and Thermodynamic Modeling of HEAs*

The comprehensive experimental investigations of various HEAs have been conducted, such as phase identifications, microstructural evolution, mechanical properties, and deformation behaviors, using state-of-the-art techniques, as described in previous sections. Based on these extensive experimental efforts, Liaw's group and his colleagues have verified the deformation mechanism and local atomic structures through the theoretical calculations and modeling, such as first-principles calculations, machine learning (ML), *ab initio* molecular dynamics (AIMD) simulations, and crystal-plasticity finite-element-modeling (CPFEM).[45–47,50,51]

1. *First-principles calculations*

With the *in-situ* neutron experimental results for the $Al_{0.3}CoCrFeNi$ HEA, which are displayed in Figure 47(d), confirm the elastic properties of the Al-containing HEA that were predicted by first principles calculations.[50] The elastic constants of the HEA were calculated using a special-quasi-random-structure (SQS) with the density-functional-theory (DFT) and exact-muffin-tin orbitals-coherent-potential-approximation (EMTO-CPA). Figure 54 presents the calculated and experimentally obtained elastic constants for the $Al_{0.3}CoCrFeNi$ HEA, which shows that the SQS model is in good agreement with the ND data. The Young's and shear moduli and Poisson's ratio also have been

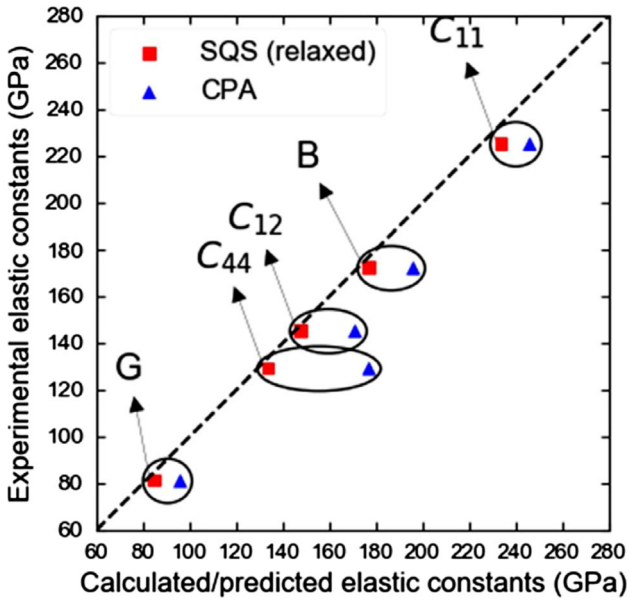

Fig. 54—Comparison of experimental and calculated elastic constants. Elastic constants of C_{11}, C_{12}, and C_{44}, elastic moduli: bulk modulus, B, and shear modulus, G. Comparison of experimental (ND) and calculated (SQS and CPA) elastic constants and elastic moduli of the $Al_{0.3}CoCrFeNi$ HEA (reproduced from Ref. [50] with permission).

Fig. 55—Spatial dependence of Young's and shear moduli and Poisson's ratio and machine learning model of the $Al_{0.3}CoCrFeNi$ HEA. (*a*), (*c*), and (*e*): The two-dimensional (2D) projections of Young's moduli, shear moduli, and Poisson's ratios on the XY, XZ, and YZ planes, respectively. (*b*), (*d*) and (*f*): The 3D visualization of Young's moduli, shear moduli, and Poisson's ratios. Learning curves showing the dependence of model prediction performance (mean squared error) on number of samples in the training dataset. (*g*) Shear modulus learning curves. (*h*) Bulk modulus learning curves (reproduced from Ref. [50] with permission). ▶

predicted by DFT calculations, based on theoretically-obtained elastic constants. The obvious anisotropic elastic properties of the $Al_{0.3}CoCrFeNi$ HEA are presented in Figure 55, indicating that there is a large deviation from the spherical geometry in the three-dimensional (3D) representation. Moreover, the Young's modulus changes significantly for different crystal orientations. The lowest and highest calculated values of Young's modulus are 126.8 GPa in the [001] orientation and 324.1 GPa in the[109] orientation, respectively (Figures 55(a) and (b)). Furthermore, it is also clearly found that the shear modulus significantly depends on the stress direction, and Poisson's ratio has similar characteristics. The lowest and highest values for the shear moduli are 45.9 GPa in the[109] direction, and 135.5 GPa in the [001] direction, respectively. The Poisson's ratio is maximized at $\nu = 0.728$, as the str*etch*ing along the diagonal directions,[98] induces the lateral contraction along the axial directions, [010]. It also can be seen in Figures 55(c) through (f) that there was a negative Poisson's ratio of $\nu = -0.155$ in the $\langle 110 \rangle$ directions. A negative Poisson's ratio along certain crystallographic directions in the $Al_{0.3}CoCrFeNi$ HEA is in line with various studies of materials with the large anisotropy.[213–215] The calculated bulk, shear moduli, and Poisson's ratio by DFT and EMTO-CPA are 177, 85 GPa, and 0.29 (DFT) and 196, 96 GPa, and 0.29 (EMTO-CPA), respectively. The bulk and shear moduli have been further predicted by ML. The ML models have the advantage of being extremely fast, compared to computing the property values using DFT. The gradient boosting trees algorithm,[216,217] for example, is used to build a model to predict the bulk and shear moduli. The features of the model are subsequently analyzed to obtain insights into the dependence of the predictions on feature values. Figures 55(g) and (h) indicate the learning curves for the bulk and shear moduli of the $Al_{0.3}CoCrFeNi$ HEA. The *y*-axis corresponds to the mean squared error (MSE) values. The models were applied to log-normalized bulk and shear modulus values, and an MSE value reflects a ratio between the predicted and actual values, as opposed to an arithmetic difference. The ML-predicted values of the bulk and shear moduli for the $Al_{0.3}CoCrFeNi$ HEA are 161 and 73 GPa, indicating the good agreement with the DFT-calculation and ND experimental results.

2. *Crystal plasticity finite element methods*

The crystal plasticity finite element method (CPFEM) has been employed to simulate the strain evolution of the $Al_{0.3}CoCrFeNi$ HEAs during tensile deformation and validate the *in-situ* neutron-diffraction tension

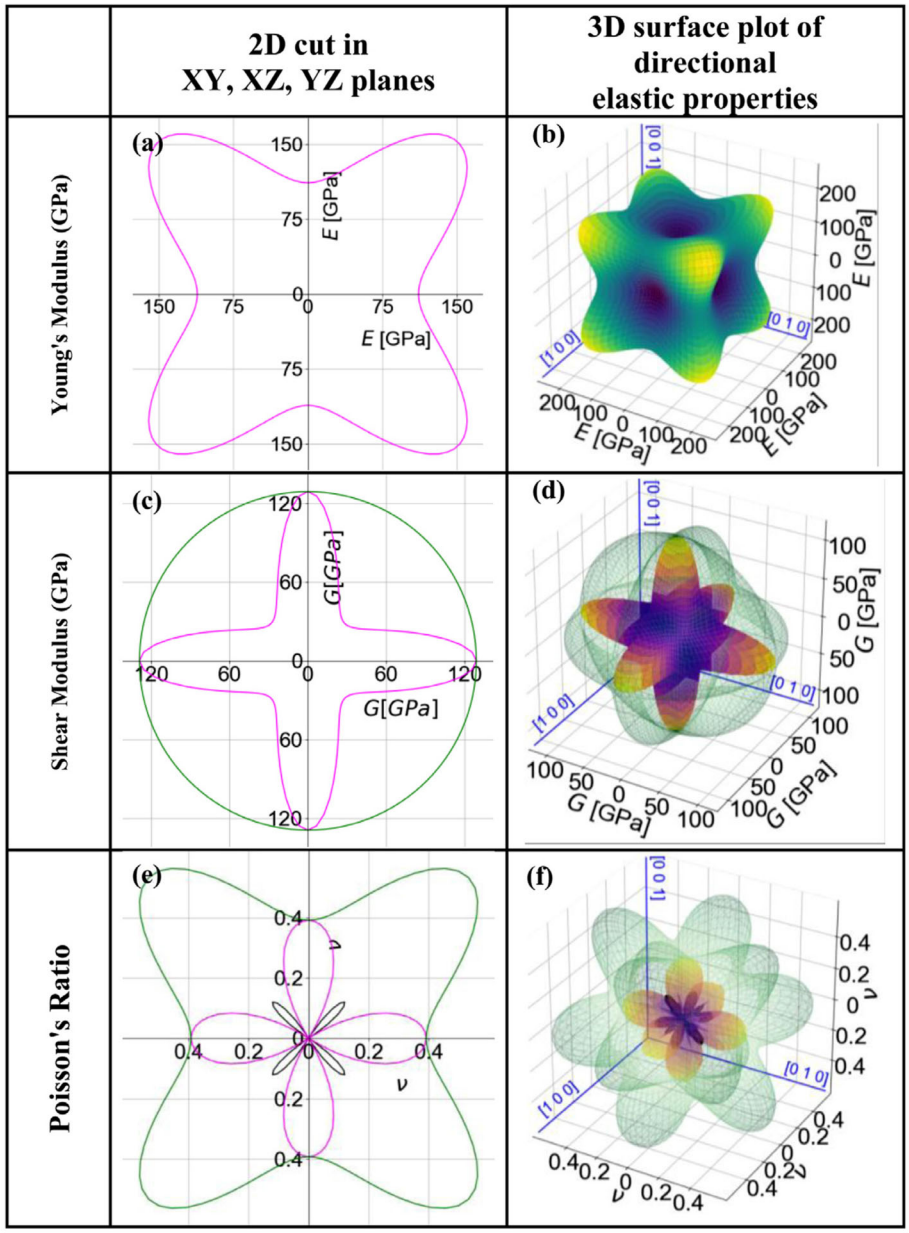
2D cut in
XY, XZ, YZ planes
3D surface plot of
directional
elastic properties
Young's Modulus (GPa)
Shear Modulus (GPa)
Poisson's Ratio
(a)
(b)
(c)
(d)
(e)
(f)
E [GPa]
G[GPa]
ν
[0 0 1]
[1 0 0]
[0 1 0]

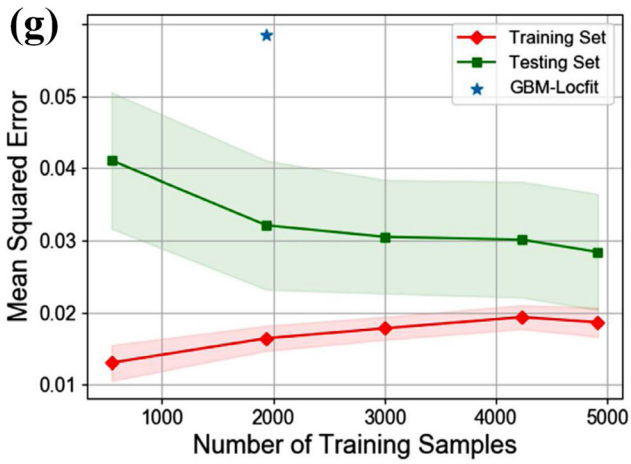
(g)
Training Set
Testing Set
GBM-Locfit
Mean Squared Error
Number of Training Samples

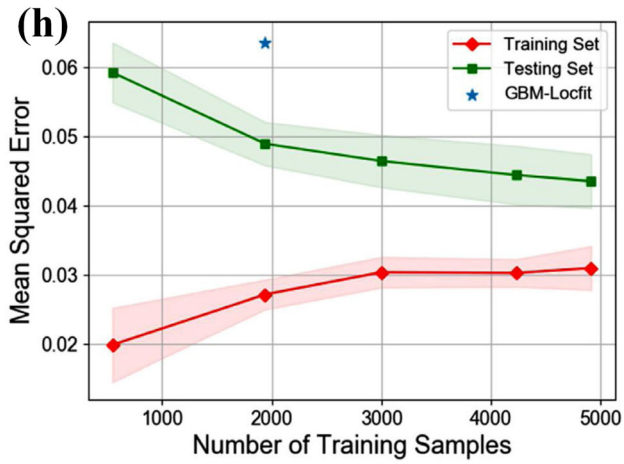
(h)
Training Set
Testing Set
GBM-Locfit
Mean Squared Error
Number of Training Samples

results (Figure 47).[46] The CPFEM is based on the crystal-plasticity theory.[218] The plastic-deformation rate for the Schmid-type crystal plasticity can be calculated as the summation over all slip systems[219–221]:

$$\dot{F}^{p}_{ik}F^{p-1}_{kj} = \sum_{\alpha'=1}^{N_{\text{slip}}} \dot{\gamma}^{(\alpha')} s_i^{(\alpha')} m_j^{(\alpha')} \quad [16]$$

where F^{p}_{kj} is the plastic-deformation gradient, N_{slip} is the total number of all activated slip directions, $\dot{\gamma}^{(\alpha')}$ is the slip rate of the α'-th slip, $s_i^{(\alpha')}$, and $m_j^{(\alpha')}$ are the slip direction and the slip plane normal, respectively. The slip rate can be given by the power-law flow rule[220,221]:

$$\dot{\gamma}^{(\alpha')} = \dot{\gamma}_0 \left| \frac{\tau^{(\alpha')}}{\tau^{(\alpha')}_{\text{flow}}} \right|^{n'} \text{sgn}\left[\tau^{(\alpha')}\right] \quad [17]$$

where $\dot{\gamma}_0$ is the reference value of the slip rate, $\tau^{(\alpha')}$ and $\tau^{(\alpha')}_{\text{flow}}$ are the resolved shear stress and flow strength of the α'-th slip, respectively, and n' is the stress exponent. The flow strength, $\tau^{(\alpha')}_{\text{flow}}$, can also be described by the Peirce–Asaro–Needleman hardening law:

$$\dot{\tau}^{(\alpha')}_{\text{flow}} = \sum_{\beta'} h_{\alpha'\beta'} \left| \dot{\gamma}^{(\beta')} \right| \quad [18]$$

where $h_{\alpha'\beta'}$ is the hardening moduli, and the self-hardening modulus can be represented as[219–221]:

$$h_{\alpha'\alpha'} = h(\gamma) = h_0 \text{sech}^2 \left| \frac{h_0 \gamma}{\tau_s - \tau_0} \right| \quad [19]$$

where h_0 is the initial hardening modulus, τ_0 is the initial slip strength, and τ_s is the saturated slip strength, and γ is the accumulated shear strain on all slip systems[219,221]:

$$\gamma = \int_0^t \sum_{\alpha'} \left| \dot{\gamma}^{(\alpha')} \right| \text{d}t \quad [20]$$

The latent-hardening moduli are given by[219–221]:

$$h_{\alpha'\beta'} = h(\gamma)\left[q + (1-q)\delta_{\alpha'\beta'}\right] \quad [21]$$

where $\alpha' \neq \beta'$, and q is the latent hardening coefficient. Among all the grains, we choose the ones whose $\{hkl\}$ planes satisfy the diffraction condition. That is, their $\langle hkl \rangle$ directions are parallel to the diffraction vector. In practice, a small tolerance of ± 5 deg is allowed between these two vectors to obtain the sufficient fraction of grains. Then, the lattice strain, ε_{hkl}, is evaluated by[219,220]:

$$\varepsilon_{hkl} = \frac{\sum_{N=1}^{N_{\text{grain}}} \int \varepsilon_{ij}^{\text{elastic}} q_i q_j \text{d}\Omega_N}{\sum_{N=1}^{N_{\text{grain}}} \int \text{d}\Omega_N} \quad [22]$$

where N_{grain} denotes the number of grains whose direction is within ± 5 deg with respect to the diffraction vector, q_i is the component of the diffraction vector, $\varepsilon_{ij}^{\text{elastic}}$ is the Lagrange–Green strain[219,220]:

$$\varepsilon_{ij}^{\text{elastic}} = \frac{1}{2}\left(F^{e}_{ik}F^{e}_{kj} - \delta_{ij}\right) \quad [23]$$

where F^{e}_{ik} is the elastic-deformation gradient.

The predicted CPFEM results of the stress–strain curves and lattice strain evolution for the $Al_{0.3}$CoCrFeNi HEAs after the homogenization treatment at 1250 °C for 2 hours (single-phase) and aging at 700 °C for 500 hours (dual-phase) are presented in Figure 56.[46] For the single-phase $Al_{0.3}$CoCrFeNi HEA in Figure 56(c), the lattice-strain splitting during elastic deformation displays the elastic anisotropy for different grains, which agree with the experimental results. More specifically, the stresses transfer among differently-oriented grains after yielding. Furthermore, the hard-oriented grains undertake higher stresses with larger lattice strains, whereas the soft-oriented grains undergo lower stresses with lower lattice strains, resulting in nonlinear lattice-strain evolution during plastic deformation. Figure 56(d) shows the stress distribution in the representative volume element (RVE) after deformation for the dual-phase $Al_{0.3}$CoCrFeNi HEA. The highlighted green cubic units represent grains of the B2 phase, which indicates that the B2 phase is subjected to a higher stress than the FCC matrix after plastic deformation. The predicted lattice-strain evolution as a function of the applied stress is presented in Figure 47(d). The solid lines are prediction data, while the symbols are experimental results. Different from the lattice-strain evolution in the single-phase $Al_{0.3}$CoCrFeNi HEA in Figure 47(d), the rate of increase in the lattice strain of the B2 phase drops dramatically after yielding. Additionally, the huge splitting of the FCC and B2 phases imply the stress partitioning in the dual-phase HEA. As a result, the stresses transfer to the B2 phase from the FCC matrix, which could delay the localized failure and enable an overall higher degree of plastic deformation.

In addition to the in-depth study of elastic- and plastic-deformation behaviors via DFT and CPFEM modeling for single and dual-phase $Al_{0.3}$CoCrFeNi HEAs, Liaw's group and his colleagues have investigated the possible local-ordering behaviors for the $Al_{1.3}$CoCrCuFeNi HEA, using the pair distribution function (PDF) analysis resulting from the ND experiments coupled with AIMD simulation.[47,222–224] Figure 57 shows the neutron PDF and calculated results of the $Al_{1.3}$CoCrCuFeNi HEA at *RT*. The observed PDF approximately matches the periodic atomic arrangement related with the present structures, such as B2, BCC, and FCC structures. However, the greatest mismatch also occurs at short distances (less than 10 Å), which results from the presence of local lattice distortions that are due to the atomic-size mismatch in solid solutions. The cumulative effect of the local lattice distortion is similar to that of thermal displacement at long distances. Hence, the observed PDF matches well with the ideal model at large distances, as presented in Figure 57(a). When the temperature increases to 1400 °C, the observed PDF result shows reasonably good

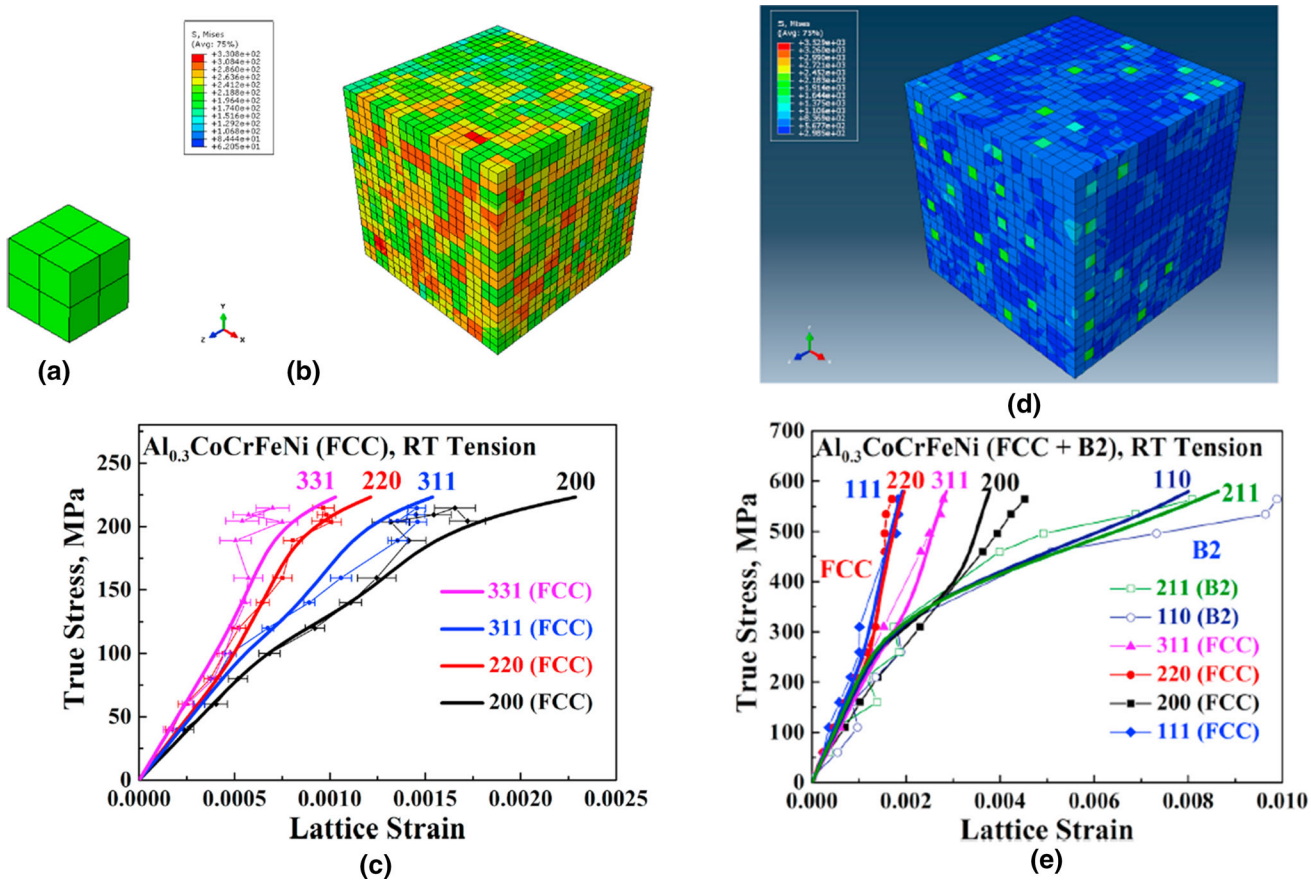

Fig. 56—The finite element simulation, as performed on a tension specimen after homogenization treatment at 1250 °C for 2 h and aging at 700 °C for 500 h. Each grain of (*a*) is represented by 8 cubic elements in the overall setup in (*b and d*). The lattice strain evolution for the $Al_{0.3}CoCrFeNi$ HEA after homogenization at 1250 °C for 2 h (*c*) and aging at 700 °C for 500 h (*e*) (reproduced from Ref. [46] with permission).

agreement with a model having short- and medium-range order. Furthermore, the amplitudes of the PDF peaks diminish at distances beyond ~ 15 Å, which is consistent with a liquid phase or BMG[84] (Figure 57(b)). Overall, the present PDF experiments indicate that there is an interesting connection between the short- and medium-range structures of liquid and solid phases.

3. *Ab initio molecular dynamics (AIMD) simulations*

The local atomic structure of the liquid status in the $Al_{1.3}CoCrCuFeNi$ HEA have been further predicted by AIMD simulations, as presented in Figures 57(c) through (e). Figure 57(c) illustrates the AIMD snapshot of a liquid structure at 1400 °C. The AIMD-simulations were run, both with and without constraints from the experimental input.[47,225] The AIMD simulated PDF results are in good agreement with the experimentally-observed PDF data (Figure 57(d)) when constrained to match the density obtained from the experimental fit (Figure 57(b)). The unconstrained AIMD predicts a higher density, with peaks shifted to smaller pair separations. The AIMD-simulated PDF may be separated into the partial pair correlation function ($g_{\alpha\beta}$) for all possible atom pairs. The predicted $g_{\alpha\beta}$ values indicate that Al-Ni, Cr-Fe, and Cu-Cu nearest-neighbor pairs occur much more frequently than Al-Al and Cr-Ni pairs, as shown in Figure 57(e). The predictive nature of AIMD simulations suggests that they can be used to qualitatively guide screening single-phase HEA compositions that should minimize short-range chemical ordering or segregation in the liquid state.[47,225]

4. *Monte Carlo simulations*

Furthermore, Liaw's group and his colleagues have developed the prediction of phase and microstructure evolution methods for Al-containing HEAs, through high-throughput Monte Carlo (MC) technique.[226] The MC model is based on the experimental data of the $Al_xCoCrFeNi$ phases. The predicted phase evolution during cooling involves only redistributions of the atomic population, as an approximation to the behavior of presented alloys undergoing sublattice ordering and coherent phase separation. Figure 58 illustrated the predicted two-step phase evolutions of AlxCoCrFeNi for $1 < x < 2$ HEA during cooling. The BCC solid-solution phase transforms into a partially-ordered B2 phase at high temperatures. The atomic distributions for a series of different temperatures have been determined, using supercells, composed of $12 \times 12 \times 24$ cubic unit cells, where each unit cell contains one α and one β

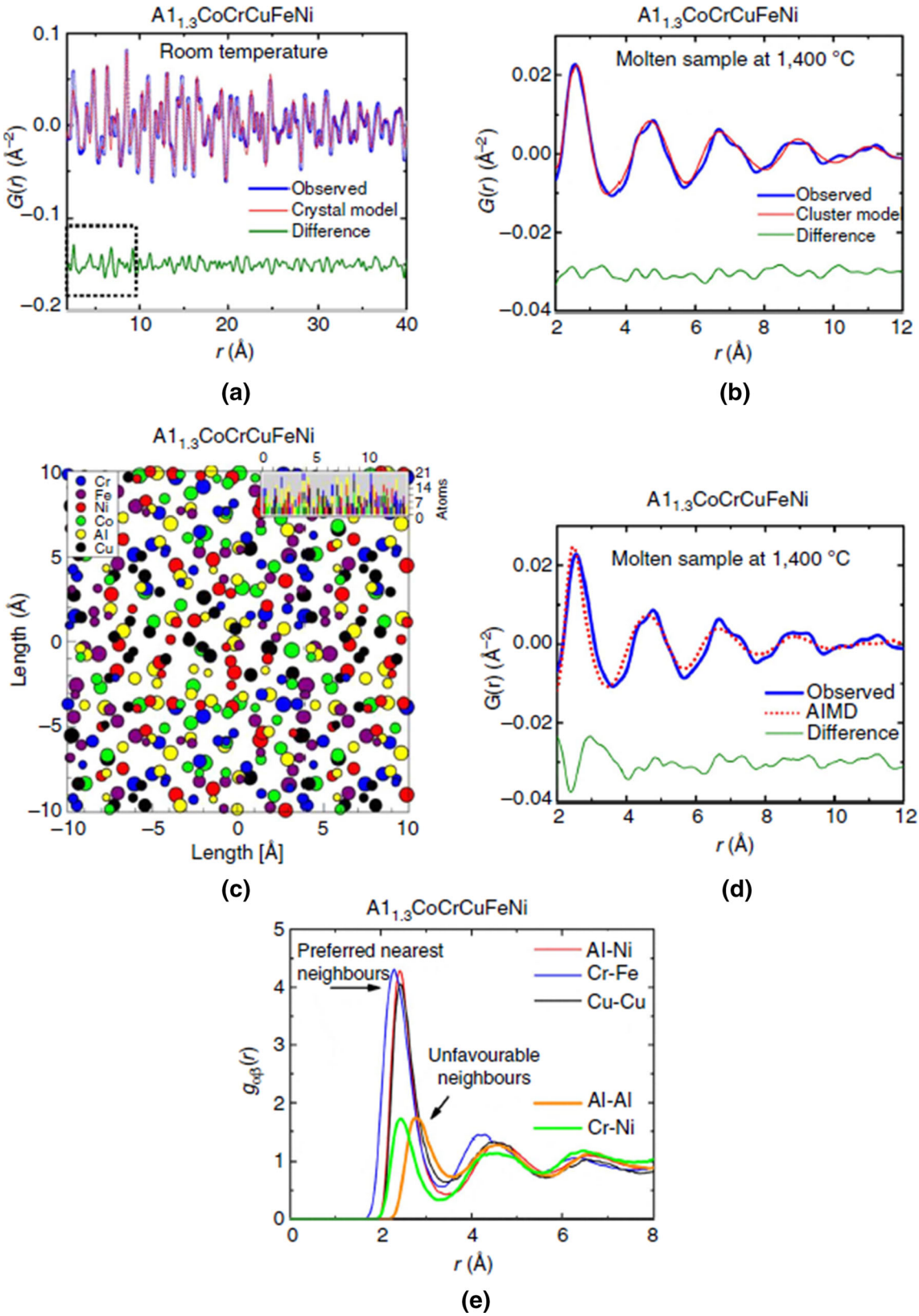

Fig. 57—The local structure of the $Al_{1.3}CoCrCuFeNi$ HEA. (*a*) Neutron PDF and calculated PDF data at RT (*b*) Neutron PDF and calculated PDF data at 1400 °C, (*c*) AIMD simulation snapshot of the liquid structure at 1400 °C, (*d*) Neutron PDF and AIMD-simulated PDF data at 1400 °C, and (*e*) Selected partial pair correlation functions, $g_{\alpha\beta}(r)$ simulated by AIMD.[47]

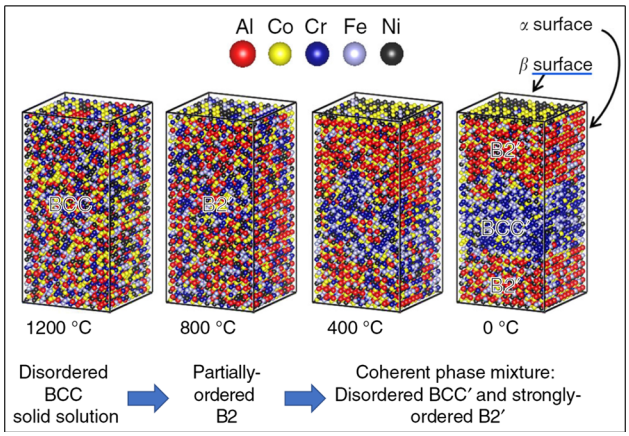

Fig. 58—Monte Carlo simulations of a two-step cooling transformation in the AlCoCrFeNi HEA[226]

sites. The supercells are "cut" to highlight configurational ordering, such that the side surfaces contain Al-rich α sites, and the top surface contains Al-poor β sites. Based upon the element-specific long-range order parameters, it is found that the BCC solid-solution phase transforms into a partially-ordered B2 phase during cooling to 800 °C. Upon further cooling, the partially-ordered phase transforms into a mixture of the disordered Cr-Fe-enriched BCC and strongly ordered Al-Co-Ni-enriched B2 phases. This calculation result is consistent with the experimentally observed main phase transformation in the Al_xCoCrFeNi HEA.[47,227–229]

To further demonstrate the feature of phase evolutions in the Al_xCoCrFeNi HEAs during cooling, the configurational order of composed elements has been simulated by MC simulations, as presented in Figure 59. These calculations are the described feature of the ordering onset, *i.e.*, where the HEA is cooled below the ordering temperature, T_c. The Al elements segregate to one sublattice with the Ni and Co primarily occupying the other sublattices. The influence of the Al content on phase evolution was clarified by comparing the higher Al-content (Al2CoCrFeNi) and lower Al-content (AlCoCrFeNi) HEA systems. In the Al2CoCrFeNi alloy, T_c is above the experimental melting point, such that the alloy cannot form disordered phases. Instead, the alloy could partially form ordered phases at the melting temperature. On the other hand, the AlCoCrFeNi, T_c occurs in the solid phase, near 1200 °C. The fraction of Al-Al pairs is low at all temperatures, exhibiting that the Al atoms are primarily pairing with the transition metals even above the B2-transformation temperature. Interestingly, as the Al content increases, the fraction of Al-Al pairs decreases, opposite of what would normally be expected for a disordered material. Thus, it can be concluded that the short-range order around the Al atoms can be formed in the disordered BCC phase at high temperatures.

The advantage of the MC simulations is that it could build in the enthalpies associated with forming ordered phases, while simultaneously capturing the large amounts of disorder, which occurs in each of the phases. These high-throughput simulations are based entirely on nearest-neighbor interactions on a rigid lattice, in the same fashion as the early studies on binary systems, and successfully reproduce major features of the phase evolution observed in Al-containing HEAs.

5. *Calculations and measurements of lattice distortion*

As described in previous sections, the BCC refractory HEAs have a high yield strength and comparable plasticity at elevated temperatures among the newly-designed HEAs (Table I). The present refractory HEA, NbTaTiV, possesses a single BCC solid-solution phase with chemical homogeneity.[49] Thus, the dominant strengthening mechanism should be solid-solution strengthening. Liaw's group and his colleagues have demonstrated the solid-solution strengthening effect on yield strength for the NbTaTiV refractory HEA, using theoretical calculations coupled with first-principles calculations.[49] The solid-solution strengthening of the NbTaTiV refractory HEA was determined, considering the elastic-modulus and atomic-size mismatches, as expressed by the following equation[63, 78, 230]:

$$\begin{aligned}\Delta\sigma_s &= \Delta\sigma_G(\text{elastic - modulus mismatch}) \\ &\quad + \Delta\sigma_a(\text{atomic - size mismatch}) \\ &= \alpha G\left(\frac{9}{8}\sum c_j\delta_{Gij}\right)^{\frac{4}{3}} c_i^{\frac{2}{3}} + \alpha G\beta\left(\frac{9}{8}\sum c_j\delta_{aij}\right)^{\frac{4}{3}} c_i^{\frac{2}{3}} \quad [24]\end{aligned}$$

where α is a dimensionless material constant (0.04),[78] G is the shear modulus of the alloy, which is determined by the rule of mixtures (49.5 GPa for NbTaTiV), β is the dislocation type-dependent constant, c_j is the atomic fraction of the jth element in the alloy, δ_{aij} and δ_{Gij} are the atomic-size and modulus differences, $\delta_{aij} = \frac{2(r_i - r_j)}{(r_i + r_j)}$, $\delta_{Gij} = \frac{2(G_i - G_j)}{(G_i + G_j)}$, $r_i(G_i)$, and $r_j(G_j)$ are the atomic radii (shear moduli) of the ith and the jth elements, and c_i is a solute concentration. Based on the theoretical calculation of strengthening by the atomic-size mismatch, the relationship between the degree of strengthening and distorted lattice of the HEAs was quantitatively determined by theoretical and experimental approaches. The lattice distortion factor, $M^D = 8\pi^2(\bar{u}^2)^D\left(\frac{\sin\theta}{\lambda}\right)^2$, is simply formulated from the Debye–Waller temperature factor, $M^T = 8\pi^2(\bar{u}^2)^T\left(\frac{\sin\theta}{\lambda}\right)^2$, where θ and λ are the angle and wavelength of the incident X-ray beam, and the amplitude of the deviation displacement of atoms ($\bar{u}^D$) was substituted instead of the thermal vibrational amplitude ($\bar{u}^T$).[231] In this case, the $\bar{u}^D$ is a dominant effective term to determine the lattice-distortion factor, M^D, which is expressed as[231]:

$$\bar{u}^D = \sqrt{\sum_i^n \left(d_i^{\text{eff}} - \bar{d}\right)^2 / n} \quad [25]$$

where d_i^{eff} is the effective interatomic distance of the ith element, $\bar{d}$ is the average interatomic distance of n elements, which are obtained from the lattice constant of the incorporated elements associated with their respective crystal structures, and n is the number of

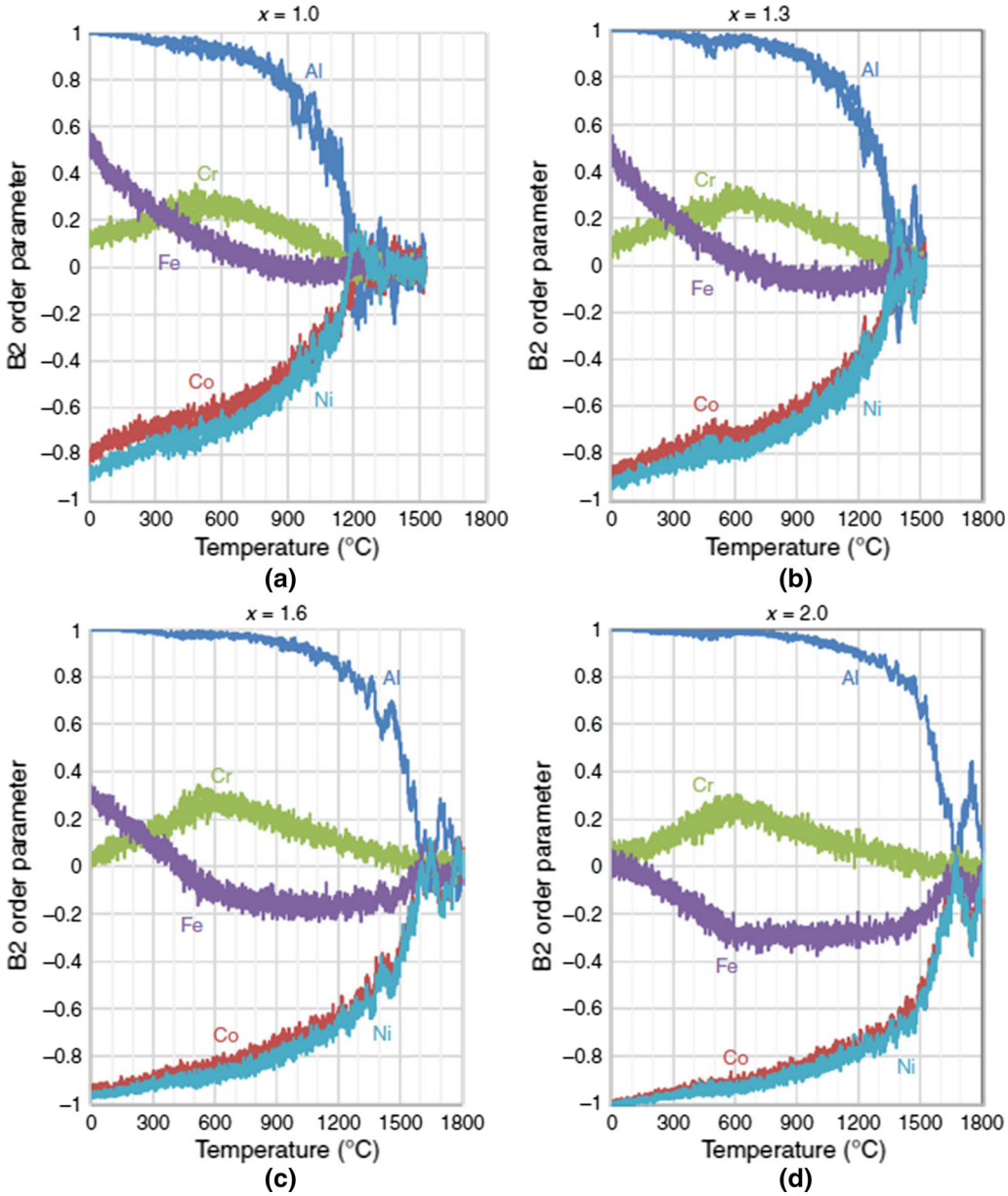

Fig. 59—Simulated configurational order. The element-specific B2-order parameters obtained from Monte Carlo simulations are plotted for the AlxCoCrFeNi family of alloys. A comparison of four different Al contents, (*a*) $x = 1.0$, (*b*) $x = 1.3$, (*c*) $x = 1.6$, and (*d*) $x = 2.0$.[226]

constituent elements. The effective interatomic distance of the *i*th element will be obtained, considering the atomic fraction, f_j, and change of the atomic volume of the *i*th element dissolving into the *j*th element, ΔV_{ij}, as exhibited in the following equation:

$$d_i^{\text{eff}} = \sum_j^n f_j \left(1 + \frac{\Delta V_{ij}}{V_i}\right)^{\frac{1}{3}} d_i \qquad [26]$$

where f_j is the atomic fraction of the *j*th element, V_i is the atomic volume, and d_i is the lattice constant of the *i*th element, and ΔV_{ij} is the atomic-volume change of the *i*th element dissolved into the *j*th element. With this mathematical approach, which quantifies the lattice distortion, the values of $\bar{u}^D$ were experimentally verified from the measured chemical compositions and lattice constants, substituting the atomic fractions, f_j, and average lattice constants, $\bar{d}$, into the Eqs. [24] and [25], which are obtained from the APT measurement and synchrotron X-ray/neutron-diffractions in previous sections. The obtained lattice distortion, $\bar{u}^D$ (0.2373 Å), for the NbTaTiV refractory HEA, applying these experimentally-measured values, is fairly close to the theoretically-calculated parameter (0.2344 Å). In order to quantitatively understand the local lattice distortion of the present NbTaTiV refractory HEA, the distribution of atomic distances in a relaxed 64-atom NbTaTiV SQS was analyzed and shown in Figure 60(a).[49] The interatomic distance of all *n*th nearest-neighboring (NN) pairs extends over a wide range, suggesting that

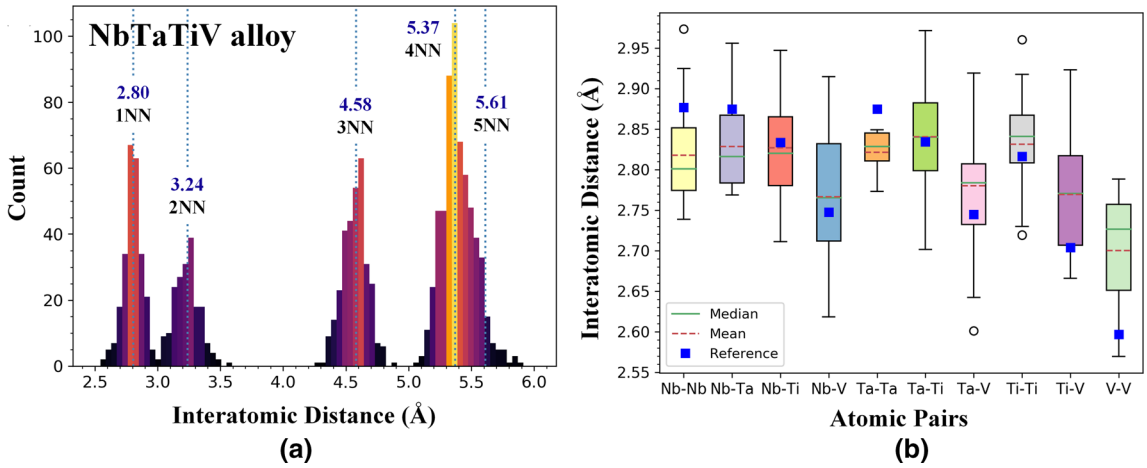

Fig. 60—First-principles calculations for NbTaTiV refractory HEA. (*a*) Distribution of the interatomic distances for the first to fifth nearest neighbors (NN) of the BCC NbTaTiV HEA calculated from the optimized SQS. (*b*) Box plot presenting the distribution of interatomic distances of 1NN bonds in the SQS for the BCC NbTaTiV HEA. The box shows the first and third quartile of the bond lengths for a type of atomic bonds. The reference bond lengths, calculated from comparable BCC structures for the homoatomic pairs and B2 structures for the heteroatomic pairs, are presented in blue squares (reproduced from Ref. [49] with permission).

many of the atoms deviate substantially from their ideal lattice sites. Thus, it leads to a severe local lattice distortion in this HEA. The average interatomic distances for the atomic pairs with and without considering the local atomic relaxation are $r = 2.80$, 3.23, 4.57, 5.42, and 6.47 Å and $r = 2.80$, 3.24, 4.58, 5.37, and 5.61 Å for the first to fifth NN pairs, respectively. It was found that the deviation in the average interatomic distances from an ideal BCC lattice for the 4NN and 5NN is noticeable. These results suggest that while the BCC lattice is maintained on average for the NbTaTiV HEA, a severe lattice distortion is predicted to be noticeable over longer ranges of atomic distances. Figure 60(b) presents the NN interatomic distance of the aforementioned pairs in the SQS after the structural optimization. The NbTaTiV HEA has ten different types of atomic pairs, *i.e.*, the homoatomic pairs of Nb-Nb, Ti-Ti, Ta-Ta, and V-V, and the heteroatomic pairs of Nb-Ti, Nb-Ta, Nb-V, Ti-Ta, Ti-V, and Ta-V. Additional DFT calculations were performed for the homoatomic and heteroatomic pairs with BCC and B2 crystal structures to obtain the reference bond length for the interatomic pairs. The mean and median of the interatomic distance of each pair are also shown in Figure 60(b). Considering both the range of the interatomic distance and the mean value of a pair, a large number of atoms in the SQS shift strongly away from their ideal lattice sites, indicating a severe local lattice distortion in the NbTaTiV HEA. The lattice distortions can be defined as the change of the bond length with respect to the reference bond length:

$$\text{Lattice distortion} = \frac{|d_i - d_r|}{d_r} \times 100 \qquad [27]$$

where d_i is the interatomic distance of a pair in the relaxed SQS, and d_r is the interatomic distance obtained for a pair with a BCC or B2 structure. Using this equation, the largest lattice distortion pairs are V-V and Ti-Ti, which are 4.7 and 5.1 pct, respectively. Among the heteroatomic pairs, the largest lattice distortions are the Nb-V and Ti-V pairs with a lattice distortion of 6.1 and 8.1 pct, respectively. In short, the dominant strengthening mechanism for the NbTaTiV refractory HEA was found to be solid-solution hardening, which originated from the lattice distortion. The distorted lattice of the NbTaTiV HEA was quantitatively determined by the experimental efforts and theoretical modeling, such as first-principles calculations. The results of the modeling and analysis suggest that the severe lattice distortions are induced, due to the atomic-size mismatch and local atomic interactions in the NbTaTiV refractory HEA.

G. *Additive Manufacturing in HEAs*

Recently, the additive manufacturing (AM) technique has attracted increasingly attention and has been applied in high-entropy alloys (HEAs), due to the better performances of properties, such as reduced defects, low cost, and high efficiency compared to typical casted alloys. Most previous research in HEAs have more focused on casted alloys and their microstructure tuning through secondary processing methods, such as cold rolling, forging, or annealing treatment.[232] However, it is a still large challenge to control the casting defects (shrinkages and pores) without the variation of phase formation and microstructures, which could strongly affect mechanical properties, through the secondary treatments. Compared with the conventional up–down fabrication method, the AM processing technique has been applied to the fabrication of three-dimensional (3D) printing, enables the fabrication of 3D objects based upon computer-aided design (CAD) models, which have been accepted as a transformative technology across multiple industries.[233,234] To keep up with the new trend of HEAs processing, Liaw's group and his colleagues have manufactured and studied the FCC-structured HEAs, using

the selective laser meting (SLM) technique.[235] First of all, the carbon-containing FeCoCrNi HEA was fabricated by SLM and have investigated the effect of processing parameters on microstructural evolution and mechanical properties of the present HEA.[236]

Figure 61 indicates the evolution of density in the $FeCoCrNiC_{0.05}$ HEA as a function of laser powers and scanning speeds during AM processing. It is found that the increase of the SLM scanning powers and the decrease of the scanning speeds lead to the increase of density. Especially, when the $FeCoCrNiC_{0.05}$ HEA manufactured using a low laser scanning speed about 800 mm/s, the near full density was achieved (above 99 pct). Figure 62 shows the microstructures of the top, middle, and bottom parts of the SLMed $FeCoCrNiC_{0.05}$ HEA, which was prepared under the laser power of 400 W and laser scanning speed of 800 mm/s. As illustrated in Figure 62(a) (an inverse pole figure of EBSD), the distribution of randomly-oriented grains is verified along the whole sample regions. The shape of grains is related to the thermal gradient and cooling rate. Figure 62(b) exhibits local misorientation maps, indicating the high level of local deformations. The large amount of low-angle grain boundaries and high density of dislocation also can be seen in grain boundaries maps (Figure 62(c)). These local deformations could lead to strain concentration and occurrence of microcracks.

With the investigation of microstructures of the SLMed $FeCoCrNiC_{0.05}$ HEA above, the mechanical properties of the present HEAs, which were manufactured by various scanning speeds and laser powers, are shown in Figure 63. The detailed parameters of mechanical properties are summarized in Figure 62. The engineering stress–strain curves data indicates that the yield strength of the SLMed $FeCoCrNiC_{0.05}$ is not strongly influenced by the manufacturing condition. However, the elongation shows notable changes with varying the processing condition. When the highest scanning speed of 1200 mm/s and laser power of 400 W were applied, the elongation (EL) was 7.7 pct. Sample 4 (400 W and 800 mm/s) exhibits a good ductility (13.5 pct). From the present work, we can conclude that the carbon-containing $FeCoCrNiC_{0.05}$ HEA with a full density can be successfully processed by SLM. The density of HEAs increases with the increasing scanning power and the decreasing scanning speed. With a full density, the grain size increases with increasing the scanning power and decreasing the scanning speed. The present HEAs of full density have a high tensile yield strength of 656 MPa. The ductility increases with the scanning power but decreases with the scanning speed.

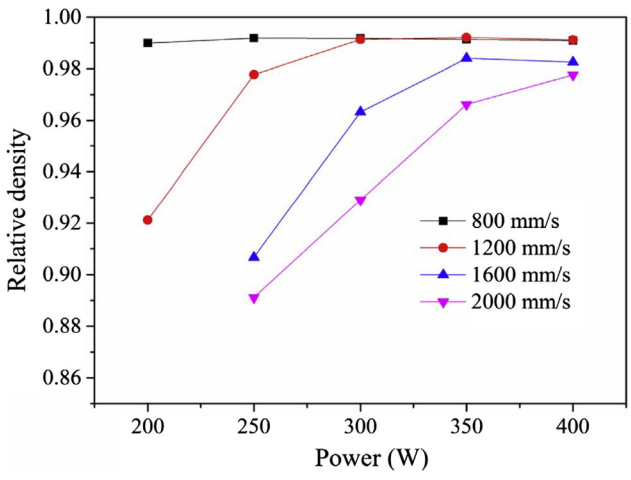

Fig. 61—Relative density of the SLMed $FeCoCrNiC_{0.05}$ HEA (reproduced from Ref. [236] with permission).

Based on the comprehensive investigation on microstructures and mechanical properties for the SLMed FeCoCrNi HEA above, Liaw's group and his colleagues have further manufactured the CoCrFeMnNi HEA, using a SLM technique with various scanning speeds and laser powers.[237] Figure 64 shows the microstructures of the SLMed CoCrFeMnNi HEA, which are obtained by optical microscopy, SEM, EBSD, and bright-field STEM. The typical hierarchical microstructure with semi-elliptical scan tracks of melt pools was observed from the SLMed sample (Figure 64(a)), which have been manufactured by a scanning speed of 2000 mm/s and laser power of 240 W. The SEM image in Figure 64(b) shows the formation of columnar grains along the building direction (BD), signalizing the epitaxial growth. Figure 64(c) reveals the formation of a cellular structure, which could be correlated with the solidification conditions. Furthermore, some nanovoids tend to distribute along cell walls. The EBSD IPF map along the BD in Figure 64(d) indicates that many grains tend to grow along the preferred growth direction of ⟨001⟩ during the solidification process. The EBSD image quality (IQ) map in Figure 64(e) exhibits that the as-built sample contained a high fraction of low-angle grain boundaries, whereas the Kernel average misorientation (KAM) map (Figure 64(f)) delineates local misorientations on the order of 0.2 deg to 0.9 deg across grains. The nano-scaled structures of the SLMed CoCrFeMnNi HEA were further investigated by a bright-field STEM technique, as illustrated in Figures 64(g) and (h). A typical sub-micron cellular structure with an average size of 0.34 μm was observed. Moreover, the cell walls are decorated with a high density of dislocations. The inset corresponding selected area electron diffraction (SAED) pattern in Figure 64(g) exhibits small misorientation among the cells. The homogenized elemental distribution was confirmed from the EDS analysis, which is associated with the area of Figure 64(h), since the fast-cooling process could suppress the chemical segregation.[238]

After the heat treatment, as shown in Figure 65, the cellular structure almost disappears and indicates a much lower dislocation density, which could imply the thermodynamically-metastable nature of the cellular structure. The existence of a small amount of dislocation may be due to the low heat-treatment temperature or short annealing time. With the investigation of microstructures of the SLMed CoCrFeMnNi HEA above, the mechanical properties of the present HEAs, which are manufactured by various scanning speeds and heat treatments, are shown in Figure 66. The as-built

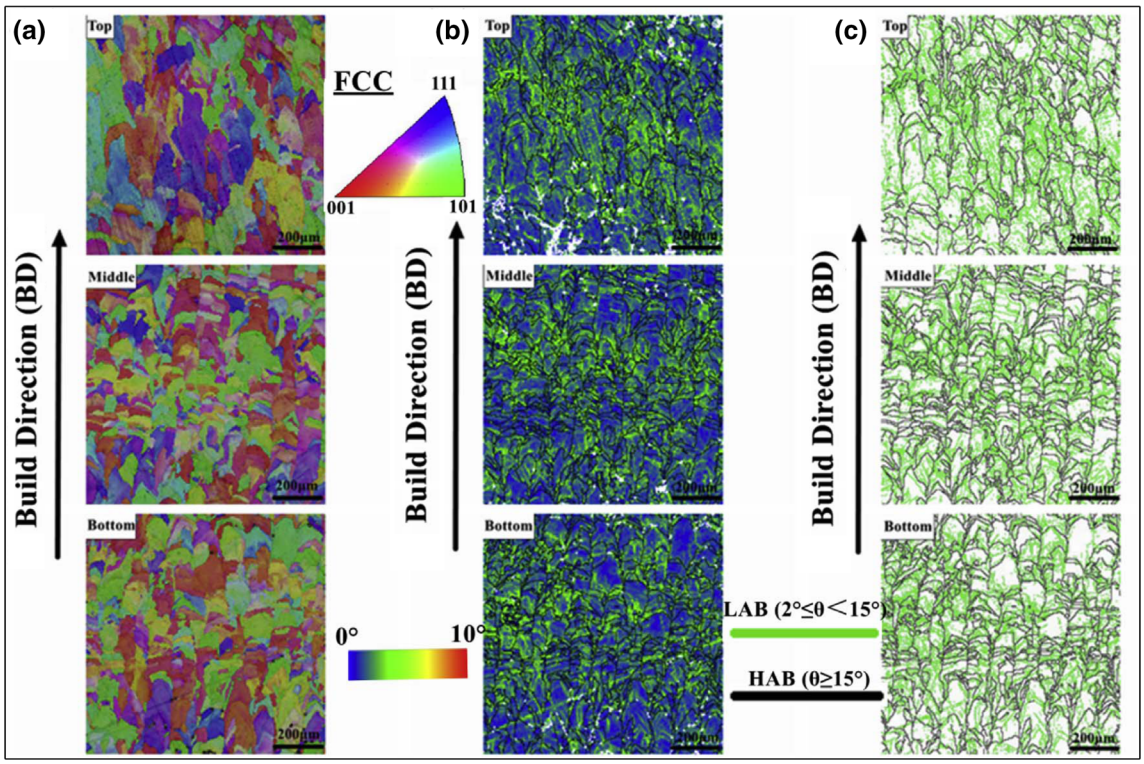

Fig. 62—EBSD analyses of the SLMed $FeCoCrNiC_{0.05}$ HEA (400 W, 800 mm/s) (*a*) IPF, (*b*) Local misorientation (LM) maps, (*c*) Grain boundaries (GB) maps of the $FeCoCrNiC_{0.05}$ HEA (reproduced from Ref. [236] with permission).

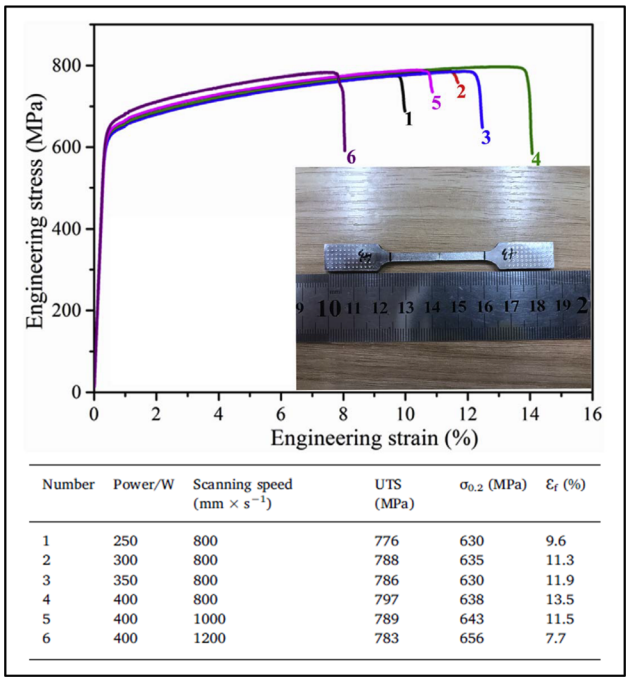

Number	Power/W	Scanning speed (mm × s^{-1})	UTS (MPa)	$\sigma_{0.2}$ (MPa)	ε_f (%)
1	250	800	776	630	9.6
2	300	800	788	635	11.3
3	350	800	786	630	11.9
4	400	800	797	638	13.5
5	400	1000	789	643	11.5
6	400	1200	783	656	7.7

Fig. 63—Room-temperature tensile strain-stress curves for $FeCoCrNiC_{0.05}$ alloys (The numbers corresponded to the insert table) (reproduced from Ref. [236] with permission).

V2000 HEA, which has been manufactured by the scanning speed of 2000 mm/s and laser power of 240 W, indicates an excellent combination of strength and ductility, comparable to the as recrystallized and as-cast CoCrFeNiMn sample.[239] The yield strength of the as-built V2000 possesses a nearly-doubles value, compared with the as recrystallized counterparts. After the heat treatment, although the yield strength decreases due to the recovery of the cell structures, the ductility increases. For the V2500 HEA, which has been manufactured by a scanning speed of 2500 mm/s and laser power of 240 W, the decrease of ductility may be due to the existence of pores, which could act as critical sites for stress concentration.[240]

In order to understand the deformation mechanisms of the as-built samples, the microstructures of the as-built V2000 strained to fracture were examined, using EBSD and STEM, as presented in Figure 67. The plastic deformation is mainly accommodated by dislocation motions, as illustrated in Fig 67(a). According to a recent investigation,[28] the critical stress for initiating deformation twins in this HEA is 720 ± 30MPa. However, the KAM map related with the geometrically necessary dislocations in Figure 67(b) exhibits a local misorientation up to 1.6 deg, demonstrating the dominance of the dislocation-mediated plasticity during deformation. The bright-field STEM image in

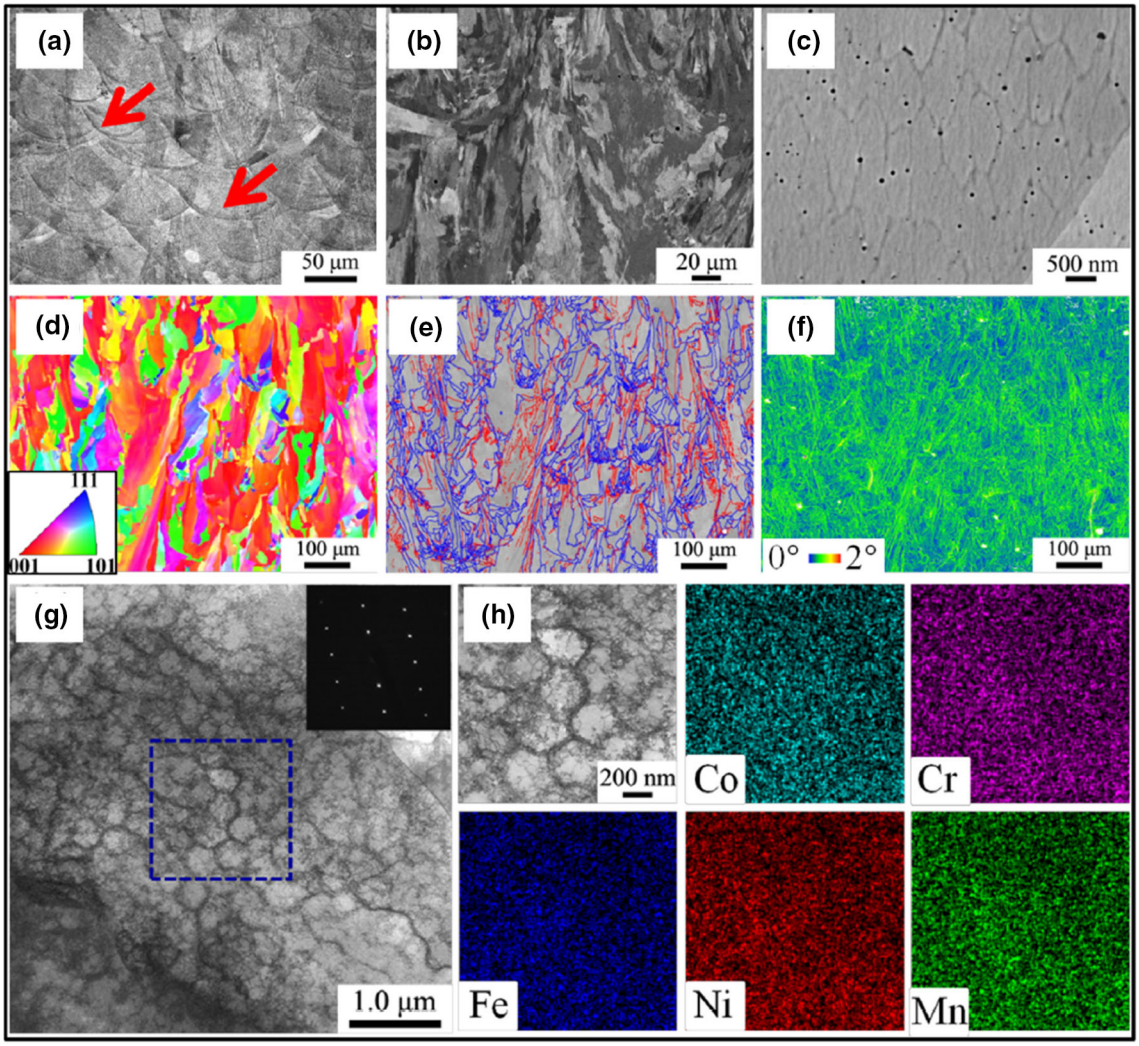

Fig. 64—(*a*) OM and (*b*) SEM images of the front surface. (*c*) SEM image of the cellular structure. (*d*) The EBSD IPFs of the front surface. (*e*) EBSD IQ map with high-angle GBs (blue lines) and low angle GBs (red lines) superimposed. (*f*) KAM image of the front surface. (*g*) Bright-field STEM image of the cellular structure with the corresponding SAED pattern. (*h*) Bright-field STEM image of the selected area illustrated by a square in (*g*) and the elemental-distribution maps of the area for the SLMed CoCrFeMnNi HEA (reproduced from Ref. [237] with permission).

Figure 67(c) suggests a remarkable dislocation trapping and retention mechanism within the cells, leading to an apparent increase of the dislocation density inside the cell walls. Another fingerprint of dislocation substructures is the planar slip bands, as shown in Figure 67(d). These slip bands significantly interact with cellular structures to form a three-dimensional dislocation network.

IV. FUTURE TRENDS AND PROSPECTS

Although some research has been done by Liaw's group and his colleagues regarding the fundamental study and design of new metallic alloys, microstructural investigations, deformation behaviors, and mechanisms in BMGs and HEAs, there is still plenty to investigate. For example, future investigations could involve the modeling and analysis of the serrated flow behavior in BMGs and HEAs using techniques, such as the detrended fluctuation analysis[241] and complexity algorithms. Moreover, theoretical models involving finite-element methods, machine-learning algorithms, and molecular dynamics could be used to thoroughly investigate the effects of composition, temperature, and strain rate on the serrated flow dynamics in BMGs. Advanced microstructural-characterization techniques, such as high energy *in-situ* XRD and ND could be coupled with the results of the modeling and analysis to gain foundational insight regarding the interplay between the deformation behavior and microstructures of BMGs during the serrated flow.

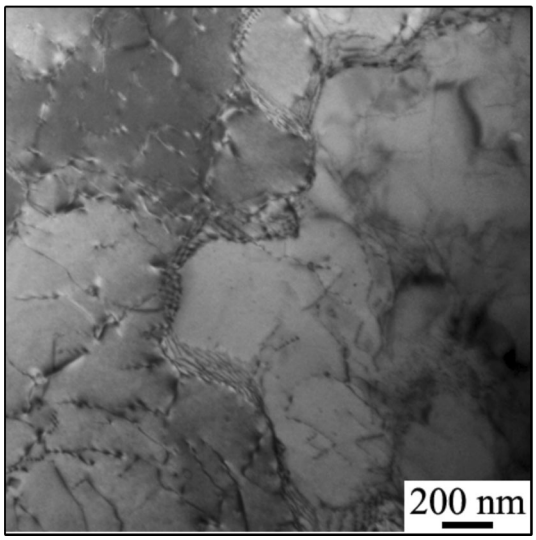

Fig. 65—Bright-field STEM image of the as-built CoCrFeMnNi after the heat treatment (reproduced from Ref. [237] with permission).

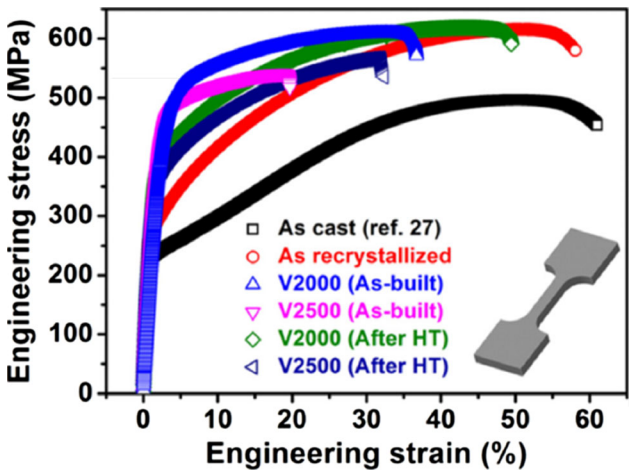

Fig. 66—The engineering stress–strain curves of the as-built CoCrFeMnNi samples with different conditions (reproduced from Ref. [237] with permission).

Moreover, future investigations could examine how the combinations of temperature and irradiation dose affects the serrated flow dynamics in BMGs and HEAs. One example of such future studies could involve the nanopillar compression of ion-irradiated BMGs. Here, ions would bombard the sample with energies high enough such that the ions would be implanted beyond the region of interest, which will ensure a uniform damage profile. During the experiment of BMGs, samples would be exposed to temperatures well below the glass-transition temperatures of the alloys to avoid thermally-induced crystallization during irradiation. The serration behavior of the pillars subjected to compression would be analyzed, using the complexity and the MFT analysis. Such studies would be extremely important as it would assess how irradiation-induced rejuvenation and thermal relaxation could affect the serration dynamics in BMGs. Another important experiment could involve analyzing the serrated flow of neutron-irradiated BMG and HEA samples subjected to compression testing at different strain rates and test temperatures.

In addition to the serrated flow behavior, there should be future studies regarding the bio applications of BMGs and HEAs, such as implant materials. These investigations could involve the fatigue behavior of BMGs in environments typical of joint environments. The microstructure evolution during mechanical testing could be examined *via in-situ* ND or TEM. Furthermore, the fatigue behavior could be modeled and analyzed, using statistical models. The results of the microstructural and mechanical behavior characterization could then be coupled to help gain a more fundamental understanding as to the potential of BMGs and HEAs for implant applications.

Furthermore, high-throughput CALPHAD modeling and machine learning techniques, coupled with first-principles calculations and molecular-dynamics simulations, could be applied to efficiently design new HEA compositions. The designed HEAs also could be fabricated by new technologies, such as additive manufacturing. Based on the study of microstructural investigations and mechanical behaviors in HEAs from Liaw's group and his colleagues, we could extend the range of applications by studying the thermoelectric, magnetic, electrochemical, and bio-properties of a wide range of HEAs. In the meantime, theoretical modeling, such as machine learning, quantum mechanical modeling, classical interatomic potentials, and molecular-to-mesoscale modeling, should be developed to further verify the detailed mechanical mechanisms of HEAs. Figure 68 illustrates the example world-wide collaborations with Liaw's group. These extensive collaborations with various Universities and National Laboratories will accelerate the development of new structural materials, including BMGs and HEAs.

Above all, it is critical to design and develop BMGs and HEAs with desirable properties for many industrial applications through fundamental research activities.

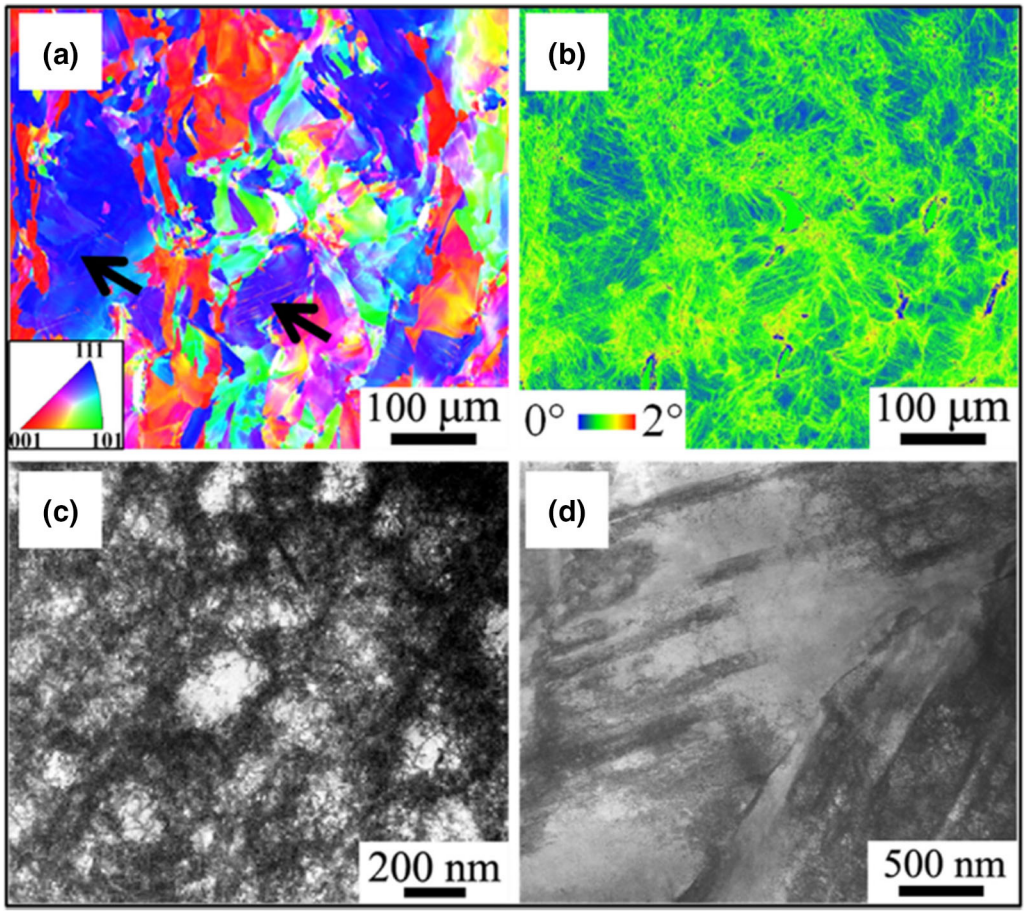

Fig. 67—(*a*) EBSD IPF, (*b*) KAM map, and (*c and d*) Bright-field STEM images of an as-built CoCrFeMnNi sample strained to fracture. The arrows show the deformation twins (reproduced from Ref. [237] with permission).

V. CONCLUSIONS

In conclusion, this paper covered the past and more recent investigative work being undertaken by Liaw's research group and his colleagues regarding BMG and HEA materials. In terms of the former, the present work includes the study of shear-banding dynamics and the modeling and analysis of the serrated plastic flow. As for HEAs, his group has been active in the design of HEAs using state-of-the-art experimental and computational approaches. Furthermore, Liaw's group and his colleagues have performed the fundamental work regarding the mechanical and microstructural behavior of HEAs, using advanced *ex-situ* and *in-situ* characterization techniques, such as thermography, neutron and synchrotron diffraction. Especially, his group and his colleagues have focused on various HEAs, such as Al-containing HEAs, lightweight HEAs, and refractory HEAs, aiming to extend the range of applications. Moreover, possible future directions of research have also been discussed, such as using additive manufacturing techniques to produce designed HEAs and combining modeling and analysis methods with advanced *in situ* characterization techniques to gain a more fundamental understanding of the serrated plastic flow phenomenon, mechanical and phase-transformation behavior in BMGs and HEAs. It is our hope that with our continual fundamental research on BMGs and HEAs, the materials with desirable properties can be designed and developed for many industrial applications.

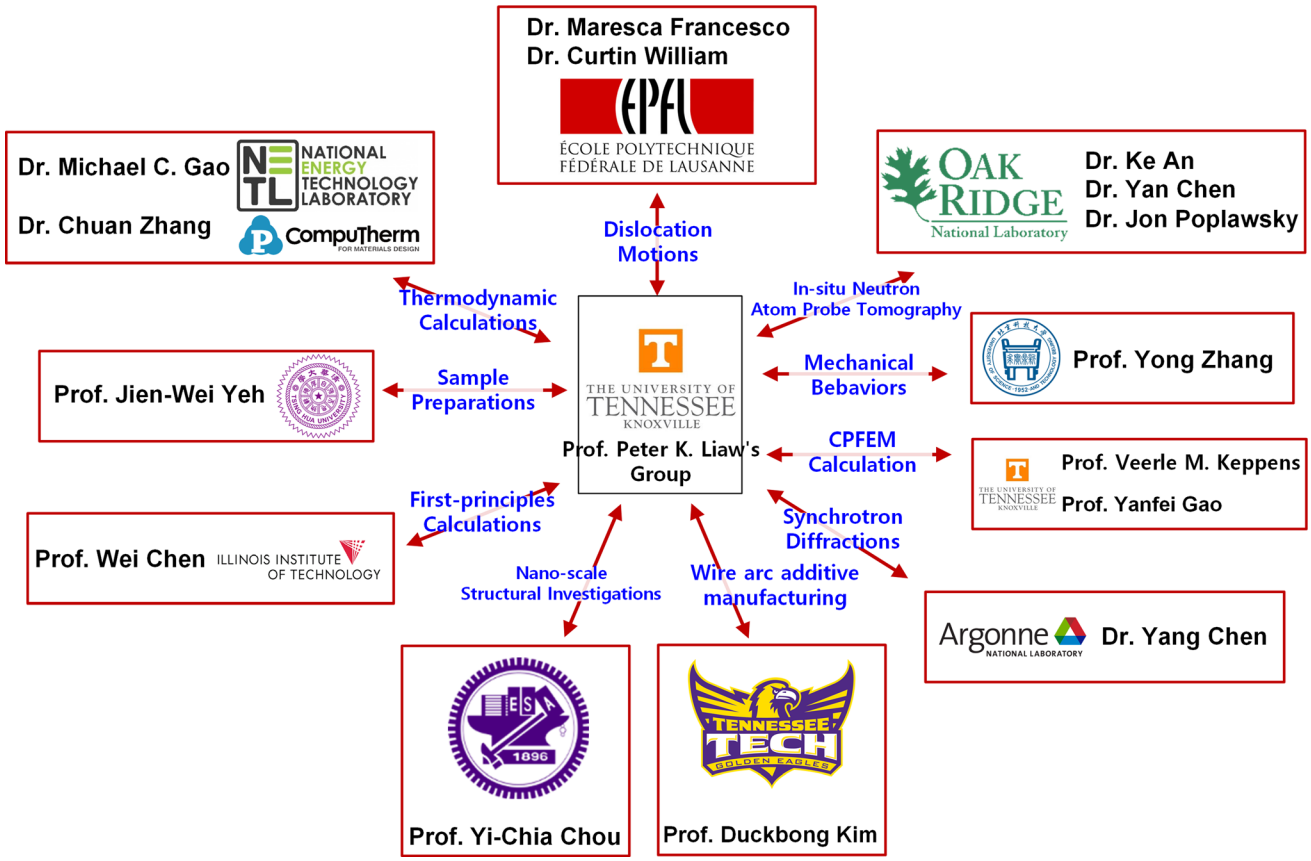

Fig. 68—Example world-wide collaborations map with Liaw's group. We apologize for not being able to include all our colleagues.

ACKNOWLEDGMENTS

The authors very much appreciate the support from the U.S. Army Office Project (Grant Nos. W911NF-13-1-0438 and W911NF-19-2-0049) with the program managers, Drs. Michael P. Bakas, David M. Stepp, and Suveen Mathaudhu. Peter K. Liaw also thanks the support from the National Science Foundation (Grant Nos. DMR-1611180 and 1809640) with the program directors, Drs. Judith Yang, Gary Shiflet, and Diana Farkas.

REFERENCES

1. W. Klement, R.H. Willens, and P.O.L. Duwez: *Nature*, 1960, vol. 187, pp. 869–70.
2. N. Mattern: *J. Non-Crystalline Solids*, 2007, vol. 353, pp. 1723–31.
3. H.S. Chen: *Acta Metall.*, 1974, vol. 22, pp. 1505–11.
4. M. Miller and P. K. Liaw, (Springer: New York, 2008).
5. A. Peker and W.L. Johnson: *Appl. Phys. Lett.*, 1993, vol. 63, pp. 2342–44.
6. A. Inoue: *Acta Mater.*, 2000, vol. 48, pp. 279–06.
7. A. LindsayGreer: *Nature*, 1993, vol. 366, pp. 303–04.
8. A. Inoue, B. Shen, and N. Nishiyama: *Bulk Metallic Glasses*, Springer, New York, 2008.
9. J. Plummer and W.L. Johnson: *Nat. Mater.*, 2015, vol. 14, pp. 553–55.
10. J. Brechtl, S. Agarwal, M.L. Crespillo, J. Salasin, T. Yang, H. Bei, and S.J. Zinkle: *Intermetallics*, 2020, vol. 116, art. no. 106655.
11. S.J. Pang, T. Zhang, K. Asami, and A. Inoue: *Corros. Sci.*, 2002, vol. 44, pp. 1847–56.
12. L. Huang, D.C. Qiao, B.A. Green, P.K. Liaw, J.F. Wang, S.J. Pang, and T. Zhang: *Intermetallics*, 2009, vol. 17, pp. 195–99.
13. W.H. Peter, R.A. Buchanan, C.T. Liu, P.K. Liaw, M.L. Morrison, C.A. Carmichael, and J.L. Wright: *Intermetallics*, 2002, vol. 10, pp. 1157–62.
14. S.V. Madge, A. Caron, R. Gralla, G. Wilde, and S.K. Mishra: *Intermetallics*, 2014, vol. 47, pp. 6–10.
15. M.N.M. Patnaik, R. Narasimhan, and U. Ramamurty: *Acta Mater.*, 2004, vol. 52, pp. 3335–45.
16. F.F. Wu, K.C. Chan, S.S. Jiang, S.H. Chen, and G. Wang: *Sci. Rep.*, 2014, vol. 4, art. no. 5302.
17. X. Gu, G.J. Shiflet, F.Q. Guo, and S.J. Poon: *J. Mater. Res.*, 2005, vol. 20, pp. 1935–38.
18. N. Hua, Z. Liao, Q. Wang, L. Zhang, Y. Ye, J. Brechtl, and P.K. Liaw: *J. Non-Cryst. Solids*, 2020, vol. 529, art. no. 119782.
19. J. Brechtl, S. Agarwal, M.L. Crespillo, T. Yang, H. Bei, and S.J. Zinkle: *J. Nucl. Mater.*, 2019, vol. 523, pp. 299–309.
20. G.Y. Wang, P.K. Liaw, and M.L. Morrison: *Intermetallics*, 2009, vol. 17, pp. 579–90.
21. G.Y. Wang, M.D. Demetriou, J.P. Schramm, P.K. Liaw, and W.L. Johnson: *J. Appl. Phys.*, 2010, vol. 108, art. no. 023505023505.
22. G.Y. Wang, P.K. Liaw, Y. Yokoyama, A. Peker, W.H. Peter, B. Yang, M. Freels, Z.Y. Zhang, V. Keppens, R. Hermann, R.A. Buchanan, C.T. Liu, and C.R. Brooks: *Intermetallics*, 2007, vol. 15, pp. 663–67.
23. G.Y. Wang, P.K. Liaw, Y. Yokoyama, A. Inoue, and C.T. Liu: *Mater. Sci. Eng. A*, 2008, vol. 494, pp. 314–23.
24. A. Inoue, T. Zhang, W. Zhang, and A. Takeuchi: *Mater. Trans. JIM*, 1996, vol. 37, pp. 99–108.
25. A. Inoue, H. Koshiba, T. Itoi, and A. Makino: *Appl. Phys. Lett.*, 1998, vol. 73, pp. 744–46.
26. A. Inoue: *Mater. Sci. Eng. A*, 2001, vol. 304, pp. 1–10.

27. C.J. Gilbert, R.O. Ritchie, and W.L. Johnson: *Appl. Phys. Lett.*, 1997, vol. 71, pp. 476–78.
28. C.J. Gilbert, V. Schroeder, and R.O. Ritchie: *Metall. Mater. Trans. A*, 1999, vol. 30A, pp. 1739–53.
29. P. Lowhaphandu and J.J. Lewandowski: *Scr. Mater.*, 1998, vol. 38, pp. 1811–17.
30. J.H. Schneibel, J.A. Horton, and P.R. Munroe: *Metall. Mater. Trans. A*, 2001, vol. 32A, pp. 2819–25.
31. Y. Zhang, Y.J. Zhou, J.P. Lin, G.L. Chen, and P.K. Liaw: *Adv. Eng. Mater.*, 2008, vol. 10, pp. 534–38.
32. W.H. Peter, P.K. Liaw, R.A. Buchanan, C.T. Liu, C.R. Brooks, J.A. Horton, C.A. Carmichael, and J.L. Wright: *Intermetallics*, 2002, vol. 10, pp. 1125–29.
33. M. Freels, P.K. Liaw, G.Y. Wang, Q.S. Zhang, and Z.Q. Hu: *J. Mater. Res.*, 2007, vol. 22, pp. 374–81.
34. D.C. Qiao, G.J. Fan, P.K. Liaw, and H. Choo: *Int. J. Fatigue*, 2007, vol. 29, pp. 2149–54.
35. G.J. Fan, H.H. Liao, H. Choo, P.K. Liaw, N. Mara, A.V. Sergueeva, A.K. Mukherjee, and E.J. Lavernia: *Metall. Mater. Trans. A*, 2007, vol. 38A, pp. 2001–2005.
36. W.Z. Liang, J. Shen, J.F. Sun, L.Z. Wu, and P.K. Liaw: *Mater. Sci. Eng. A*, 2008, vol. 497, pp. 378–82.
37. X.L. Bian, G. Wang, H.C. Chen, L. Yan, J.G. Wang, Q. Wang, P.F. Hu, J.L. Ren, K.C. Chan, N. Zheng, A. Teresiak, Y.L. Gao, Q.J. Zhai, J. Eckert, J. Beadsworth, K.A. Dahmen, and P.K. Liaw: *Acta Mater.*, 2016, vol. 106, pp. 66–77.
38. W. Dmowski, C. Fan, M.L. Morrison, P.K. Liaw, and T. Egami: *Mater. Sci. Eng. A*, 2007, vol. 471, pp. 125–29.
39. J. Brechtl, X. Xie, Z. Wang, J. Qiao, and P.K. Liaw: *Mater. Sci. Eng. A*, 2020, vol. 771, art. no. 138585.
40. J. Brechtl, Z. Wang, X. Xie, J.-W. Qiao, and P.K. Liaw: *Appl. Sci.*, 2020, vol. 10, art. no. 3892.
41. X. Xie, Y.-C. Lo, Y. Tong, J. Qiao, G. Wang, S. Ogata, H. Qi, K.A. Dahmen, Y. Gao, and P.K. Liaw: *J. Mech. Phys. Solids*, 2019, vol. 124, pp. 634–42.
42. O.N. Senkov, G.B. Wilks, D.B. Miracle, C.P. Chuang, and P.K. Liaw: *Intermetallics*, 2010, vol. 18, pp. 1758–65.
43. Y. Zhang, T.T. Zuo, Z. Tang, M.C. Gao, K.A. Dahmen, P.K. Liaw, and Z.P. Lu: *Progr. Mater. Sci.*, 2014, vol. 61, pp. 1–93.
44. R. Feng, M.C. Gao, C. Lee, M. Mathes, T. Zuo, S. Chen, J.A. Hawk, Y. Zhang, and P.K. Liaw: *Entropy*, 2016, vol. 18, art. no. 333.
45. R. Feng, M.C. Gao, C. Zhang, W. Guo, J.D. Poplawsky, F. Zhang, J.A. Hawk, J.C. Neuefeind, Y. Ren, and P.K. Liaw: *Acta Materialia*, 2018, vol. 146, pp. 280–93.
46. H. Diao, D. Ma, R. Feng, T. Liu, P. Chao, C. Zhang, W. Guo *et al.*: *Mater. Sci. Eng. A*, 2019, vol. 742, pp. 636–47.
47. L.J. Santodonato, Y. Zhang, M. Feygenson, C.M. Parish, M.C. Gao, R.J. Weber, J.C. Neuefeind, Z. Tang, and P.K. Liaw: *Nat. Commun.*, 2015, vol. 6, art. no. 5964.
48. J.C. Rao, H.Y. Diao, V. Ocelík, D. Vainchtein, C. Zhang, C. Kuo, Z. Tang, W. Guo, J.D. Poplawsky, Y. Zhou *et al.*: *Acta Mater.*, 2017, vol. 131, pp. 206–220.
49. C. Lee, G. Song, M.C. Gao, R. Feng, P. Chen, J. Brechtl, Y. Chen, K. An, W. Guo, J.D. Poplawsky, and S. Li: *Acta Materialia*, 2018, vol. 160, pp. 158–72.
50. G. Kim, H. Diao, C. Lee, A.T. Samaei, T. Phan, M. de Jong, K. An, D. Ma, P.K. Liaw, and W. Chen: *Acta Materialia*, 2019, vol. 181, pp. 124–38.
51. C. Lee, G. Kim, Y. Chou, B.L. Musicó, M.C. Gao, K. An, G. Song, Y.C. Chou, V. Keppens, W. Chen, and P.K. Liaw: *Sci. Adv.*, 2020, vol. 6, p. 4748.
52. M.A. Hemphill, T. Yuan, G.Y. Wang, J.W. Yeh, C.W. Tsai, A. Chuang, and P.K. Liaw: *Acta Materialia*, 2012, vol. 60, pp. 5723–5734.
53. Z. Tang, T. Yuan, C.-W. Tsai, J.-W. Yeh *et al.*: *Acta Mater.*, 2015, vol. 99, pp. 247–58.
54. Y. Shi, B. Yang, X. Xie, J. Brechtl *et al.*: *Corros. Sci.*, 2017, vol. 119, pp. 33–45.
55. Y. Shi, L. Collins, R. Feng, C. Zhang, N. Balke *et al.*: *Corros. Sci.*, 2018, vol. 133, pp. 120–31.
56. Y. Shi, B. Yang, and P. Liaw: *Metals*, 2017, vol. 7, art. no. 43.
57. M.C. Gao, J.W. Yeh, P.K. Liaw, and Y. Zhang: *High-Entropy Alloys: Fundamentals and Applications*, Springer International Publishing, New York, 2016.
58. B. Cantor, I.T.H. Chang, P. Knight, and A.J.B. Vincent: *Mater. Sci. Eng. A*, 2004, vol. 375, pp. 213–18.
59. J.-W. Yeh, S.-K. Chen, S.-J. Lin, J.-Y. Gan, T.-S. Chin, T.-T. Shun, C.-H. Tsau, and S.-Y. Chang: *Adv. Eng. Mater.*, 2004, vol. 6, pp. 299–303.
60. D.B. Miracle and O.N. Senkov: *Acta Mater.*, 2017, vol. 122, pp. 448–11.
61. O.N. Senkov, G.B. Wilks, J.M. Scott, and D.B. Miracle: *Intermetallics*, 2011, vol. 19, pp. 698–706.
62. O.N. Senkov, J.M. Scott, S.V. Senkova, F. Meisenkothen, D.B. Miracle, and C.F. Woodward: *JMatS*, 2012, vol. 47, pp. 4062–74.
63. O.N. Senkov, J.M. Scott, S.V. Senkova, D.B. Miracle, and C.F. Woodward: *J. Alloy. Compd.*, 2011, vol. 509, pp. 6043–48.
64. K.M. Youssef, A.J. Zaddach, C. Niu, D.L. Irving, and C.C. Koch: *Mater. Res. Lett.*, 2015, vol. 3, pp. 95–99.
65. M.C. Gao, B. Zhang, S.M. Guo, J.W. Qiao, and J.A. Hawk: *MMTA*, 2016, vol. 47, pp. 3322–3332.
66. H.Y. Diao, R. Feng, K.A. Dahmen and P.K. Liaw, *Curr. Opin. Solid State Mater. Sci.* 2017.
67. W. Zhenggang, H. Bei, F. Otto *et al.*: *Intermetallics*, 2014, vol. 46, pp. 131–40.
68. Y. Wu, W.H. Liu, X.L. Wang, D. Ma, A.D. Stoica, T.G. Nieh, Z.B. He, and Z.P. Lu: *Appl. Phys. Lett.*, 2014, vol. 104, art. no. 051910.
69. B. Gludovatz, A. Hohenwarter, D. Catoor, E.H. Chang, E.P. George, and R.O. Ritchie: *Science*, 2014, vol. 345, pp. 1153–58.
70. M.S. Lucas, G.B. Wilks, L. Mauger *et al.*: *Appl. Phys. Lett.*, 2012, vol. 100, art. no. 251907.
71. T.-T. Shun and D. Yu-Chin: *J. Alloy. Compd.*, 2009, vol. 479, pp. 157–60.
72. S. Guo *et al.*: *J. Alloy. Compd.*, 2013, vol. 557, pp. 77–81.
73. Y. Dong, L. Yiping, J. Kong, J. Zhang, and T. Li: *J. Alloy. Compd.*, 2013, vol. 573, pp. 96–101.
74. Y. Dong, K. Zhou, L. Yiping, X. Gao, T. Wang, and T. Li: *Mater. Des.*, 2014, vol. 57, pp. 67–72.
75. B.S. Li, Y.P. Wang, M.X. Ren, C. Yang, and H.Z. Fu: *Mater. Sci. Eng. A*, 2008, vol. 498, pp. 482–86.
76. Y. Zou, S. Maiti, W. Steurer, and R. Spolenak: *Acta Mater.*, 2014, vol. 65, pp. 85–97.
77. M.C. Gao, C.S. Carney, Ö.N. Doğan, P.D. Jablonksi, J.A. Hawk, and D.E. Alman: *JOM*, 2015, vol. 67, pp. 2653–69.
78. H.W. Yao, J.W. Qiao, J.A. Hawk, H.F. Zhou, M.W. Chen, and M.C. Gao: *J. Alloy. Compd.*, 2017, vol. 696, pp. 1139–50.
79. S. Fang, X. Xiao, L. Xia, W. Li, and Y. Dong: *J. Non-Cryst. Solids*, 2003, vol. 321, pp. 120–25.
80. F. Spaepen: *Acta Metall.*, 1977, vol. 25, pp. 407–15.
81. Q. Hu, X.-R. Zeng, and M.W. Fu: *J. Appl. Phys.*, 2011, vol. 109, art. no. 053520.
82. A. Van Den Beukel and S. Radelaar: *Acta Metall.*, 1983, vol. 31, pp. 419–27.
83. P. Wen, M.B. Tang, M.X. Pan, Z. Zhang, and W.H. Wang: *Phys. Rev. B*, 2003, vol. 67, art. no. 212201.
84. J. Brechtl, H. Wang, N.A.P.K. Kumar, T. Yang, Y.R. Lin, H. Bei, J. Neuefeind, W. Dmowski, and S.J. Zinkle: *J. Nucl. Mater.*, 2019, vol. 526, art. no. 151771.
85. A. van den Beukel and J. Sietsma: *Acta Metall. Mater.*, 1990, vol. 38, pp. 383–89.
86. X.X. Yue, A. Inoue, C.T. Liu, and C. Fan: *Mater. Re.-Ibero-Am. J. Mater.*, 2017, vol. 20, pp. 326–38.
87. Y. Huang, Y. Sun, and J. Shen: *Intermetallics*, 2010, vol. 18, pp. 2044–50.
88. G. Z. Voyiadjis, L. Malekmotiei and A. Samadi-Dooki, In *Handbook of Nonlocal Continuum Mechanics for Materials and Structures*, ed. George Z. Voyiadjis (Springer International Publishing: Cham, 2017), pp. 1–27.
89. A.S. Argon: *Acta Metall.*, 1979, vol. 27, pp. 47–58.
90. A.J. Foreman, M.A. Jaswon, and J.K. Wood: *Proc. Phys. Soc. Lond. A*, 1951, vol. 64, pp. 156–63.
91. J.S. Langer: *Scripta Mater.*, 2006, vol. 54, pp. 375–79.

92. K. Kosiba, S. Scudino, J. Bednarcik, J. Bian, G. Liu, U. Kuhn, and S. Pauly: *Phys. Rev. B*, 2020, vol. 102, art. no. 8.
93. S.X. Song and T.G. Nieh: *Intermetallics*, 2011, vol. 19, pp. 1968–77.
94. M. Jafary-Zadeh, G. Praveen Kumar, P.S. Branicio, M. Seifi, J.J. Lewandowski, and F. Cui: *J. Funct. Biomater.*, 2018, vol. 9, art. no. 19.
95. C.A. Schuh, T.C. Hufnagel, and U. Ramamurty: *Acta Mater.*, 2007, vol. 55, pp. 4067–4109.
96. J. Brechtl, S. Chen, C. Lee, Y. Shi, R. Feng, X. Xie, D. Hamblin, A.M. Coleman, B. Straka, H. Shortt, and R.J. Spurling: *Metals*, 2020, vol. 10, art. no. 1101.
97. S.V. Madge: *Metals*, 2015, vol. 5, pp. 1279–1305.
98. J. Antonaglia, X. Xie, G. Schwarz, M. Wraith, J. Qiao, Y. Zhang, P.K. Liaw, J.T. Uhl, and K.A. Dahmen: *Sci. Rep.*, 2014, vol. 4, art. no. 4382.
99. H. Chen, Y. He, G.J. Shiflet, and S.J. Poon: *Nature*, 1994, vol. 367, pp. 541–43.
100. W.H. Jiang, F.E. Pinkerton, and M. Atzmon: *Scripta Mater.*, 2003, vol. 48, pp. 1195–1200.
101. J. Li, X. Gu, and T.C. Hufnagel: *Microsc. Microanal.*, 2003, vol. 9, pp. 509–15.
102. J. Li, F. Spaepen, and T.C. Hufnagel: *Philos. Mag. A*, 2002, vol. 82, pp. 2623–30.
103. Y. Hirotsu, T.G. Nieh, A. Hirata, T. Ohkubo, and N. Tanaka: *Phys. Rev. B*, 2006, vol. 73, art. no. 4.
104. P.E. Donovan and W.M. Stobbs: *Acta Metall.*, 1981, vol. 29, pp. 1419–36.
105. S.V. Ketov and D.V. Louzguine-Luzgin: *Scientific Reports*, 2013, vol. 3, art. no. 2798.
106. Y. Zhang, N.A. Stelmashenko, Z.H. Barber, W.H. Wang, J.J. Lewandowski, and A.L. Greer: *J. Mater. Res.*, 2007, vol. 22, pp. 419–27.
107. J.J. Lewandowski and A.L. Greer: *Nat. Mater.*, 2006, vol. 5, pp. 15–18.
108. B. Yang, M.L. Morrison, P.K. Liaw, R.A. Buchanan, G.Y. Wang, C.T. Liu, and M. Denda: *Appl. Phys. Lett.*, 2005, vol. 86, art. no. 3.
109. J. Brechtl, S.Y. Chen, X. Xie, Y. Ren, J.W. Qiao, P.K. Liaw, and S.J. Zinkle: *Int. J. Plast*, 2019, vol. 115, pp. 71–92.
110. M. Abbadi, P. Hahner, and A. Zeghloul: *Mater. Sci. Eng. A.*, 2002, vol. 337, pp. 194–201.
111. J. Antonaglia, W.J. Wright, X. Gu, R.R. Byer, T.C. Hufnagel, M. LeBlanc, J.T. Uhl, and K.A. Dahmen: *Phys. Rev. Lett.*, 2014, vol. 112, pp. 1–5.
112. J.J. Li, Z. Wang, and J.W. Qiao: *Mater. Des.*, 2016, vol. 99, pp. 427–32.
113. F.H.D. Torre, D. Klaumünzer, R. Maaß, and J.F. Löffler: *Acta Mater.*, 2010, vol. 58, pp. 3742–50.
114. R. Maaß, D. Klaumünzer, and J.F. Löffler: *Acta Mater.*, 2011, vol. 59, pp. 3205–13.
115. B. Shi, S.Y. Luan, and P.P. Jin: *J. Non-Cryst. Solids*, 2018, vol. 482, pp. 126–31.
116. W.H. Jiang, G.J. Fan, F.X. Liu, G.Y. Wang, H. Choo, and P.K. Liaw: *Int. J. Plast.*, 2008, vol. 24, pp. 1–16.
117. A. Sarkar, P. Barat, and P. Mukherjee: *Fractals*, 2010, vol. 18, pp. 319–25.
118. A. Chatterjee, A. Sarkar, P. Barat, P. Mukherjee, and N. Gayathri: *Mater. Sci. Eng. A*, 2009, vol. 508, pp. 156–60.
119. M.A. Valdes-Tabernero, R. Sancho-Cadenas, I. Sabirov, M.Y. Murashkin, I.A. Ovid'ko, and F. Galvez: *Mater. Sci. Eng. A*, 2017, vol. 696, pp. 348–59.
120. N. Chibane, H. Ait-Amokhtar, and C. Fressengeas: *Scripta Mater.*, 2017, vol. 130, pp. 252–55.
121. D. Yuzbekova, A. Mogucheva, D. Zhemchuzhnikova, T. Lebedkina, M. Lebyodkin, and R. Kaibyshev: *Int. J. Plast.*, 2017, vol. 96, pp. 210–26.
122. M. Jobba, R.K. Mishra, and M. Niewczas: *Int. J. Plast.*, 2015, vol. 65, pp. 43–60.
123. A. Sarkar, S.A. Maloy, and K.L. Murty: *Mater. Sci. Eng. A*, 2015, vol. 631, pp. 120–25.
124. Y. Zhang, J.P. Liu, S.Y. Chen, X. Xie, P.K. Liaw, K.A. Dahmen, J.W. Qiao, and Y.L. Wang: *Prog. Mater. Sci.*, 2017, vol. 90, pp. 358–60.
125. D.M. Field and D.C. Van Aken: *Metall. Mater. Trans. A*, 2018, vol. 49A, pp. 1152–66.
126. P. Lan and J.Q. Zhang: *Metall. Mater. Trans. A*, 2018, vol. 49A, pp. 147–61.
127. P.D. Zavattieri, V. Savic, L.G. Hector, J.R. Fekete, W. Tong, and Y. Xuan: *Int. J. Plast.*, 2009, vol. 25, pp. 2298–30.
128. M. Madivala, A. Schwedt, S.L. Wong, F. Roters, U. Prahl, and W. Bleck: *Int. J. Plast.*, 2018, vol. 104, pp. 80–103.
129. J. Brechtl, B. Chen, X. Xie, Y. Ren, J.D. Venable, P.K. Liaw, and S.J. Zinkle: *Mater. Sci. Eng. A*, 2019, vol. 753, pp. 135–45.
130. S. Chen, X. Xie, B.L. Chen, J.W. Qiao, Y. Zhang, Y. Ren, K.A. Dahmen, and P.K. Liaw: *JOM*, 2015, vol. 67, pp. 2314–20.
131. R. Carroll, C. Lee, C.-W. Tsai, J.-W. Yeh, J. Antonaglia, B.A.W. Brinkman, M. LeBlanc, X. Xie, S. Chen, P.K. Liaw, and K.A. Dahmen: *Sci. Rep.*, 2015, vol. 5, art. no. 16997.
132. S.Y. Chen, X. Yang, K.A. Dahmen, P.K. Liaw, and Y. Zhang: *Entropy*, 2014, vol. 16, pp. 870–84.
133. S. Chen, L. Yu, J. Ren, X. Xie, X. Li, Y. Xu, G. Zhao, P. Li, F. Yang, Y. Ren, and P.K. Liaw: *Sci. Rep.*, 2016, vol. 6, art. no. 29798.
134. S. Chen, X. Xie, W. Li, R. Feng, B. Chen, J. Qiao, Y. Ren, Y. Zhang, K.A. Dahmen, and P.K. Liaw: *Mater. Chem. Phys.*, 2018, vol. 210, pp. 20–28.
135. M. Komarasamy, N. Kumar, R.S. Mishra, and P.K. Liaw: *Mater. Sci. Eng. A*, 2016, vol. 654, pp. 256–63.
136. S. Chen, W. Li, X. Xie, J. Brechtl, B. Chen, P. Li, G. Zhao, F. Yang, J. Qiao, K.A. Dahmen, and P.K. Liaw: *J. Alloy. Compd.*, 2018, vol. 752, pp. 464–75.
137. A. Yilmaz, *Sci. Technol. Adv. Mater.* 2011, vol. 12.
138. P. Rodriguez: *Bull. Mater. Sci.*, 1984, vol. 6, pp. 653–63.
139. L.H. Liu, Z.Y. Liu, Y. Huan, X.Y. Wu, Y. Lou, X.S. Huang, L.J. He, P.J. Li, and L.C. Zhang: *J. Alloy. Compd.*, 2018, vol. 766, pp. 908–17.
140. Z.Y. Liu, Y. Yang, and C.T. Liu: *Acta Mater.*, 2013, vol. 61, pp. 5928–36.
141. C. Suryanarayana and A. Inoue: *Bulk Metallic Glasses*, 2nd ed., CRC Press, New York, 2017, p. 520.
142. R. Maaß and J.F. Löffler: *Adv. Func. Mater.*, 2015, vol. 25, pp. 2353–68.
143. N.H. Alrasheedi, M.A. Yousfi, K. Hajlaoui, B.J. Mahfoudh, Z. Tourki, and A.R. Yavari: *Metals*, 2016, vol. 6, art. no. 48.
144. L.Z. Zhao, R.J. Xue, Z.G. Zhu, Z. Lu, E. Axinte, W.H. Wang, and H.Y. Bai: *J. Appl. Phys.*, 2014, vol. 116, art. no. 103516.
145. E.K.H. Salje and K.A. Dahmen: *Annu. Rev. Condens. Matter Phys.*, 2014, vol. 5, pp. 233–54.
146. Y. Shi, B. Yang, X. Xie, J. Brechtl, K.A. Dahmen, and P.K. Liaw: *Corrosion Sci.*, 2017, vol. 119, pp. 33–45.
147. N. Friedman, A.T. Jennings, G. Tsekenis, J.Y. Kim, M. Tao, J.T. Uhl, J.R. Greer, and K.A. Dahmen: *Phys. Rev. Lett.*, 2012, vol. 109, p. 095507.
148. K.A. Dahmen, Y. Ben-Zion, and J.T. Uhl: *Physical Review Letters*, 2009, vol. 102, p. 175501.
149. Y. Cao, X. Xie, J. Antonaglia, B. Winiarski, G. Wang, Y.C. Shin, P.J. Withers, K.A. Dahmen, and P.K. Liaw: *Sci Rep*, 2015, vol. 5, art. no. 10789.
150. J.T. Uhl, S. Pathak, D. Schorlemmer, X. Liu, R. Swindeman, B.A. Brinkman, M. LeBlanc, G. Tsekenis, N. Friedman, R. Behringer, D. Denisov, P. Schall, X. Gu, W.J. Wright, T. Hufnagel, A. Jennings, J.R. Greer, P.K. Liaw, T. Becker, G. Dresen, and K.A. Dahmen: *Sci. Rep.*, 2015, vol. 5, art. no. 16493.
151. Y. Hu, L. Shu, Q. Yang, W. Guo, P.K. Liaw, K.A. Dahmen, and J.M. Zuo: *Commun. Phys.*, 2018, vol. 1, art. no. 8.
152. K.A. Dahmen, J.T. Uhl, and W.J. Wright: *Front. Phys.*, 2019, vol. 7, p. 176.
153. M. LeBlanc, L. Angheluta, K. Dahmen, and N. Goldenfeld: *PhRvE*, 2013, vol. 87, art. no. 022126.
154. M.D. Costa, T. Henriques, M.N. Munshi, A.R. Segal, and A.L. Goldberger: *Chaos*, 2014, vol. 24, art. no. 5.
155. M. Costa, A.L. Goldberger, and C.K. Peng: *Phys. Rev. E*, 2005, vol. 71, art. no. 021906.
156. M. Costa, C.-K. Peng, A.L. Goldberger, and J.M. Hausdorff: *Physica A*, 2003, vol. 330, pp. 53–60.
157. M. Costa, A.L. Goldberger, and C.K. Peng: *Phys. Rev. Lett.*, 2002, vol. 89, art. no. 068102.

158. A. Hemakom, T. Chanwimalueang, A. Carrion, L. Aufegger, A.G. Constantinides, and D.P. Mandic: *IEEE J. Select. Topics Signal Process.*, 2016, vol. 10, pp. 1112–26.
159. J.A. Xia and P.J. Shang: *Fluct. Noise Lett.*, 2012, vol. 11, art. no. 12.
160. J. Brechtl, X. Xie, P.K. Liaw, and S.J. Zinkle: *Chaos Solitons Fract.*, 2018, vol. 116, pp. 166–75.
161. B. Zhang, P.K. Liaw, J. Brechtl, J. Ren, X. Guo, and Y. Zhang: *J. Alloy. Compd.*, 2020, vol. 820, art. no. 153092.
162. A. Sarkar, A. Chatterjee, P. Barat, and P. Mukherjee: *Mater. Sci. Eng. A*, 2007, vol. 459, pp. 361–65.
163. M.D. Costa and A.L. Goldberger: *Entropy*, 2015, vol. 17, pp. 1197–1203.
164. S.-D. Wu, C.-W. Wu, S.-G. Lin, K.-Y. Lee, and C.-K. Peng: *Phys. Lett. A*, 2014, vol. 378, pp. 1369–74.
165. R.E.A. van Emmerik, S.W. Ducharme, A.C. Amado, and J. Hamill: *J. Sport Health Sci.*, 2016, vol. 5, pp. 3–13.
166. E. Blons, L.M. Arsac, P. Gilfriche, and V. Deschodt-Arsac: *Entropy*, 2019, vol. 21, art. no. 1024.
167. A.C. Iliopoulos, N.S. Nikolaidis, and E.C. Aifantis: *J. Mech. Behav. Mater.*, 2015, vol. 24, pp. 1–9.
168. J.W. Qiao, Y. Zhang, and P.K. Liaw: *Intermetallics*, 2010, vol. 18, pp. 2057–64.
169. J.P. Sethna, K.A. Dahmen, and C.R. Myers: *Nature*, 2001, vol. 410, pp. 242–50.
170. B. Yuan, J.-J. Li, and J.-W. Qiao: *J. Iron Steel Res. Int.*, 2017, vol. 24, pp. 455–61.
171. T. Egami: *J. Alloy. Compd.*, 2011, vol. 509, pp. S82–S86.
172. T. Egami, K. Maeda, D. Srolovitz, and V. Vitek: *Journal De Physique Colloques*, 1980, vol. 41, pp. 272–75.
173. W. Li, H. Bei, Y. Tong, W. Dmowski, and Y.F. Gao: *Appl. Phys. Lett.*, 2013, vol. 103, p. 171910.
174. W.H. Wang: *Prog. Mater Sci.*, 2012, vol. 57, pp. 487–56.
175. B. Yang, C.T. Liu, T.G. Nieh, M.L. Morrison, P.K. Liaw, and R.A. Buchanan: *J. Mater. Res.*, 2006, vol. 21, pp. 915–22.
176. W.H. Peter, R.A. Buchanan, C.T. Liu, and P.K. Liaw: *J. Non-Cryst. Solids*, 2003, vol. 317, pp. 187–92.
177. M.L. Morrison, R.A. Buchanan, P.K. Liaw, B.A. Green, G.Y. Wang, C. Liu, and J.A. Horton: *Mater. Sci. Eng. A*, 2007, vol. 467, pp. 190–97.
178. T. Yuan, G.Y. Wang, Q.M. Feng, P.K. Liaw, Y. Yokoyama, and A. Inoue: *Acta Mater.*, 2013, vol. 61, pp. 273–79.
179. P.L. Sun, G.Y. Wang, and P.K. Liaw: *Scr. Mater.*, 2012, vol. 66, pp. 443–46.
180. G.Y. Wang, P.K. Liaw, Y. Yokoyama, and A. Inoue: *Intermetallics*, 2012, vol. 23, pp. 96–100.
181. N. Hua, X. Hong, Z. Liao, Q. Wang, L. Zhang, Q. Guo, X. Ye, J. Brechtl, and P.K. Liaw: *Intermetallics*, 2020, vol. 124, art. no. 106847.
182. N.B. Hua, X.S. Hong, Z.L. Liao, L. Zhang, X.Y. Ye, Q.T. Wang, and P.K. Liaw: *J. Non-Cryst. Solids*, 2020, vol. 542, art. no. 13.
183. A. Pardo, M.C. Merino, A.E. Coy, F. Viejo, R. Arrabal, and E. Matykina: *Corrosion Sci.*, 2008, vol. 50, pp. 1796–1806.
184. C. Lee, Y. Chou, G. Kim, M.C. Gao, K. An, J. Brechtl, C. Zhang, W. Chen, J.D. Poplawsky, G. Song, and Y. Ren: *Adv. Mater.*, 2020, vol. 32, art. no. 2004029.
185. M.C. Gao, J.-W. Yeh, P.K. Liaw, and Y. Zhang: *High-entropy Alloys: Fundamentals and Applications*, Springer, New York, 2016.
186. W. Li, S. Chen, and P.K. Liaw: *Scripta Materialia*, 2020, vol. 187, pp. 68–75.
187. P. Shi, W. Ren, T. Zheng, Z. Ren, X. Hou, J. Peng, H. Pengfei, and Y. Gao: *Nat. Commun.*, 2019, vol. 10, pp. 1–8.
188. I.S. Wani, T. Bhattacharjee, S. Sheikh, and Y.P. Lu: *Mater. Res. Lett.*, 2016, vol. 4, pp. 174–79.
189. K. Lu: *Science*, 2014, vol. 345, pp. 1455–56.
190. W. Xiaolei, M. Yang, F. Yuan, W. Guilin, Y. Wei, X. Huang, and Y. Zhu: *Proc. Natl. Acad. Sci. USA*, 2015, vol. 112, pp. 14501–505.
191. E. Ma and T. Zhu: *Mater. Today*, 2017, vol. 20, pp. 323–31.
192. W. Xiaolei and Y. Zhu: *Mater. Res. Lett.*, 2017, vol. 5, pp. 527–32.
193. J. Antonaglia, X. Xie, Z. Tang, C.-W. Tsai, J.W. Qiao, Y. Zhang, M.O. Laktionova, E.D. Tabachnikova, J.W. Yeh, O.N. Senkov, M.C. Gao, J.T. Uhl, P.K. Liaw, and K.A. Dahmen: *JOM*, 2014, vol. 66, pp. 2002–2008.
194. E. Kröner: *Zeitschrift für Physik*, 1958, vol. 151, pp. 504–18.
195. R. De Wit: *J. Appl. Crystallogr.*, 1997, vol. 30, pp. 510–11.
196. E.M. Francis, B.M.B. Grant, J. Quinta, P.J. da Fonseca, M.M. Phillips, M.R. Daymond, and M. Preuss: *Acta Mater.*, 2014, vol. 74, pp. 18–29.
197. X.-L. Wang, Y.D. Wang, A.D. Stoica, D.J. Horton, H. Tian, P.K. Liaw, H. Choo, J.W. Richardson, and E. Maxey: *Mater. Sci. Eng. A*, 2005, vol. 399, pp. 114–119.
198. G.K. Williamson and W.H. Hall: *Acta Metall.*, 1953, vol. 1, pp. 22–31.
199. T. Ungár, I. Dragomir, Á. Révész, and A. Borbély: *J. Appl. Crystallogr.*, 1999, vol. 32, pp. 992–1002.
200. D. Caillard: *Acta Mater.*, 2010, vol. 58, pp. 3493–3503.
201. B. Chen, S. Li, H. Zong, X. Ding, J. Sun, and E. Ma: *Proc. Natl. Acad. Sci. USA*, 2020, vol. 117, pp. 16199–16206.
202. F. Wang, G.H. Balbus, S. Xu, Y. Su, J. Shin, P.F. Rottmann, K.E. Knipling, J.C. Stinville, L.H. Mills, O.N. Senkov, and I.J. Beyerlein: *Science*, 2020, vol. 370, pp. 95–101.
203. N. Hua, W. Wang, Q. Wang, Y. Ye, S. Lin, L. Zhang, Q. Guo, J. Brechtl, and P.K. Liaw: *J. Alloys Compd.*, 2020, vol. 21, p. 157997.
204. Y.Z. Shi, L. Collins, R. Feng, C. Zhang, N. Balke, P.K. Liaw, and B. Yang: *Corrosion Sci.*, 2018, vol. 133, pp. 120–31.
205. Y.Z. Shi, J.K. Mo, F.Y. Zhang, B. Yang, P.K. Liaw, and Y. Zhao: *J. Alloy. Compd.*, 2020, vol. 844, art. no. 9.
206. Y.Z. Shi, B. Yang, P.D. Rack, S.F. Guo, P.K. Liaw, and Y. Zhao: *Mater. Des.*, 2020, vol. 195, art. no. 10.
207. Y.Z. Shi, B. Yang, and P.K. Liaw: *Metals*, 2017, vol. 7, art. no. 18.
208. Y.Z. Shi, L. Collins, N. Balke, P.K. Liaw, and B. Yang: *Appl. Surf. Sci.*, 2018, vol. 439, pp. 533–44.
209. W.-Y. Ching, S. San, J. Brechtl, R. Sakidja *et al.*: *npj Comput. Mater.*, 2020, vol. 6, art. no. 45.
210. G. Kresse and J. Furthmüller: *Phys. Rev. B*, 1996, vol. 54, art. no. 169.
211. O.H. Nielsen and R.M. Martin: *Phys. Rev. Lett.*, 1983, vol. 50, pp. 697–700.
212. R. Hill: *Proc. Phys. Soc. Sect. A*, 1952, vol. 65, pp. 349–54.
213. Z.A. Lethbridge, R.I. Walton, A.S. Marmier, C.W. Smith, and K.E. Evans: *Acta Materialia*, 2010, vol. 58, pp. 6444–51.
214. C. Huang and L. Chen: *Adv. Mater.*, 2016, vol. 28, pp. 8079–96.
215. X.F. Wang, T.E. Jones, W. Li, and Y.C. Zhou: *Phys. Rev. B*, 2012, vol. 85, art. no. 134108.
216. M. De Jong, W. Chen, R. Notestine, K. Persson, G. Ceder, A. Jain, M. Asta, and A. Gamst: *Sci. Rep.*, 2016, vol. 6, art. no. 34256.
217. A. Jain, S.P. Ong, G. Hautier, W. Chen, W.D. Richards, S. Dacek, S. Cholia, D. Gunter, D. Skinner, G. Ceder, and K.A. Persson: *Appl. Mater.*, 2013, vol. 1, art. no. 011002.
218. D. Peirce, R.J. Asaro, and A. Needleman: *Acta metallurgica*, 1983, vol. 31, pp. 1951–76.
219. A.F. Bower and E. Wininger: *J. Mech. Phys. Solids*, 2004, vol. 52, pp. 1289–17.
220. P. Chao and Y. Gao: *J. Appl. Mech.*, 2015, vol. 82, art. no. 031003.
221. L.L. Zheng, Y.F. Gao, S.Y. Lee, R.I. Barabash, J.H. Lee, and P.K. Liaw: *J. Mech. Phys. Solids*, 2011, vol. 59, pp. 2307–22.
222. J. Neuefeind, M. Feygenson, J. Carruth, R. Hoffmann, and K.K. Chipley: *Nucl. Instrum. Methods Phys. Res. Sect. B*, 2012, vol. 287, pp. 68–75.
223. T.H. Proffen, S.J.L. Billinge, T. Egami, and D. Louca: *Zeitschrift für Kristallographie Crystalline Materials*, 2003, vol. 218, pp. 132–43.
224. P. Juhás, D.M. Cherba, P.M. Duxbury, W.F. Punch, and S.J.L. Billinge: *Nature*, 2006, vol. 440, pp. 655–58.
225. G. Kresse and J. Hafner: *Phys. Rev. B*, 1993, vol. 47, art. no. 558.
226. L.J. Santodonato, P.K. Liaw, R.R. Unocic, H. Bei, and J.R. Morris: *Nature Commun.*, 2018, vol. 9, art. no. 4520.
227. C.-J. Tong, M.-R. Chen, J.-W. Yeh, S.-J. Lin, S.-K. Chen, T.-T. Shun, and S.-Y. Chang: *MMTA*, 2005, vol. 36, pp. 1263–71.
228. B.A. Welk, R.E.A. Williams, G.B. Viswanathan, M.A. Gibson, P.K. Liaw, and H.L. Fraser: *Ultramicroscopy*, 2013, vol. 134, pp. 193–99.
229. A. Manzoni, H. Daoud, R. Völkl, U. Glatzel, and N. Wanderka: *Ultramicroscopy*, 2013, vol. 132, pp. 212–15.

230. R.J. Arsenault, *United States* 1975.
231. J.-W. Yeh, S.-Y. Chang, Y.-D. Hong, S.-K. Chen, and S.-J. Lin: *Mater. Chem. Phys.*, 2007, vol. 103, pp. 41–46.
232. Z. Lyu, C. Lee, Shao.-Yu. Wang, X. Fan, J.-W. Yeh, and P.K. Liaw: *MMTA*, 2019, vol. 50, pp. 1–28.
233. S. Tammas-Williams and I. Todd: *Scripta Mater.*, 2017, vol. 135, pp. 105–10.
234. M. Seifi, A. Salem, J. Beuth, O. Harrysson, and J.J. Lewandowski: *JOM*, 2016, vol. 68, pp. 747–64.
235. M. Brandt: *Laser Additive Manufacturing: Materials, Design, Technologies, and Applications*, Woodhead Publishing, Sawston, 2016.
236. R. Zhou, Y. Liu, C. Zhou, S. Li, W. Wenqian, M. Song, B. Liu, X. Liang, and P.K. Liaw: *Intermetallics*, 2018, vol. 94, pp. 165–71.
237. Z.G. Zhu, Q.B. Nguyen, F.L. Ng, X.H. An, X.Z. Liao, P.K. Liaw, S.M.L. Nai, and J. Wei: *Scripta Mater.*, 2018, vol. 154, pp. 20–24.
238. S. Singh, N. Wanderka, B.S. Murty, U. Glatzel, and J. Banhart: *Acta Materialia*, 2011, vol. 59, pp. 182–90.
239. J.Y. He, W.H. Liu, H. Wang, Y. Wu, X.J. Liu, T.G. Nieh, and Z.P. Lu: *Acta Mater.*, 2014, vol. 62, pp. 105–13.
240. K. Kempen, L. Thijs, J. Van Humbeeck, and J.-P. Kruth: *Phys. Proc.*, 2012, vol. 39, pp. 439–46.
241. E. Ihlen: *Front. Physiol.*, 2012, vol. 3, p. 484.